Outgassing Rates of PEEK, Kapton® and Vespel® Polymers

Sergio Giacomo Sammartano

Degree Thesis

Materials Processing Technology

2020

Sergio Giacomo Sammartano

DEGREE THESIS	
Arcada	
Degree Programme:	Materials Processing Technology
Identification number:	18727
Author:	Sergio Giacomo Sammartano
Title:	Outgassing rates of PEEK, Kapton® and Vespel® polymers
Supervisor (Arcada):	Mariann Holmberg
Supervisor (CERN):	Ivo Wevers
Examiner (Arcada):	Stewart Makkonen-Craig
Commissioned by:	CERN

Abstract:

In this study commissioned by CERN, the outgassing behaviour of PEEK, Kapton® and Vespel® polymers has been investigated for potential use in the vacuum systems of particle accelerators. Polymeric materials are in general avoided in high vacuum (HV) and ultra-high vacuum (UHV) applications due to their high outgassing rates, which cannot be effectively reduced via bakeout procedures typically used with metals because of their usually low melting points and loss of mechanical performance above the glass transition temperature. The selected polymers have greater usability potential due to their superior thermal resistance and relatively low outgassing rates compared to most other polymers. Pump-down measurements were conducted on at least 5 samples of different thicknesses for each material, exposed to normal levels of moisture in the air (30-60% R.H.) prior to the tests. The data collected allowed to establish that diffusion of H_2O molecules from the bulk to the surface of these materials represents their main source of outgassing when under vacuum; the concurrent release of other atmospheric species such as N_2, O_2, CO and Ar above normal levels, detected through spectrometric analysis of the residual gases, suggested that PEEK and Vespel® can also trap relevant amounts of air simply upon exposure. The decay of the outgassing rates of all three polymers, initially proportional to the inverse of the square root of time, was characterized by a time constant τ that depended on the diffusion coefficient of water inside the material and the square of its thickness; the diffusive process exhibited Fickian characteristics during pumping times up to 3τ, but diverged considerably from the expected behaviour when extending the pumping beyond this limit, indicating the occurrence of a secondary diffusive mechanism becoming manifest at low concentrations of the diffusing species in the bulk. An empirical model consisting of a 3-step equation was obtained through regression analysis of the data and the values of diffusion coefficients D and initial moisture contents c_0 of each material were estimated by optimizing the parameters in the equations during the fitting procedure. The computed diffusion coefficients were $4.2 \cdot 10^{-9}$ cm^2 s^{-1} for PEEK, $1.7 \cdot 10^{-9}$ cm^2 s^{-1} for Kapton® and $1.8 \cdot 10^{-9}$ cm^2 s^{-1} for Vespel®, while the initial moisture content was estimated to be ca 0.3% in PEEK and ca. 1% in the other two materials. These values were found in good agreement with the information retrieved from the available sources.

Keywords:	Outgassing, vacuum, polymers, PEEK, polyimides, diffusion, CERN
Number of pages:	95
Language:	English
Date of acceptance:	29 May 2020

AKNOWLEDGMENTS

First and foremost, I would like to deeply thank my CERN supervisor, Ivo Wevers, for providing me with his invaluable advice throughout my whole experience as a technical student at the laboratory. This research project would have not been possible without his guidance, his thoughtful insights and troubleshooting skills, and I am sincerely grateful to have been given the chance to learn so much while working under his supervision.

My sincere thanks also go to all the members of the VSC group, whom it has been an honour and pleasure to work with, and in particular to Giuseppe Bregliozzi, leader of the BVO section, for his constructive suggestions and constant support during the execution of the experiments.

I wish to express my most sincere appreciation to my university supervisor, Mariann Holmberg, who has inspired and encouraged me not only during the writing of this document, but also throughout the time I spent at Arcada as a student: her enthusiasm for the discipline of materials science has truly been an invaluable source of motivation during my entire academic career, and it will continue to be so in the future.

Last, but not least, I would like to thank the whole staff of the department of Energy and Materials Technology at Arcada, for giving me the opportunity to study and learn in such a friendly and stimulating environment. In particular, I thank Mirja Andersson, head of the department, for teaching me research methodology and project management skills, and Rene Herrmann, for reigniting over and over my passion for mathematical and physical disciplines throughout his courses.

CONTENTS

LIST OF FIGURES

LIST OF TABLES

LIST OF SYMBOLS (IN ORDER OF APPEARANCE)

n	Particle number density
N	Number of particles
V	Volume
p	Pressure
k	Boltzmann constant
T	Absolute temperature (in kelvins)
ν	Number of moles
R	Universal gas constant
N_a	Avogadro's number
$\bar{v}$	Average speed of gas particles
π	Mathematical constant Pi
m	Mass
M	Molar mass
j	Particles impingement/adsorption/desorption/diffusion rate per unit area
$\bar{\lambda}$	Particles mean free path
d	Particles diameter / characteristic dimension of a vacuum vessel
Kn	Knudsen number
$\dot{V}$	Volumetric flow rate
t	Time
S	Pumping speed
Q	Gas throughput/outgassing rate
C	Conductance
A	Surface area
L	Length of a duct
D	Second characteristic dimension of a duct / Diffusion coefficient
dn	Molecular flux from a differential surface element in a certain direction
β	Angle of a direction with the normal to a surface
$d\omega$	Differential solid angle with axis at an angle β with the normal to a surface
α	Transmission probability
s	Sticking probability
θ	Surface coverage fraction

$\tilde{n}$	Number of particles per unit area adsorbed on the surface
$\tilde{n}_{mono}$	Number of adsorbed particles in a unit area of a surface forming a monolayer
E_{ads}	Adsorption energy
E_{des}	Desorption energy
ν_0	Oscillation frequency of particles
e	Mathematical constant e (Euler's number)
τ_0	Oscillation period of particles
h	Planck's constant
f	Fraction of a monolayer desorbed from a surface
p_0	Pressure at the unit time of pumping
q	Specific outgassing rate
q_0	Specific outgassing rate at the unit time of pumping
c	Concentration of a species dissolved in the bulk of an object
x, y, z	Spatial coordinates of a point in a three-dimensional object
c_0	Initial concentration of a species dissolved in the bulk of an object
l	Thickness of a slab
τ	Diffusion time constant
τ_s	Sojourn time
i	Electrical current
K	Proportionality constant for pressure measurement with HV gauges
T_g	Glass transition temperature
T_m	Melting temperature
j_0	Parameter in the diffusion 3-step model

LIST OF ABBREVIATIONS (IN ALPHABETIC ORDER)

ABS	Acrylonitrile Butadiene Styrene
ALICE	A Large Ion Collider Experiment
ATLAS	A Toroidal LHC ApparatuS
BG	BackGround
BVO	Beam Vacuum Operation section
CMS	Compact Muon Solenoid
CERN	European Organization for Nuclear Research
DMS	Dual-Mode Sorption
DNA	DeoxyriboNucleic Acid
ELENA	Extra Low ENergy Antiproton ring
HV	High Vacuum
IUPAC	International Union of Pure and Applied Chemistry
LEIR	Low Energy Ion Ring
LHC	Large Hadron Collider
LHCb	Large Hadron Collider beauty
LIGO	Laser Interferometer Gravitational-wave Observatory
LINAC	LINear ACcelerator
RGA	Residual Gas Analyser
RNA	RiboNucleic Acid
PEEK	Polyether Ether Ketone
PhD	Philosophiae Doctor (Latin), Doctor of Philosophy
PS	Proton Synchrotron
PSB	Proton Synchrotron Booster
RGA	Residual Gas Analyser
SI	International System of Units
SPS	Super Proton Synchrotron
TMP	Turbo-Molecular Pump
TDS	Technical Data Sheet
UHV	Ultra-High Vacuum
VSC	Vacuum, Surfaces and Coatings group

1 INTRODUCTION

At the European Organization for the Nuclear Research (CERN), physicists use particle accelerators such as the Proton Synchrotron (PS), the Super Proton Synchrotron (SPS) and the Large Hadron Collider (LHC) to study the fundamental properties of matter (CERN, 2020a), by colliding beams of particles moving at relativistic speeds into special fixed targets or against other beams moving in opposite direction. These machines need to operate at extremely low pressures (CERN, 2020b) in order to reduce as much as possible the probability of interaction between the accelerated beams and other extraneous particles present inside the pipeline where the beams move. The achievement of those pressures is made difficult by the continuous flow of molecules releasing from every surface exposed to vacuum, a phenomenon known as outgassing (Hudson, 1998, p. 614). Since this process heavily depends on the nature and characteristics of the surfaces themselves, the selection of the most appropriate materials to use in such systems is of extreme importance for their operational functionality (Lee, 1989).

Polymers are usually avoided in high vacuum (HV) and ultra-high vacuum (UHV) applications due to their high outgassing rates (LIGO, 2011), but few technical and engineering plastics such as PEEK (polyether ether ketone) and the polyimides Vespel® and Kapton® have nevertheless found applications in vacuum equipment due to technical, manufacturing or economic reasons. The characterization of the outgassing behaviour of these polymers under vacuum is therefore of great interest to the engineers responsible for the achievement of the operational vacuum pressures inside particle accelerators.

The present thesis work offers an insight on the topic by presenting the results collected during 14 months of internship that the author carried out at CERN between February 2019 and March 2020. The first sections of the document describe the theoretical concepts, the materials, the equipment and the methodology utilized in a series of tests performed to characterize the outgassing of PEEK, Kapton® and Vespel® polymers; the analysis of the collected data, the discussion of their physical meaning and their dependence on the characteristics and properties of the polymers constitute the central part of the thesis, which is concluded with final considerations on the outgassing behaviour of these polymeric materials during pump-down, and practical recommendations on the selection, storage and handling of polymeric components before installation.

1.1 Background

1.1.1 The European Organization for Nuclear Research (CERN)

The European Organization for Nuclear Research, known internationally as CERN[1], is a scientific institution established in 1954 with the aim to promote the development of nuclear physics in Europe (CERN, 2020c). For more than six decades, the organization has provided infrastructure and other resources necessary to conduct research in fundamental physics, particularly in the field of particle physics. Because of this, the CERN laboratory is site of a huge complex of particle accelerators and detectors (CERN, 2020d), of which a schematic representation is given in Figure 1.

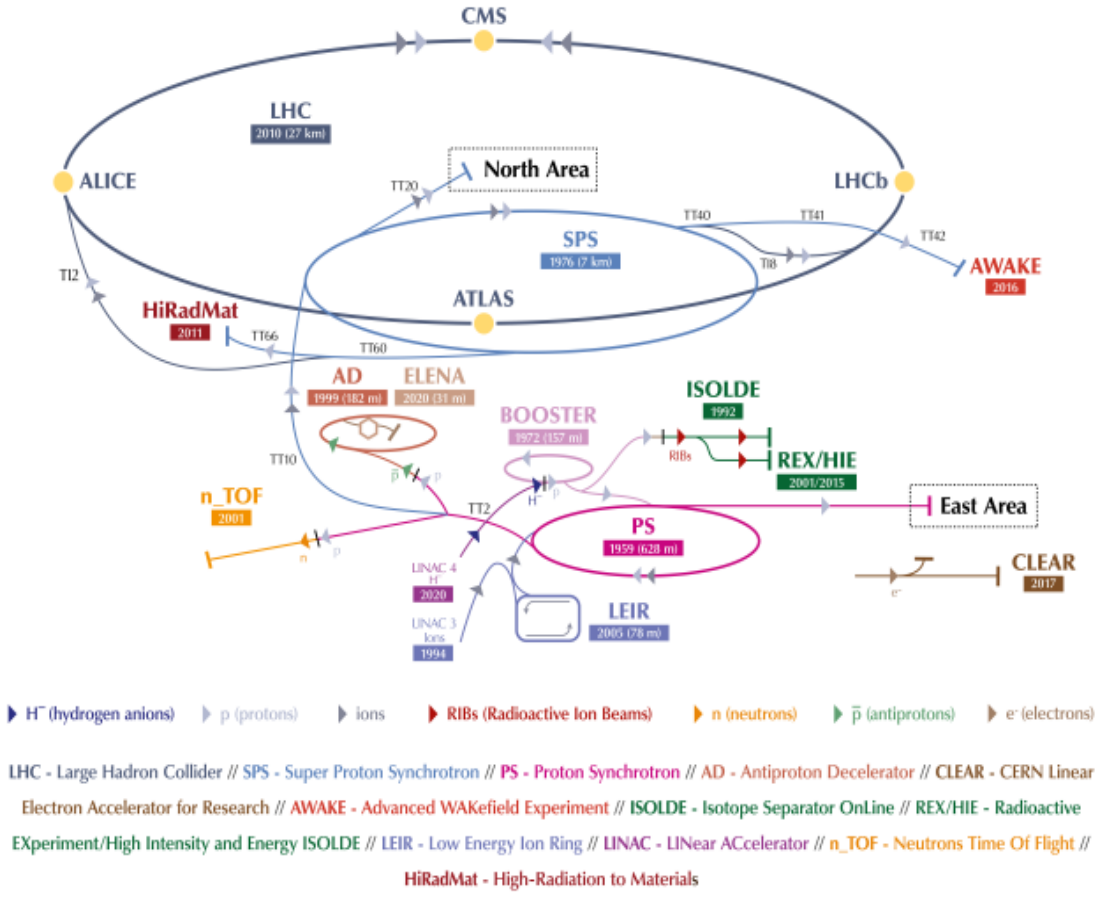

Figure 1. The accelerators complex at CERN (CERN, 2020e).

[1] The acronym, standing for European Council for Nuclear Research (in French: "Conseil Européen pour la Recherche Nucléaire"), was used for the first time during a UNESCO meeting held in 1951 in Paris, when the foundation of an international institute for the development of atomic physics in Europe was officially proposed. The council was established in 1952 with the signature of 11 countries, officially adopting the acronym CERN for the new-born institution. The term “Council” was eventually changed into “Organization” due to the expansion of the scope of the institute, but the original acronym was maintained as the de-facto name by which the research center is internationally known (CERN, 2020c).

The complex is a connected succession of machines (the so called "accelerators chain") that allow to accelerate to increasingly higher energies beams of electrically charged particles such as protons or lead ions. Linear accelerators (LINACs) feed the first, relatively small circular machines LEIR (Low Energy Ion Ring) and PSB (Proton Synchrotron Booster, often simply referred to as Booster), from which the beams can be transferred to a series of interconnected accelerators of gradually greater size: the PS, the SPS and the LHC. Experimental halls equipped with special collision targets and detectors are present in almost every accelerator of the chain, allowing to conduct experiments at several different energies: the Booster accelerates the beams to 1.4 GeV[2], the PS to 25 GeV and the SPS up to 450 GeV. Instead of using collision targets, the LHC makes two beams circulating in opposite direction collide against each other at 4 designed points, where the LHC experiments ALICE, ATLAS, CMS and LHCb are located[3]: each beam of particles is accelerated up to an energy of 6.5 TeV, for a total energy at the collision points of 13 TeV. With its circumference of 27 km, the Large Hadron Collider is (as of the year 2020) both the most powerful and the largest particle accelerator in the world (CERN, 2020a).

Through the years, CERN accelerators have been used to test the predictions of the Standard Model of particle physics, a theory developed in the 1970s that describes the structure of everything that exists in the universe as made of a surprisingly small number of basic fundamental particles (quarks, leptons and bosons), governed by four forces (the strong force, the weak force, the electromagnetic force, and the gravitational force). The discoveries of the W and Z boson in the 1980s and that of the Higgs boson in 2012 are perhaps the best-known examples of how CERN contributed to the validation of the theory (CERN, 2020f; CERN, 2020g).

Currently, the laboratory is aiming not only to study in greater detail the particles described by the Standard Model, but also to investigate the boundaries and limitations of the theory, in the attempt to find evidence of new physics beyond it. Several are the rea-

[2] The eV (electron Volt) and its multiples GeV (10^9 eV = 1.6 x 10^{-10} J) and TeV (10^{12} eV = 1.6 x 10^{-7} J) are units used in particle physics to describe the energies of moving particles and collisions, since the Joule is very impractical for such cases. An eV is defined as the work done by an electric field to move a particle with unitary charge (for example an electron or a proton) through a potential difference of 1 Volt (Halliday, Resnick, & Walker, 2008, p. 771).

[3] More information about the LHC experiments and their detectors is available on the following internet page: https://home.cern/science/experiments.

sons to do so. For example, the Standard Model does not explain what dark matter and dark energy are, nor predicts their existence, although there is strong empirical evidence for both. Another example is the notorious difficulty to incorporate General Relativity, Einstein's famous theory of gravity, into the same mathematical framework of quantum mechanics – the theory at the core of the Standard Model – incompatibility which calls for a revision of one theory or the other, or both (CERN, 2020g).

Although the main focus of CERN is particle physics, its research program is much broader, encompassing experiments in nuclear physics, high-energy physics and condensed matter physics, as well as investigations on the behaviour of antimatter and radioactive phenomena. To bring advances in all these fields, the laboratory needs sophisticated equipment and tools delivering ultimate performance, the development of which has often pushed forward the limits of technology and brought innovations into important scientific areas such as materials science and computing. Many of these innovations have found applications in other scientific fields, industry and everyday life, like the introduction of vacuum technologies used in electron microscopy and computer chip manufacture, the development of powerful imaging techniques for medical diagnosis and – perhaps the most famous contribution to modern society – the invention of the World Wide Web (CERN, 2020f).

1.1.2 The Vacuum at CERN

As mentioned before, to avoid colliding with gas molecules inside an accelerator, the beams of particles must move in a vacuum, thus each sector of the accelerators chain at CERN is also a vacuum system with its own pressure requirements, ranging from the low 10^{-6} mbar of the LINACs to the low 10^{-12} mbar of the ELENA ring (Bregliozzi, 2017, p. 2-16). As a whole, the CERN accelerators complex is one of the biggest vacuum systems in the world, comprising 128 km of vacuum pipelines overall, 104 km of which are inside the LHC alone (Bregliozzi, 2017, p. 17), as a consequence of its three separate vacuum systems: one for the beam pipes, one for insulating the cryogenically cooled magnets and one for insulating the helium distribution line[4] (CERN, 2020b).

[4] Superconductive dipole magnets are used to steer the beams of particles inside the curved sectors of the LHC. These magnets are kept at 1.9 K (-271.3°C) by liquid helium and the vacuum serves as a thermal insulator both for the helium distribution line and the magnets themself, reducing the amount of heat that seeps from the surrounding room-temperature environment (CERN, 2020b).

Attaining and keeping high vacuum or ultra-high vacuum inside such a vast system of vessels and pipelines is a truly challenging task, requiring the prowess and commitment of a team of mechanical engineers and specialized technicians, surface-physics specialists, thin-film coating experts and electroplating professionals, all dedicated to the design, construction, operation, maintenance and upgrade of high and ultra-high vacuum systems for the accelerators and detectors of the complex (Chiggiato, 2018). This team of people constitutes the Vacuum, Surfaces and Coatings (VSC) group of the CERN Technology Department, a unit whose mandate is to provide all the required technologies and innovations necessary to run the accelerators under the best possible conditions and make all the programmed experiments possible.

The VSC group is responsible for a wide range of services and operations, including the management of the logistic chain of the vacuum equipment, installation of vacuum components, support on vacuum control systems and monitoring tools, characterization of materials and surfaces in UHV, degassing analysis and treatments, simulation of dynamic pressure profiles, plasma characterization, coatings, electroplating, surface cleaning services and more (CERN, 2019). Research and development are also very important activities inside the group: a significant number of PhD and Technical Students from universities all around the world are regularly integrated into its personnel with the purpose of conducting studies on new materials, surface treatments, desorption phenomena and measurement techniques, while project associates from several industrial sectors constantly collaborate with the VSC group to develop more efficient and better performing equipment designed to generate, improve, maintain and monitor the vacuum inside the already existing and future accelerators.

The Beam Vacuum Operation (BVO) section of the VSC group is the most specialized in the testing, installation, maintenance and in-situ treatment of components for the vacuum systems of the accelerators chain. Its members make sure that the vacuum requirements of each sector are achieved within specific time constraints and in accordance with the experimental schedule of the laboratory. The task is particularly demanding in the LHC, due to the exceptional length of its vacuum system and the very low pressure requirements, in the range 10^{-8} – 10^{-10} mbar (Bregliozzi, 2017, p. 14-15). The BVO section fulfils this task by applying the most effective available strategies, materials and technologies to attain the most efficient pumping and reduce at the same time the outgassing from the internal surfaces of the vacuum vessels to the lowest possible levels.

1.2 Scope of the Thesis

During his internship as a Technical Student in the BVO section of the VSC group, the author was given the task to investigate the outgassing behaviour of three selected polymeric materials, PEEK, Kapton® and Vespel®, and assess the impact of their application in the HV and UHV systems of the accelerators complex at CERN. The outcomes of the investigation developed into the present thesis work, whose fundamental aim is the quantification of the specific outgassing rates of these materials during pump-down as a function of time and certain properties of the materials themselves, in particular thickness, moisture content and diffusion coefficient.

This will be done by attempting to fit the empirical data with curves computed using the Fickian diffusion model, whose suitability to replicate and predict the outgassing behaviour of the selected polymeric materials will be also evaluated. Based on the results of this assessment, a possible modification to the model will be presented, in the attempt to provide a more accurate method to predict the outgassing rates of these three polymers even for very long pump-down times.

2 LITERATURE REVIEW

2.1 Fundamentals of Vacuum Science

The term vacuum is generally used to denote a region of space in which the pressure is significantly low compared to atmospheric pressure. This definition is quite broad, encompassing a wide range of values that in applications on earth can span approximately 15 orders of magnitude, from the low vacuum generated inside a vacuum cleaner, to the ultra-high vacuum achieved in some particle accelerators, which is about the same as the one found in the interplanetary space (Chambers, 2005, p. 1-2). The terms “low” and “ultra-high” denote two of the five categories into which this extended pressure range is traditionally divided, i.e. low, medium, high, ultra-high and extreme ultra-high vacuum, whose upper and lower boundaries are summarized in Table 1. Although this division is somewhat arbitrary, it is nevertheless convenient because it allows to quickly denote the different physical phenomena that occur within the pressure ranges specified for each category (Singh & Thomas, 1998, p. 4), most notably the behaviour and properties of gases (Chambers, 2005, p. 7).

Table 1. The five degrees of vacuum ordered by pressure range (Chambers, 2005, p. 7).

Region	Pressure range
Low (rough) vacuum	Atmospheric pressure to 1 hPa
Medium vacuum	1 to 10^{-3} hPa
High vacuum (HV)	10^{-3} to 10^{-8} hPa
Ultrahigh vacuum (UHV)	10^{-8} to 10^{-12} hPa
Extreme high vacuum (XHV)	Less than 10^{-12} hPa

2.1.1 Units

Being described in terms of pressure, its units are used to measure vacuum. The standard unit of pressure in the International System of Units (SI) is the pascal (symbol Pa), defined as 1 Pa = 1 N m^{-2} = 1 kg m^{-1} s^{-2} (Bureau International des Poids et Mesures, 2019, p. 137). Due to historical reasons, however, several other units of pressure exist, most notably the standard atmosphere (1 atm = 101325 Pa), used in oceanography and chemistry, the torr (1 Torr ≈ 133 Pa), also known as millimeter of mercury and very common in meteorology, and the bar (1 bar = 10^5 Pa), which is widely employed in several technical and engineering fields. The torr and the 10^{-3} submultiple of the bar, i.e. the millibar (mbar), are still today very relevant to vacuum technology, and often adopted even in the published material on the subject (Chambers, 2005, p. 5-6). In particular, the millibar is the unit utilized at CERN to measure the pressure in the accelerators and in the laboratory test-benches used for vacuum-related experiments carried out by the VSC group. Since 1 mbar = 10^2 Pa = 1 hPa, values expressed in millibars can be readily translated into equivalent SI values without the need to apply any conversion factor, thus the hectopascal will be used throughout this document to report the results collected during the measurements conducted at CERN for the purposes of this study.

2.1.2 Number Density, Ideal Gas Law and the Kinetic Theory of Gases

Even at the lowest achievable pressures, a vacuum is far from being completely empty: that is, a perfect vacuum is more an abstract idealization than a physical reality. At an altitudes of ca. 800 km above the ground, where artificial satellites normally orbit the earth essentially frictionless, there are roughly 10^{15} particles (molecules and single atoms) per m^3, while in the space between the planets there are still about 10^7 particles per m^3. For reference, at the sea level on earth, 1 m^3 of air contains on average $2.5 \cdot 10^{25}$ particles (Chambers, 2005, p. 2). Thus, creating a vacuum in a certain region of space

essentially means reducing the number of particles per unitary volume in that space, a quantity called *particle number* density or simply *number density*, denoted in this document with the symbol *n* and defined as:

$$n = \frac{N}{V} \qquad 2.1$$

where N is the number of particles present in a certain region of space of volume V.

Even at extremely low pressures found in typical HV and UHV systems, the ensemble of particles in the evacuated space still behaves overall as a gas and can be described quite well by the general gas equation of state (Singh & Thomas, 1998, p. 8-10), also known as ideal[5] gas law (Jitschin, 2016b, p. 36):

$$pV = NkT \qquad 2.2$$

In the above, p represents the gas pressure, V the volume occupied by the gas, N the number of particles present in the volume V, T the absolute temperature expressed in kelvins and $k = 1.381 \cdot 10^{-23}\ \mathrm{J\,K^{-1}}$ is the Boltzmann constant. Dividing both sides by the volume V and taking into account Equation 1.1, the ideal gas law becomes:

$$p = nkT \qquad 2.3$$

Thus, for any given temperature, the pressure of a gaseous system can be directly related to its number density.

There are other formulations of the ideal gas law, among which the most useful is perhaps the one that links the pressure, volume and temperature of a gas with its amount, expressed in number of moles *v* (Jitschin, 2016b, p. 36):

$$pV = \nu RT \qquad 2.4$$

Here $\nu = N/N_a$, being N_a = 6.022 · 10^{23} $\mathrm{mol^{-1}}$ the Avogadro's number, which is the number of particles (atoms for monoatomic gases, molecules for polyatomic gases and other compounds) contained in a mole of a certain substance, hence ν represents the number of moles in the volume V. The symbol $R = 83.14\ \mathrm{hPa\,L\,mol^{-1}K^{-1}}$ is the universal gas constant, which makes the equation very handy to express concentration val-

[5] Depending on their state, real gases behave more or less differently than what predicted by the ideal gas law. Usually, the deviation is higher under higher pressure and at lower temperature, i.e. for higher number density values. On the other hands, the more rarefied a gas is, the better its behaviour approximates that of an ideal gas (Jitschin, 2016b, p. 37).

ues in pressure units and calculate concentration changes in in terms of mass flow rates.

Equation 2.4 represents the original version of the ideal gas law as formulated by Clapeyron in the early 19th century and derived combining the results of experiments conducted in the 17th and 18th century by Boyle, Mariotte, Charles, Avogadro and Gay-Lussac on the macroscopic properties of gases (Clapeyron, 1834). On the other hand, Equations 2.2 and 2.3 arose from a completely different theoretical framework based on statistical methods and a series of assumptions and idealizations on the behaviour of the microscopic particles constituting a substance in its gaseous state. Originally conceived in the mid-19th century by Krönig (Jitschin, 2016b, p. 39), and later further developed by Clausius, Maxwell, and Boltzmann at the end of the 19th century, this theoretical framework, known as the *kinetic theory of ideal gases*, is of central importance in vacuum science and technology (Chambers, 2005, p. 26).

The theory is based on few idealizations and assumptions (Singh & Thomas, 1998, p. 11) that can be summarized as follows:

- A gas is composed of a very large number of tiny particles that are in constant, chaotic motion.
- The volume occupied by these particles is negligible compared to the total volume occupied by the gas, and the average distance between two particles is large compared to their size.
- The particles continuously hit each other and the walls of the gas container, following the laws of classical mechanics.
- During these collisions, the total kinetic energy is conserved, that is, the particles behave as perfect elastic spheres and they are assumed to exert no force on each other at a distance.

Building upon these basic assumptions, the theory derives the macroscopic properties of ideal gases from the microscopic motion of their individual particles: the temperature of a gas is a measure of the kinetic energy of its particles (Singh & Thomas, 1998, p. 11-12), while the pressure exerted by the gas on the walls of a container is due to the change in momentum the particles undergo during their collisions with the walls, and it is proportional to the rate of these collisions (Chambers, 2005, p. 33).

One of the central results of the kinetic theory of gases is the formulation of the Maxwell-Boltzmann probability distribution function of the speeds of the particles of a gas,

which allows to compute the particles average speed knowing the mass m of a single particle and the temperature of the gas (Chambers, 2005, p. 28-29):

$$\bar{v} = \sqrt{\frac{8kT}{\pi m}} \qquad 2.5$$

Since $N_a m = M$ and $N_a k = R$, the above equation can also be written in terms of a gas molar mass M by multiplying both numerator and denominator by Avogadro's number:

$$\bar{v} = \sqrt{\frac{8RT}{\pi M}} \qquad 2.6$$

which allows to calculate the particles average speed in a slightly easier way than using Equation 2.5, since it does not deal with the extremely small masses of the gas particles, which are in the order of 10^{-27}-10^{-26} kg (Chambers, 2005, p. 29).

The rate of collisions between the particles of a gas and a unit area of a surface exposed to it, also called impingement rate, depends on both the gas number density and its particles average speed, according to the following relationship (Chambers, 2005, p. 32):

$$j = \frac{n\bar{v}}{4} \qquad 2.7$$

By combining the latter with the previous equations, it is possible to express the impingement rate of a gas as function of its pressure and molecular mass (Chambers, 2005, p. 38-39):

$$j = \frac{p}{\sqrt{2\pi m k T}} \qquad 2.8$$

Or, since $m = \frac{M}{N_a}$ and $k = \frac{R}{N_a}$:

$$j = \frac{p N_a}{\sqrt{2\pi M R T}} \qquad 2.9$$

Hence, for a specific temperature, the impingement rate is proportional to the pressure of the gas and inversely proportional to the square root of its molecular/molar mass.

The theory also introduces the important concept of *mean free path* $\bar{\lambda}$, which is the average distance travelled by a gas particle before colliding with another particle:

$$\bar{\lambda} = \frac{1}{\sqrt{2} n \pi d^2} \qquad 2.10$$

where d is the diameter of the particle and n is the number density (Singh & Thomas, 1998, p. 17). By expressing n as the ratio p/kT, the mean free path can be rewritten as:

$$\bar{\lambda} = \frac{kT}{\sqrt{2} p \pi d^2} \qquad 2.11$$

This equation shows that the mean free path of gas particles is inversely proportional to the gas pressure, hence the more rarefied a gas, the longer the mean free path of its constituting particles.

Understanding the actual meaning of the quantities $p, n, \bar{v}, j$ and $\bar{\lambda}$ and their mutual connection is of fundamental importance in vacuum technology, since it allows to correctly analyse a series of phenomena that are directly depending on them. A practical example of how these quantities change with the different degrees of vacuum is given in the Table 2 below.

Table 2. Values of $n, j, \bar{v}$ and $\bar{\lambda}$ for N_2 at 273 K and various pressure levels (Chambers, 2005, p. 38).

p (hPa)	n (m^{-3})	j ($cm^{-2}\ s^{-1}$)	$\bar{\lambda}$	$\bar{v}$ ($m\ s^{-1}$)
$10^3 \approx 1$ atm	$2.5 \cdot 10^{25}$	$2.9 \cdot 10^{23}$	64 nm	454
1 (rough vacuum)	$2.5 \cdot 10^{22}$	$2.9 \cdot 10^{20}$	64 µm	
10^{-3} (medium vacuum)	$2.5 \cdot 10^{19}$	$2.9 \cdot 10^{17}$	64 mm	
10^{-6} (HV)	$2.5 \cdot 10^{16}$	$2.9 \cdot 10^{14}$	64 m	
10^{-10} (UHV)	$2.5 \cdot 10^{12}$	$2.9 \cdot 10^{10}$	640 km	

2.1.3 Knudsen Number and Gas Flow Regimes

The flow of a gas in a duct is affected by both the pressure of the gas and the geometry of the duct. Under standard conditions[6], the gas particles have an extremely short mean free path (see Table 2) and collide with each other much more often than with the walls of the vessel they are moving through. Conversely, at pressures in the HV and UHV regions, the mean free path becomes considerably larger than the characteristic dimensions of typical vacuum vessels (such as their diameter), and thus collisions between the

[6] The International Union of Pure & Applied Chemistry (IUPAC) since 1982 has defined the standard temperature and pressure (STP) as 273.15 K (0 °C) and 10^5 Pa (1 bar). Other organizations, however, define the standard conditions slightly differently: the National Institute of Standards & Technology (NIST) uses 293.15 K (20 °C) and 101.325 kPa (1 atm), for example (Mosher, 2016). In this document, the expression "standard conditions" denotes the STP as defined by the IUPAC.

particles and the walls become much more frequent than the collisions between the particles themselves (Chambers, 2005, p. 41-42). These two opposite situations determine distinct *flow regimes*, whose type can be determined by evaluating a ratio called *Knudsen number*, defined as (Livesey, 1998, p. 81-82):

$$Kn = \frac{\bar{\lambda}}{d} \qquad 2.12$$

where $\bar{\lambda}$ is the mean free path and d is the characteristic dimension of the vacuum duct.

Depending on the Knudsen number[7], three different types of flow regimes can be identified (Jitschin, 2016a, p. 83-84):

- $Kn < 0.01$: *continuum flow*. The mean free path is much smaller than the characteristic dimension of the duct and the gas particles affect each other motion through a great number of mutual collisions, which are much more frequent than particle-wall collisions; the gas behaves like a continuum and its flow can be analysed hydrodynamically.
- $Kn > 0.5$: *molecular flow*. The mean free path is of the same order or larger than the characteristic dimension of the duct and therefore the particles very seldom interact with each other; their motion is almost entirely determined by particle-wall collisions, resulting in random zig-zag paths from wall to wall that, combined together, form the macroscopic flow. The normal laws of hydrodynamics cannot be applied to this type of flow.
- $0.01 < Kn < 0.5$*: transitional flow*. The mean free path is slightly smaller than the dimensions of the container and both particle-wall and particle-particle collisions occur with similar frequency; the characteristics of the flow are somewhat in between those of continuum and molecular flow.

The inner volumes of most HV and UHV pipelines are usually a few centimetres across, which is comparable to the $\bar{\lambda}$ of the most abundant atmospheric gases, such as nitrogen, in the lower limit of the medium vacuum region (see Table 2). This implies that, once reached pressures below 10^{-3} hPa (usually achieved in less than one minute with modern

[7] Different authors often report slightly different values of Kn, for example setting to 1 the lower limit for molecular flow (see Chambers, 2005, p. 42 or Singh & Thomas, 1998, p. 27). This might also be due to different choices for the characteristic dimension, for example the radius of a pipe instead of its diameter.

pumping equipment for HV and UHV systems), $Kn > 0.5$ and so the residual gaseous particles flow in the molecular regime.

2.1.4 Flow Measurement: Gas Throughput, Pumping Speed, Conductance

In the field of vacuum science and technology, it is common practice to express the flow of gases as the product of pressure p and the volumetric flow rate $\dot{V} = dV/dt$, since the product pV is an indirect way to express the amount of gas in terms of number of molecules or moles (see Equations 2.2 and 2.4). The product $p\dot{V}$ is called gas *throughput* and is typically measured in units such as mbar L s^{-1} (Chambers, 2005, p. 79), which is the de-facto standard unit used at the VSC group for this physical quantity.

Although not an SI unit, the litre is accepted for use together with SI units by the International Committee for Weights and Measures (Bureau International des Poids et Mesures, 2019, p. 145), since it corresponds to an SI sub-multiple of the cubic meter, that is 1 L = 10^{-3} m^3 = 1 dm^3, hence values given in mbar L s^{-1} can readily be expressed either as hPa L s^{-1} or as hPa dm^3 s^{-1} without using any conversion factor.

The volumetric flow rate $\dot{V}$ is often given the symbol S and called *pumping speed*, especially when it refers to the flow rate at the inlet of a pump or at the entrance of a pipe that has a pump connected to its other end (Chambers, 2005, p. 80). Using the pumping speed, the gas throughput Q can be written as:

$$Q = p\dot{V} = Sp \qquad 2.13$$

When the inlet of a pump is directly connected to a vacuum chamber, the *effective* pumping speed of the system is determined by the nominal volumetric pumping speed of the pump. However, if some restrictive elements are interposed between the vacuum chamber and the inlet of the pump, which is often the case, the effective pumping speed at the outlet of the vacuum chamber is reduced by an amount that depends on how much the intermediate elements restrict the flow, situation represented in Figure 2.

In vacuum science, a quantitative analysis of this effect is done by introducing the concept of *conductance* C of an element, which is a measure of the ease of flow of a gas through that element. The latter could be, for example, an opening in a wall connecting two adjacent chambers, a straight pipe, or simply a part of the chamber with a different geometry.

In Figure 2, assuming isothermal[8] steady flow from the chamber on the left to the pump on the right, the gas throughput is proportional to the pressure differential between the two volumes and the conductance of the pipe, that is:

$$Q = C(p - p^*) \qquad 2.14$$

The conductance has therefore the same dimensions as the pumping speed, i.e. volume/time, and it is expressed in units such as L s^{-1} or dm^3 s^{-1} (Chambers, 2005, p. 80).

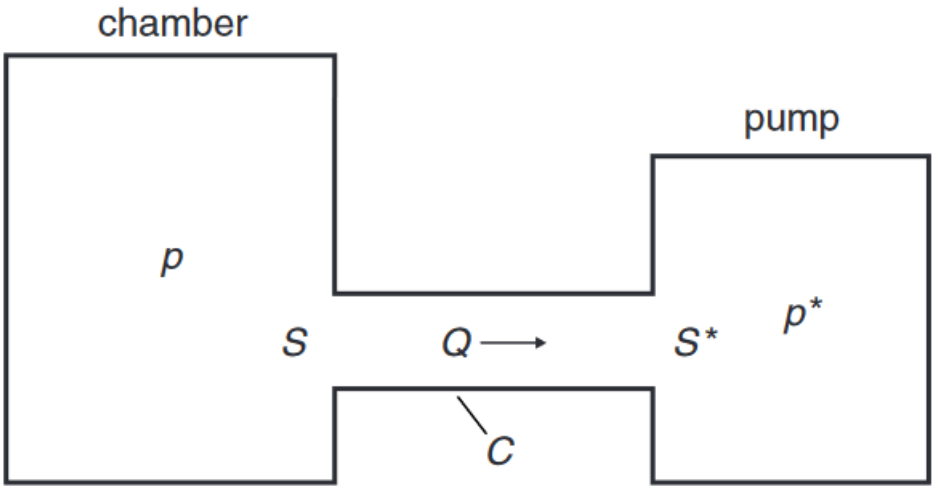

Figure 2. Gas flow between two volumes separated by a pipe. The pumping speed S at the vacuum chamber results lower than S at the pump because of the conductance C in between (Chambers, 2005, p. 82).*

If multiple connecting elements with conductances $C_1, C_2, \dots, C_n$ are installed in parallel between two volumes, the resulting combined conductance is given by the sum of the individual conductances, i.e. (Chambers, 2005, p. 81):

$$C_{parallel} = C_1 + C_2 + \cdots + C_n \qquad 2.15$$

If the connections are instead mounted in series, the resulting total conductance is calculated as the reciprocal of the sum of the reciprocals of the conductances of the individual elements:

$$\frac{1}{C_{series}} = \frac{1}{C_1} + \frac{1}{C_2} + \cdots + \frac{1}{C_n} \qquad 2.16$$

The rule for the serial connection can also be used to estimate the effective pumping speed at the outlet of a vacuum chamber connected to a pump of pumping speed S_{pump}

[8] A process is said to be isothermal if changes in the system such as mass transfer or pressure/volume variations do not involve changes in temperature (Afework, Hanania, Stenhouse, & Donev, 2018).

through an element of conductance C (Jitschin, 2016a, pp. 92-93):

$$\frac{1}{S_{eff}} = \frac{1}{C} + \frac{1}{S_{pump}} \quad \therefore \quad S_{eff} = \frac{S_{pump}}{1 + \frac{S_{pump}}{C}} \tag{2.17}$$

Equation 2.17 shows that, if an element with a small conductance C is interposed between the vacuum chamber and the pump, the effective pumping speed at the chamber outlet results greatly reduced. As a limiting case, if the conductance of the connecting element is much smaller than the pumping speed, the contribution of the pump to the overall pumping speed becomes negligible, and therefore:

$$S_{eff} \approx C \qquad for \quad C \ll S_{pump} \tag{2.18}$$

But by Equation 2.13 and 2.14, this means also that:

$$\begin{aligned} Q &= C\left(p_{chamber} - p_{pump}\right) = S_{eff}\, p_{chamber} \\ \therefore \quad & \left(p_{chamber} - p_{pump}\right) \approx p_{chamber} \\ \therefore \quad & p_{pump} \ll p_{chamber} \quad , \quad for \quad C \ll S_{pump} \end{aligned} \tag{2.19}$$

And therefore:

$$Q = S_{eff}\, p_{chamber} \approx C\, p_{chamber} \quad , \quad for \quad C \ll S_{pump} \tag{2.20}$$

Thus, by interposing a very small conductance between the pump and the vacuum chamber, the gas throughput can be estimated with negligible error by simply multiplying the pressure reading inside the vacuum chamber by the conductance of the element(s) connecting the chamber with the pump, making in many cases the reading of the pressure at the inlet of the pump superfluous. These are important results often exploited during laboratory measurements of outgassing rates.

Knowing the conductance of each connecting element in a vacuum system is therefore of primary importance for the calculation of gas throughputs. Since the pumping speed at the inlet of a pump is normally known, the conductance of an element could be empirically determined by simply measuring accurately the pressure upstream and downstream of it. Combining Equations 2.13 and 2.14 gives, in fact:

$$C = \frac{S_{pump}\, p_{pump}}{p_{chamber} - p_{pump}} \tag{2.21}$$

However, for system design considerations, it is usually necessary to know the conduct-

ance of a component beforehand, therefore its value must be calculated rather than measured. The simplest case is the conductance of an aperture of area A in a thin wall between two vacuum chambers. Assuming that the gas is in the molecular regime, which is the case of interest in HV and UHV systems, the flow is not affected by mutual interactions between molecules and the throughput can be entirely attributed to the difference in impingement rate between the two sides of the aperture (Chambers, 2005, p. 97). If p_1 and p_2 are the pressures on each side, applying Equations 2.2, 2.8 and the definition of throughput leads to:

$$\begin{aligned} Q = p\dot{V} &= \frac{dN}{dt}kT \\ &= A(j_1 - j_2)kT \\ &= \frac{A(p_1 - p_2)kT}{\sqrt{2\pi mkT}} \\ &= \sqrt{\frac{kT}{2\pi m}}A(p_1 - p_2) \\ &= \sqrt{\frac{RT}{2\pi M}}A(p_1 - p_2) \end{aligned} \qquad 2.22$$

Hence, by equation 2.14:

$$C = \sqrt{\frac{RT}{2\pi M}}A \qquad 2.23$$

Thus, the conductance of an orifice can be calculate knowing the molar mass of a gas and the area of the orifice.

For circular pipes and other types of ducts with constant cross section, it is necessary to introduce the concept of *transmission probability*. In molecular flow, a gas particle that crosses the inlet of a duct can undergo two possible situations, illustrated in Figure 3:

1. The initial direction of the particle allows it to directly reach the end of the duct and exit to the other side, or
2. After crossing the inlet, the particle collides into the inner surface of the duct and bounces away in one of several possible directions.

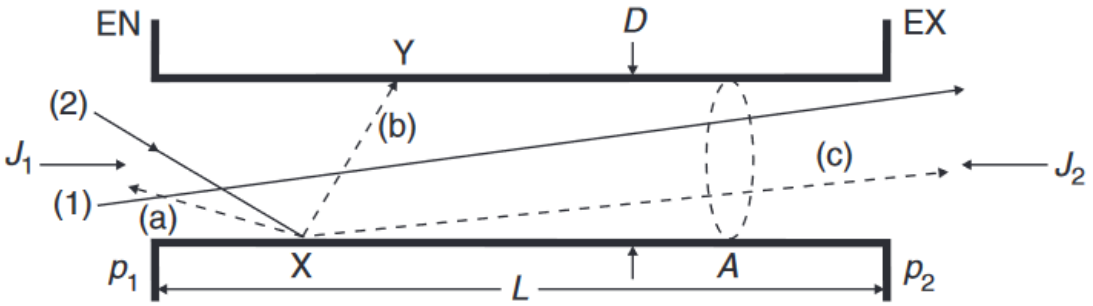

3. *Figure 3. Illustration of the three possible outcomes for a particle entering the inlet of a long duct (Chambers, 2005, p. 99).*

If L is the length of the duct and D is its other characteristic dimension (such as the diameter, in a rounded pipe), the probability of the first outcome to occur clearly diminishes as the ratio L/D increases. On the other hand, if the particle collides with the inner walls of the duct, it might immediately bounce elastically away in a direction that is the specular reflection of its incoming direction, it might directly bounce away inelastically in a direction slightly different than the reflected incoming direction, or it might briefly stick on the surface and be released soon after in a direction determined by a probabilistic law called Knudsen's cosine law, whose formulation is (Greenwood, 2002):

$$dn = \left(\frac{n\bar{v}}{4}\right)\frac{1}{\pi}A\,cos\beta d\omega \qquad 2.24$$

where dn is the molecular flux of gas particles from a surface element of area A having directions within a small solid angle $d\omega$ whose axis makes an angle β with the normal to A. In more simple terms, this law states that, unlike in a specular rebound, the angle of release of a gas particle that sticks on a surface after a collision has a higher probability to be released into a direction close to the normal to the surface, rather than into a shallower trajectory. This implies that, after impinging the internal walls of the duct the first time, the particle has a high probability to bounce randomly many more times inside the duct before exiting from the outlet, and it has even a certain probability to bounce back in the direction of the inlet of the duct, thus effectively contributing to backflow.

If a certain number of molecules cross the inlet of a duct in a given amount of time, the transmission probability represents the percentage of those particles that exit from the outlet of the duct after having passed through it (Chambers, 2005, p. 98-100). Usually denoted with the symbol α, the transmission probability must be multiplied with the conductance of the inlet of a duct in order to correctly compute its overall conductance:

$$C_{duct} = \alpha C_{inlet} \tag{2.25}$$

The transmission probability of apertures in very thin walls can be assumed as being equal to 1, but α decreases as the ratio L/D increases. The exact computation of the transmission probability is quite difficult, and it can be done analytically only for few simple geometries[9]. However, several equations that allow to quickly calculate the value of α with little error have been developed for some of the most common geometries (Jitschin, 2016a, p. 139). For example, for pipes with circular cross section either of the following equations can be used:

$$\alpha = 1 - \frac{L}{D}\,, \quad if\ L \ll D \tag{2.26}$$

$$\alpha = \frac{4}{3}\frac{D}{L}\,, \quad if\ L \gg D \tag{2.27}$$

2.2 Sorption Phenomena

The creation of a vacuum typically requires the removal of gases from a given vessel or chamber, for example atmospheric air. Although relatively easy in principle, the task is made difficult by the presence of gases *adsorbed* on every surface inside the vacuum vessel and in some cases also by gases *absorbed* beneath the surfaces in the bulk of the materials exposed to vacuum. The continuous release of these gases usually necessitates continuous pumping even if the target is just to maintain a given high vacuum level inside a chamber (Hablanian, 1998, p. 59).

Gas particles are said to be adsorbed on a solid surface when, after impinging upon it, they temporarily remain on the surface and therefore leave the gaseous phase. Of the total impinging particles, the fraction of particles that adhere represents the *sticking probability* s, and, by consequence, the probability for a particle to actually bounce back from the surface right after the impact is $(1 - s)$. The sticky probability is influenced by the *surface coverage fraction* θ, that is the fraction of the total surface that is already covered with adsorbed particles or, equivalently:

$$\theta = \frac{\tilde{n}}{\tilde{n}_{mono}} \tag{2.28}$$

[9] Monte-Carlo computer simulations are used to calculate the transmission probability through complex geometries (Chiggiato, 2016, p. 10).

In the above, $\tilde{n}$ is the number of particles per unit area adsorbed on the surface, and $\tilde{n}_{mono} = N/A$ is the total number N of particles that would fully cover the surface of area A if closely packed one adjacent to the other, thus forming a monomolecular layer, or *monolayer* for short. For individual atoms or small molecules, $\tilde{n}_{mono} \approx 10^{15}$ cm^{-2}. The sticky probability s is nearly constant when $\theta < 0.5 - 0.6$ (depending on the gas), but it drops when θ approaches 1, i.e. when almost all the surface is already covered (Jousten, 2016a, p. 229-235).

Gaseous particles may also get absorbed below the surface, by dissolving into the material after adsorption on the surface. Both these phenomena are collectively referred to as *sorption* processes. On the other hand, the outward release of trapped gaseous molecules from the surface of some material is called *desorption*, while the term *outgassing* is a more generic term used to encompass any form of release of gases from a material, such as desorption, diffusion from the bulk and any other type of gas evolution from a surface (ibid.).

2.2.1 Desorption

Depending on the chemical nature of the interacting gas and surface, a gas particle can adhere to the surface either due to dipole or van der Waals forces (physisorption), or due to stronger chemical linkage such as covalent bonds (chemisorption). The binding energy resulting from these forces is referred to as adsorption energy E_{ads}, which is also equivalent to the amount of energy that the adsorbed particles need to receive to desorb from the surface, called desorption energy E_{des}. While for physisorbed species in general E_{des} is less than 0.4 eV per particle, i.e. 40 kJ mol^{-1}, for chemisorbed species $E_{des} \approx 0.8 - 8$ eV per particle, or 80 – 800 kJ mol^{-1} (Jousten, 2016a, p. 229).

Desorption energies are of critical importance in vacuum technology, since they determine the rate at which adsorbed species are released from the internal surfaces of vacuum systems. Species with $E_{des} \leq 71$ kJ mol^{-1} desorb from the surfaces very quickly, becoming irrelevant in usually less than 30 minutes, while species with $E_{des} \geq 105$ kJ mol^{-1} desorb so slowly that they do not cause an important pressure rise inside a vacuum chamber. Molecules with E_{des} in between these two values constitute however a problem, since they can continue to degas from the surfaces of a vacuum chamber for very long time. Unfortunately, the desorption energy of H_2O molecules on stainless steel and aluminium surfaces ranges between 80 kJ mol^{-1} and 104 kJ mol^{-1}, which means that the

outgassing of water vapour from the walls of a previously vented vacuum chamber stays significant for weeks even under continuous pumping, severely delaying the achievement of very low pressures (Jousten, 2016a, p. 240).

One way to speed up this process is intentionally increasing the temperature of the walls of a vacuum chamber, a process called *bakeout*. By providing extra kinetic energy to the adsorbed particles, the number of those whose vibrational energy at any given time is greater than E_{des} results increased, thus speeding up the overall desorption rate from the surface. The latter is indeed dependent not only on the desorption energy, but also on the number of adsorbed molecules per unit area $\tilde{n}$ and on the temperature T of the surface, according to the following relationship (Jousten, 2016a, p. 235-236):

$$j_{des} = \left(\frac{d\tilde{n}}{dt}\right)_{des} = -\nu_0 \tilde{n} e^{\left(-\frac{E_{des}}{RT}\right)} \qquad 2.29$$

In the above equation, ν_0 is the oscillation frequency of the molecules, that can be calculated as:

$$\nu_0 = \frac{kT}{h} \qquad 2.30$$

where h is the Planck constant, equal to $6.626 \cdot 10^{-34}$ m^2 kg s^{-1}, resulting in an oscillation frequency for $T = 300$ K of $\nu_0 = 6.25 \cdot 10^{12}$ s^{-1}, i.e. a period $\tau_0 = 1.60 \cdot 10^{-13}$ s.

Writing $\tau = \tau_0 e^{\left(\frac{E_{des}}{RT}\right)}$, Equation 2.29 can be rewritten as:

$$j_{des} = -\frac{\tilde{n}}{\tau} \qquad 2.31$$

which integrated gives the number of desorbed particles as a function of time:

$$\tilde{n}(t) = \tilde{n}_0 e^{-\frac{t}{\tau}} \qquad 2.32$$

where $\tilde{n}_0 = \tilde{n}_{mono}$, i.e. 10^{15} cm^{-2} if a surface is completely saturated with a monolayer of adsorbed molecules. Rearranging Equation 2.32 and taking the natural logarithm on both sides, the time t necessary for a fraction of the monolayer $f = \tilde{n}/\tilde{n}_0$ to desorb is calculated as:

$$t = -\tau \ln \frac{\tilde{n}}{\tilde{n}_0} = \tau \ln \frac{1}{f} \qquad 2.33$$

Equations 2.29, 2.31, 2.32 and 2.33 are only descriptive of an ideal process, accounting

for just one unique desorption energy for a certain surface-species pair, and neglecting the possibility for some of the desorbed particles to get readsorbed by the same surface before getting pumped out from the vacuum chamber. Unfortunately, in most cases readsorption occurs at least in part; moreover the desorption energies of species such as H_2O seem to take a multitude of values changing from site to site on the surface of a vacuum vessel, resulting in empirically measured net desorption rates that do not follow the expected exponential rule stated in Equation 2.29 (Jousten, 2016a, p. 237-241).

Indeed experiments show that, when mostly due to surface desorption, the pressure and outgassing rates inside a vacuum chamber change according to a power rule resulting from the cumulative effect of several exponential curves attributed to multiple desorption processes, each having different desorption energies[10]. The resulting pressure curves take the form (Chambers, 2005, p. 63):

$$p = p_0 t^{-n} \qquad 2.34$$

where usually n takes values close to 1 and p_0 is the pressure at the unit time (Figure 4).

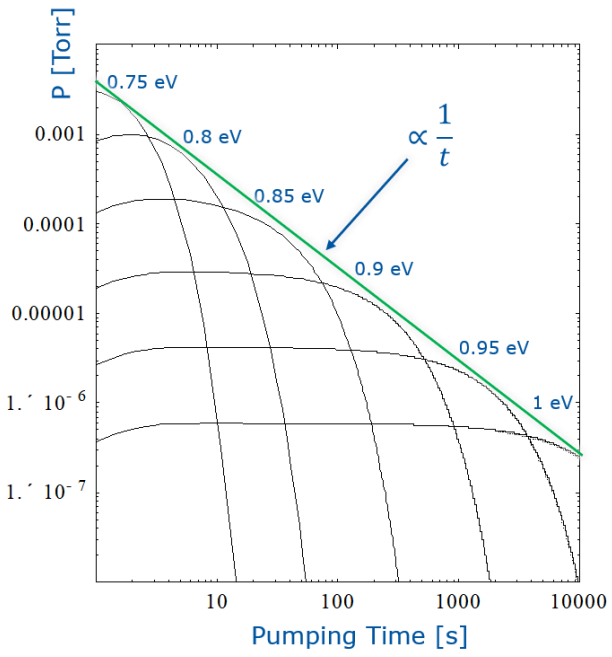

Figure 4. Theoretical exponential pump-down curves for different desorption energies of H_2O on steel, and their cumulative effect resulting in a curve obeying a power rule (Chiggiato, 2017, p. 12).

[10] There is still debate on the exact reason why the rates of desorption of water and other gaseous species follow a power rule instead than an exponential rule. One of the most accepted explanations is that the topological complexity of the surfaces causes the desorption energy to differ from point to point, resulting in a series of concurrent desorption processes characterized by several different τ values, whose cumulative effect results in the empirically determined power rule. However, other explanations involving diffusion processes have also been proposed (Jousten, 2016a, p. 241).

Since gas throughput in a vacuum chamber is proportional to pressure (see Equation 2.13), if the pumping speed is constant, the specific desorption rates of the surfaces inside the chamber can be calculated by dividing the total gas throughput by the area A of the desorbing surfaces, that is:

$$q = \frac{Q}{A} = \frac{S\, p_0\, t^{-n}}{A} = q_0 t^{-n} \qquad 2.35$$

Being inferred from pressure readings, measured desorption rates per unit area, rather than in terms of number of particles per second, are typically expressed in pressure-volume units such as mbar L s^{-1} cm^{-2} (hPa dm^3 s^{-1} cm^{-2}), in which case they are generally referred to as specific outgassing rates, most often denoted by the symbol q. The coefficient q_0 in Equation 2.35 represents a specific outgassing rate value at the unit time (usually 1 hour) that is characteristic of each material (Chiggiato, 2017, p. 6).

Pressure, specific and total outgassing rates are usually plotted against pump-down time in graphs where the values of both the horizontal and the vertical axis are shown in logarithmic scale (log-log plot). In such graphs, curves that obey a power rule like Equations 2.34 and 2.35 display a characteristic straight line shape, whose steepness is determined by the value of the exponent n. While pump-down curves dominated by surface desorption processes typically follow the $p = p_0 t^{-1}$ rule as shown in Figure 4, different curves are obtained if other concurrent outgassing phenomena, such as diffusion of molecules from the bulk, occur inside the vacuum chamber during pump-down.

2.2.2 Diffusion

Atoms and molecules on the surface of a solid can get absorbed and diffuse from the surface into the bulk and vice-versa, by moving through interstitial sites in the crystalline lattice or along grain boundaries inside the solid (Jousten, 2016a, p. 247). When the rate at which these molecules arrive to the surface determines the rate of the desorption process, the latter is referred to as *diffusion-limited* desorption (Chambers, 2005, p. 67).

An important example of this phenomenon is given by the stainless steel, which most vacuum systems are made of: during their production process, all steels absorb high quantities of hydrogen molecules from the atmosphere; the gas trapped inside slowly migrates to the surface and constitutes the main source of residual gas in baked-out vacuum systems that have already achieved UHV pressures (Jousten, 2016a, p. 247).

The migration of particles through the material is driven by a difference in the concentration c of the absorbed particles between different points inside the material, i.e. a concentration gradient, and the process is governed by Fick's two laws of diffusion, the first of which is (Crank, 1975, p. 2):

$$j_{diff} = -D\frac{\partial c}{\partial x} \tag{2.36}$$

which states that the rate of flow of diffusing particles in a direction x is proportional to the concentration gradient along x, and that the flow occurs from points with higher concentration to points with lower concentration, expressed by the negative sign. In the above equation, the constant of proportionality D is called *diffusion coefficient* and has units such as $m^2\ s^{-1}$ or, more often, $cm^2\ s^{-1}$. The concentration c can be function of both space and time (hence the use of the partial derivative), but, if the concentration along the solid does not change with time, then Fick's first law can be expressed as a total derivative, in which case it describes a situation of steady flow across a material.

The second law describes instead how the concentration inside the material changes with time under non-steady conditions, and its complete three-dimensional formulation is (Crank, 1975, p. 4):

$$\frac{\partial C}{\partial t} = D\left(\frac{\partial^2 c}{\partial x^2} + \frac{\partial^2 c}{\partial y^2} + \frac{\partial^2 c}{\partial z^2}\right) \tag{2.37}$$

If there is a concentration gradient only along one direction, let us say the x direction, diffusion is one-dimensional and Equation 2.37 can be written in the simpler form:

$$\frac{\partial c}{\partial t} = D\frac{\partial^2 c}{\partial x^2} \tag{2.38}$$

Thus, at a point x inside a material, the concentration changes in time proportionally to the second partial derivative of c with respect to x.

The diffusion coefficient might change from point to point along the direction of the flow, as it might occur in anisotropic materials or if the coefficient depends on the concentration of the diffusing substance. When D is position dependent, the second derivatives on the right hand side of Equations 2.37 and 2.38 needs to be modified to take this into account. In the one-dimensional case:

$$\frac{\partial c}{\partial t} = \frac{\partial}{\partial x}\left(D\frac{\partial c}{\partial x}\right) \tag{2.39}$$

Some particular solutions of Fick's second law have been analytically found for specific initial and boundary conditions, the most relevant of which, for this study, is the case of a thin slab with an initial uniform distribution of diffusant in its bulk and exposed to very low pressures inside a vacuum chamber. In this scenario, the surface of the side walls is negligible compared to the surface of the main faces, which means that diffusion will occur mostly along the direction normal to them, hence the process can be mathematically treated as a one-dimensional case. Almost immediately after starting the pump-down, the concentration of the diffusant outside the slab becomes much lower than in the slab interior, and it can be essentially considered equal to zero. Additionally, one can assume that the rate of diffusion of the particles to the surface is slower than their rate of desorption from the surface to the vacuum space, so essentially after the beginning of the pump-down, the surface of the slab can be considered free of diffusant, i.e. essentially with zero concentration. Assuming that the diffusion coefficient D stays constant, if $\Omega = [0, l]$ is the spatial domain of the points between the two faces of the slab, c_0 is the initial concentration of the diffusant in its interior before the beginning of the pump-down and l is its thickness, the problem may be summarized as follows:

$$c(x, 0) = c_0 \quad , \quad x \in \Omega = [0, l] \tag{2.40}$$

$$c(0, t) = c(l, t) = 0 \quad , \quad t > 0 \tag{2.41}$$

$$\frac{\partial c(0, t)}{\partial t} = \frac{\partial c(l, t)}{\partial t} = 0 \quad , \quad t > 0 \tag{2.42}$$

$$\frac{\partial c}{\partial t} = D \frac{\partial^2 c}{\partial x^2} \quad , \quad x \in (0, l) \quad , \quad t \geq 0 \tag{2.43}$$

With the given boundary and initial conditions, the solution to this differential equation calculated at $x = 0$ leads to the following formula[11] for calculating the specific outgassing rates at the surface of the slab (Jousten, 2016a, p. 248):

$$q = \frac{4D}{l} c_0 \sum_{i=0}^{\infty} e^{\left(-\frac{(2i+1)^2 \pi^2 D t}{l^2}\right)} \tag{2.44}$$

[11] In the source, instead of the total thickness l, the half-thickness $d = l/2$ is used to write the equivalents of Equations 2.44 and 2.45. Finding the author easier to work with the full thickness in the following sections of this document, the coefficients of these two equations have been adjusted to take into account the different choice for this parameter. Moreover, here the number density n has been replaced with a more generic term c_0, since the same equation can be used to calculate outgassing rates also in moles s^{-1} cm^{-2} or hPa L s^{-1} cm^{-2} by simply expressing the concentration in terms of molarity or n as the ratio p/kT.

The above equation can be well approximated with negligible error by the following two step equation, simpler to compute:

$$q = \begin{cases} \frac{4D}{l}\, c_0 \sqrt{\frac{\pi\tau}{16t}} & for\ t \ll 0.5\tau \\ \frac{4D}{l}\, c_0 e^{\left(-\frac{t}{\tau}\right)} & for\ t \gg 0.5\tau \end{cases} \quad , \quad \tau = \frac{l^2}{\pi^2 D} \qquad 2.45$$

where the parameter τ represents an important time constant characterizing the decay of the outgassing rates (ibid.). When plotted on a log-log graph, either of the two above equations produces a curve like the one in Figure 5, featuring an initial $q \propto t^{-1/2}$ behavior followed by an exponential decay.

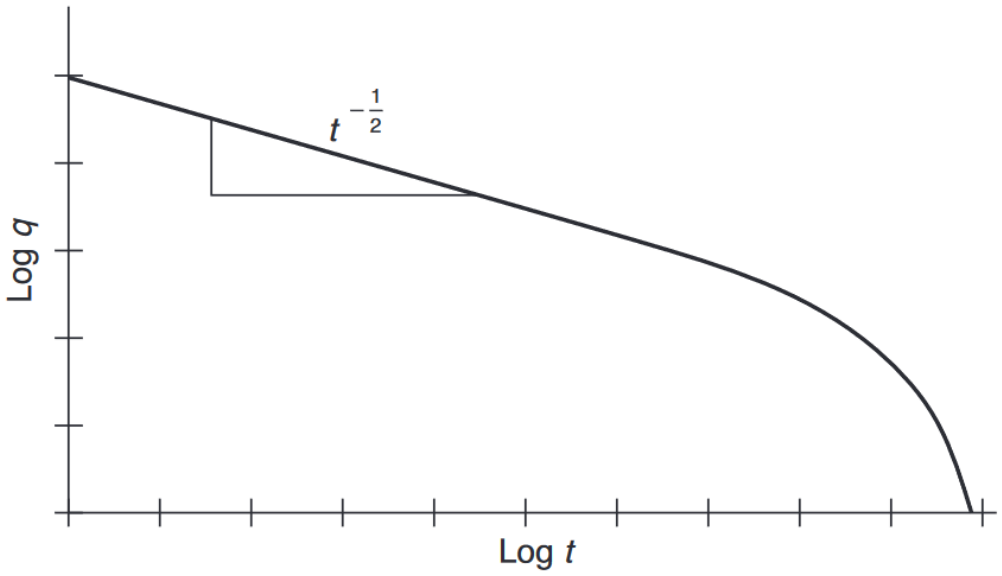

Figure 5. Plot of diffusion-limited specific outgassing rate according to the Fickian diffusion model (Chambers, 2005, p. 68).

Diffusion processes do not always obey the standard Fickian diffusion model. The so-called glassy polymers often exhibit 'anomalous' or 'non-Fickian' behaviour, especially when the diffusing substance causes significant swelling or other structural changes in the material (Crank, 1975, pp. 254-255). The reason for this behaviour is that these polymers barely present any tightly packed crystalline structures in their bulk, because when cooling down from the melt phase they remain “frozen” in a glassy state which is in volumetric and thermodynamic disequilibrium (Tant & Hill, 1999, p. 1-4). Within the glassy state, the molecular chains of the polymer slowly “relax” as a diffusant penetrates inside the amorphous phase of the material, altering the dynamics of the diffusion process itself. Several mathematical models have been proposed by a number of authors to

try to describe non-Fickian diffusion phenomena in these polymers, but no single model is capable of explaining all the experimental observations (Crank, 1975, pp. 257-258). Luckily, most of the observed non-Fickian behaviours arise only under high loads of penetrants causing swelling and/or plasticization of the polymer, phenomena which are not expected to be relevant for the present research work.

A different type of diffusion model, which stems from to the so-called free-volume theories and extends beyond the classical simple Fickian model, is the so called *dual-mode sorption* (DMS) model (Duda & Zielinski, 1996, p. 159), which might be of interest for this study as it has been used with a certain amount of success to explain some moderate discrepancies between the Fickian model and the diffusion dynamics observed in glassy and semi-crystalline polymers. The DMS model, of which more than one version has been proposed (Guo & Barbari, 2009), hypothesizes a dynamic equilibrium based on a dual Fickian transport process by which molecules trapped inside micro-voids distributed throughout the glassy phase of the polymer (Langmuir population) can migrate into the more rigid and dense regions of the material (Henry population) as the concentration in the latter changes and vice-versa (ibid.).

2.3 Pumping Principles and Technologies

2.3.1 The Pump-Down Process

The pump-down, i.e. the removal of air or other gases from a vacuum chamber, is a multi-stage process that start at atmospheric pressure and continues until the achievement of a certain target pressure, which depends on the requirements and purposes of the vacuum system. Ideally, if only the initial gas content had to be removed, the pressure inside a chamber could be reduced to lower and lower values by just adequately extending the pump-down time. In reality, a series of phenomena including desorption, diffusive processes and the possible presence of air leaks from outside the vacuum system prevent the achievement of pressures below a certain limit, and usually require the pumping action to be continued even after the achievement of the target pressure, just to maintain it (Hablanian, 1998, p. 59).

Assuming that a pumping system operates in isothermal conditions, for mass conservation, the change of amount of gas inside a vacuum chamber of volume V during a small interval of time dt must be equal to the amount of gas introduced into the volume by

outgassing, leaks, etc., minus the amount of gas removed from the chamber by the action of the pump. If Q_{in} represents the total mass flow rate accounting for outgassing, leaks, etc. and $Q_{out} = Sp$ is the gas throughput at the outlet of the vacuum chamber, the above conditions can be expressed as a balance equation (Chambers, 2005, p. 108):

$$\begin{aligned} V\,dp &= Q_{in}\,dt - Q_{out}\,dt \\ &= Q_{in}\,dt - Sp\,dt \end{aligned} \qquad 2.46$$

where $V\,dp$ represent the change in amount of gas in the chamber, since the volume V is constant. Dividing both sides by dt the equation becomes:

$$V\frac{dp}{dt} = Q_{in} - Sp \qquad 2.47$$

Integrating Equation 2.47 leads to an expression to calculate the pressure as a function of pumping time:

$$p(t) = p_0\, e^{\left(-\frac{S}{V}t\right)} + \frac{Q_{in}}{S} \qquad 2.48$$

When the pressure is still high, i.e. at the beginning of the pump-down, the term Q_{in}/pV is very small compared to p_0 and Equation 2.48 essentially becomes:

$$p(t) = p_0\, e^{\left(-\frac{S}{V}t\right)} \qquad 2.49$$

which reflects the fact that the pressure drops quite quickly in the early stages of a pump-down, especially after a period of time $t = V/S$. On the other hand, as $t \to \infty$, the term $p_0\, exp\left(-\frac{S}{V}t\right)$ becomes negligible and Equation 2.48 becomes:

$$p(t \to \infty) = \frac{Q_{in}}{S} \qquad 2.50$$

Hence the pressure inside the vacuum chamber stabilizes nearby an asymptotic value.

This value represents the *ultimate pressure* p_u achievable inside a pumping system once reached steady flow, provided that all the residual gas sources inside the sample chamber are known. For instance, if there are no leaks and the outgassing from the internal surfaces is the only process releasing molecules into the vacuum chamber, then the ultimate pressure p_u is:

$$p_u = \frac{Q_{outgassing}}{S} = \frac{q_{outgassing}}{S}A \qquad 2.51$$

where $q_{outgassing}$ is the specific outgassing rate of the surfaces inside the vacuum chamber and A is the total internal area. Of course, if there are multiple residual gas sources, the final pressure is given by the summation of the effects of the various gas flows (Hablanian, 1998, p. 70):

$$p_u = \sum \frac{Q_{in}}{S} = \frac{Q_{outg1}}{S} + \frac{Q_{outg2}}{S} + \cdots \frac{Q_{leaks}}{S} \qquad 2.52$$

2.3.2 Pumps and Pumping Technologies

The removal of gas from a vacuum chamber is carried out by the means of pumps, devices that are capable of extracting gas molecules from a *designated* volume and prevent their return back into it. Most pumps are capable of lowering the pressure to a value that is suitable for a specific purpose (Chambers, 2005, p. 119), but no pump is capable to deal with all the 15 orders of magnitude of vacuum that different applications require, and most pumping devices are efficient only within a specific pressure range (Hablanian, 1998, p. 60). Thus, typically at least two types of pumps are employed to obtain high vacuum: *coarse pumps*, also called *roughing pumps*, are used to evacuate the initial content of gas from a chamber, while *high-vacuum pumps*, also said *fine pumps*, are used to remove the gas evolving from the surfaces (ibid.).

Roughing pumps usually start operating at atmospheric pressure, and therefore they are mostly efficient in the continuum flow regime. They are typically *positive displacement pumps*, which means that they capture discrete amounts of gas from their inlet by the cyclical movement of mechanical parts, then displace and compress the captured gas away from the inlet and into an exhaust that release the pressurised gas to the atmosphere. Rotary vane pumps, scroll pumps, screw pumps and diaphragm pumps are just a few examples of this type of pumps (Chambers, 2005, p. 119).

Positive displacement pumps are widely used either as stand-alone pumping devices to create low and medium vacuums, or as fore pumps used to remove the initial bulk of air from the pumped volume in high vacuum systems – the so-called "roughing" process – and back-up other types of pumps which cannot exhaust the pumped air directly to the atmosphere. Used in such a combination, they are usually referred as *primary pumps*. The major limitation of positive displacement pumps is that they are capable of removing gases only in the range from 100 hPa to about 10^{-3} hPa, and therefore they are not

capable of achieving high vacuum if used alone (Chambers, 2005, p. 120). Another important drawback is that, since they operate mechanical parts cyclically moving with relatively high frequencies, most often they use synthetic oils or other liquids as coolants, lubricants and to seal the moving parts in contact with each other thus to improve compression ratios (Figure 6); these liquids might migrate in the form of vapor or droplets to the pump inlet and from there contaminate the vacuum chamber (Jousten, et al., 2016, p. 261).

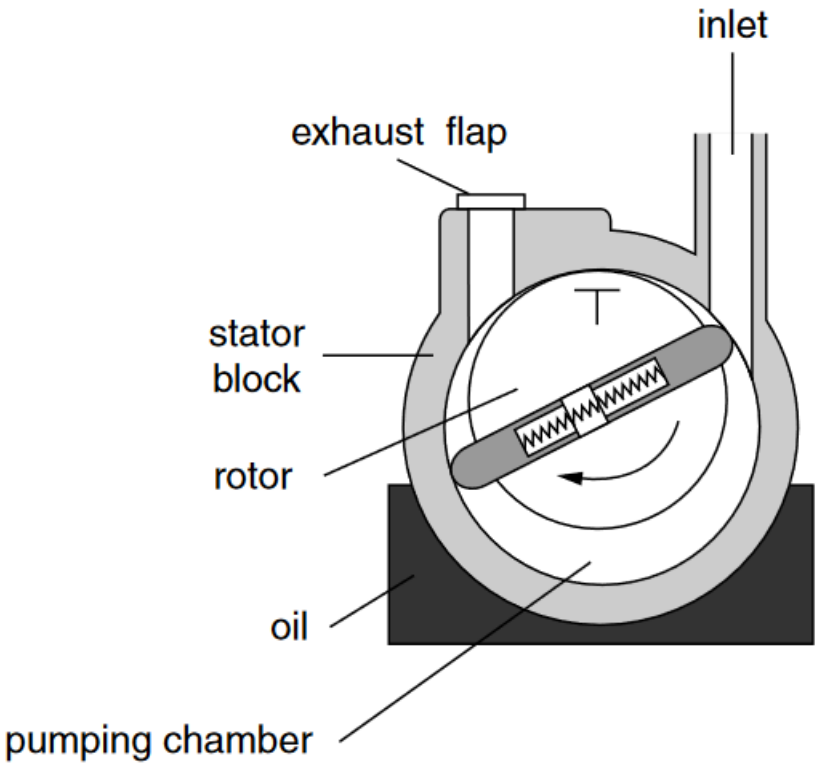

Figure 6. Sectional view of the interior a typical rotary vane pump (Chambers, 2005, p. 123).

Despite these limitations, positive displacement pumps are basically indispensable to HV and UHV systems, since pumps which operate in the molecular flow regime usually cannot achieve their operational pressure range on their own.

Fine pumps are fundamentally different than roughing pumps in that they are usually not efficient if operated at pressures above the HV region. They may or may not have mechanically moving parts and use several different physical and chemical principles to remove gaseous molecules from a vacuum chamber. According to their working principle, they might be divided into two major categories: *momentum transfer pumps* and *capture pump*s (Chambers, 2005, p. 119).

Momentum transfer pumps are devices that transport gases away from a vacuum cham-

ber by providing gas molecules with a velocity component in the direction of the outlet of the pump. The transfer of this velocity component, and therefore of momentum, is carried out either by fast rotating rotors or blades, like in molecular drag pumps and turbomolecular pumps, or by a high-velocity jet stream of a vapor or other fluid, like in diffusion pumps (Hablanian, 1998, p. 60).

The *turbomolecular pump* (TMP) is perhaps the most widespread momentum transfer pump in use today, owing its success to its clean, consistent and reliable operation (Henning, 1998, p. 183).

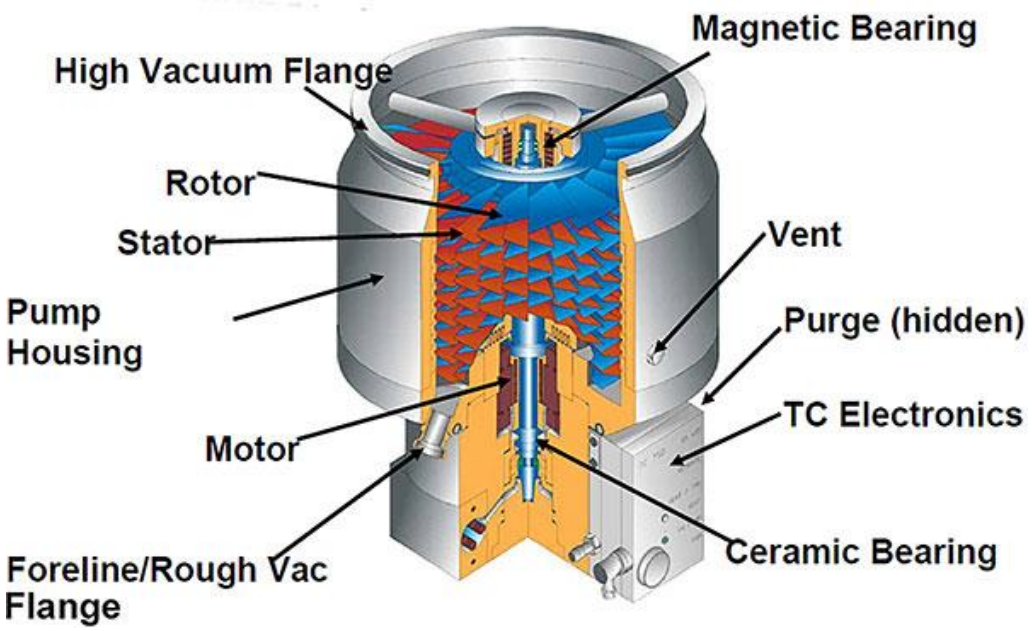

Figure 7. Cutaway view of a turbomolecular pump (Kurt J. Lesker Company®, n.d.).

Below the inlet, a TMP compresses gases by briefly "capturing" by adsorption the gas molecules with a series of fast spinning rotors, whose blades travel with speeds up to 500 m s^{-1}, comparable to the speeds of gas molecules. To achieve these speeds, the rotors typically rotate at frequencies of 1000 Hz and beyond (Chiggiato, 2016, p. 52-54).

A stator whose blades are tilted in the opposite way is placed below each rotor (Figure 7). Once the molecules leave a rotating blade, they are scattered from its surface following the cosine law (see Section 2.1.4), but with an additional velocity component that increases the probability for the molecules to hit the bottom of a blade of the following stator; the orientation of the latter maximises the likelihood that the molecules desorbing from the stator are then captured again by the spinning rotor below it and so on, resulting in a cascade effect that effectively produces a net downstream flow in the direction

of the outlet, where compression occurs.

To operate efficiently, these pumps require the mean free path of the gas molecules to be similar to or larger than the distance between the blades, which occurs at pressures below 10^{-3} hPa. For this reason, they are usually coupled with a positive displacement roughing pump that is used at the initial stages of the pump-down to remove the gas from atmospheric pressure to the medium vacuum region (Henning, 1998, p. 183-184). Turbomolecular pumps can attain pressures in the range below 10^{-10} hPa and maintain constant pumping speed within their optimal operativity range, i.e. 10^{-3} – 10^{-10} hPa. The major drawback of turbomolecular pumps is the fragility of their blades, which, due to their high rotational speeds, can easily get damaged in case of abrupt exposure to pressures above the HV region; additionally, in case of rotor deceleration due to power cut or failure, they are not capable to prevent back streaming of contaminants from the backing pump, demanding therefore the use of additional safety valves and dedicated pressure sensors (Chiggiato, 2016, p. 54-55).

Capture pumps remove particles from the gas phase inside a vacuum chamber by trapping them on surfaces exploiting physical or chemical processes such as condensation, physisorption and chemisorption. These types of pumps have no outlets, since, once trapped, the particles are stored in the condensed state on the designed surface, without leaving the vacuum chamber (Chambers, 2005, p. 118-119). To be effective, therefore, capture pumps need to trap the particles for periods of time longer than the operational time of the device they remove the particles from: in the case of particle accelerators, this might correspond to 2 or 3 years of continuous operational run (Elsen & Bordry, 2018). This is achieved by opportunely extending the particles average *sojourn time* on the trapping surface, which is determined by the Frenkel law (Chiggiato, 2016, p. 55):

$$\tau_s = \tau_0 e^{\left(\frac{E_{ads}}{RT}\right)} \qquad 2.53$$

where E_{ads} is the particle-surface adsorption energy and τ_0 is the average oscillation period of the molecules, which at 300 K is approximately 10^{-13} s (see Section 2.2.1). By Equation 2.53, the sojourn time can be extended either by increasing the adsorption energy, or by decreasing the temperature T of the surface.

The latter route is exploited by *cryopumps*, short for cryogenic pumps, which capture molecules in the gaseous phase by condensation or, for certain gases with very low

freezing point, by adsorption on surfaces held at very low temperature. The required cooling is either achieved by small, laboratory sized refrigerator units, or, in installations such as particle accelerators, by large distribution lines of liquid nitrogen or liquid helium (Chambers, 2005, p. 162). Due to the inevitable accumulation of molecules on their pumping surfaces, cryopumps require periodic regeneration (carried out by heating the pump to room temperature) to remove the adsorbed or condensed gases in order to avoid the formation of an excessively thick deposit which would act as an insulating layer, reducing the pumping efficiency. For the same reason, these pumps need to operate in the molecular regime in order not to clog too rapidly their capturing surfaces with molecules, hence they can be used only as secondary pumps, in conjunction with other types of pumps (Chiggiato, 2016, p. 66).

While cryopumps rely mainly on physisorption to operate, *getter pumps* use predominantly chemisorption to trap particles on a designed surface, using a combination of adsorption, absorption and chemical bonding processes (Jousten, 2016b, p. 472). Examples of getter pumps are sublimation pumps, non-evaporable getters (NEGs) and sputter-ion pumps, all used in UHV applications.

Sublimation pumps work by deposition of a layer of reactive metal (getter) on selected surfaces inside a vacuum chamber. The metal is usually titanium, deposited by a high temperature source such as a filament traversed by a strong current. The titanium sublimates from the solid state directly into the vapor phase, depositing onto the nearby target surface, which acquires pumping capability. The high reactivity of the metal assures that impinging molecules of a wide range of gases are trapped on the surface through chemisorption, but as the coverage of the surface increases, the pumping speed of the surface decreases, thus the sublimation process needs to be repeated regularly (flashing) in order to maintain an high average rate of pumping. Sublimation pumps cannot operate at pressures above 10^{-4} hPa, since under these conditions a strongly bonded surface layer of titanium oxides and nitrides forms on the surface of the sublimator itself, preventing most of the sublimation process to happen (Singleton, 1998, p. 243-244).

Non evaporable getters, usually abbreviated as NEGs, function upon the same principle of the sublimation pumps, capturing a wide range of residual gases occurring in UHV vacuum chambers by binding them chemically on some very reactive surface. NEGs can either be applied as cartridges and strips inside special devices or locations exposed

to the vacuum, or directly deposited on the internal surfaces of a vacuum chamber. In this second case, the difference with the layers deposited by a sublimation pump is that NEGs coatings are usually applied ex-situ only once via magnetron sputtering deposition. This technique exploits the sputtering of atoms from a target material to a substrate caused by the impacts of ionized atoms or molecules of an inert gas (i.e. a plasma) such as argon onto the negatively charged target; both an electric and magnetic field are applied between the target and the substrate, causing the electrons in the plasma to move in long spiral paths in the region between target and substrate, which results in a high rate of secondary ionisation of the gas particles, and, by consequence, high impact and deposition rates (Gould, Kasap, & Ray, 2017, p. 661-662).

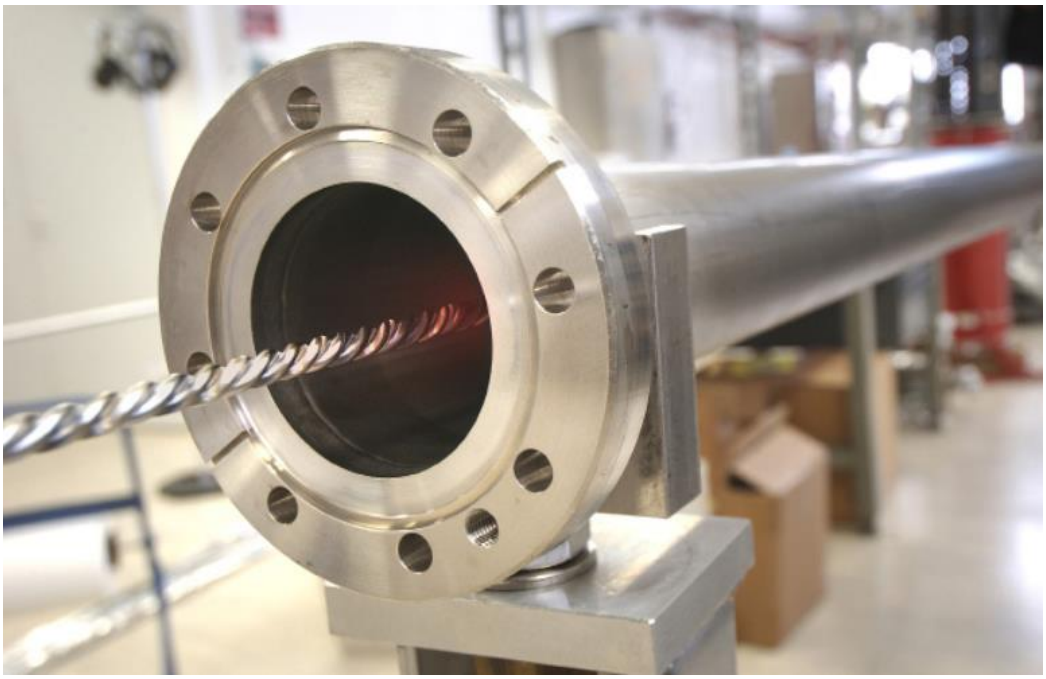

Figure 8. A vacuum chamber of the LHC after being coated with a thin NEG layer (CERN, n.d.).

Made of alloys of zirconium, titanium, hafnium and vanadium, all of which are very reactive metals (Chiggiato, 2016, p. 62), NEGs form a passivated layer of carbides and oxides on their surfaces upon exposure to air. However, this layer can be dissolved into the substrate by a procedure called “activation” executable in-situ after installation, and consisting in heating the material to a suitable temperature for a specific amount of time, which depends on the particular NEG type: ca. 1 hour at 350-450°C for Zr-V-Fe alloys typically available on the market (Chambers, 2005, p. 173-174), and ca. 24 hours at 180-200°C for a Ti-Zr-V alloy specially developed at CERN for its accelerators (Costa Pinto, 2013, p. 14). A similar thermal cycle can be used to regenerate the surface

of the NEG once saturated with adsorbed particles: this process, called “reactivation”, is repeatable several times, thus eliminating the need for multiple and frequent recoating procedures.

NEG pumps are very effective at trapping residual gases such as N_2, O_2, CO_2 and CO through surface chemisorption. Additionally, they are also capable of trapping hydrogen gas that, after being adsorbed on the surface as H_2 molecules, dissociates into individual H atoms and diffuses into the bulk of the coating (Chambers, 2005, p. 174). This is particularly important since most turbomolecular pumps that are used to achieve UHV pressures have a quite modest compression ratio value for H_2 gas and struggle to contain back streaming of these molecules back into the evacuated volume (Chiggiato, 2016, p. 54). On the other hand NEGs are relatively inactive with noble gases and stable, non-polar molecules such as CH_4 (methane), which represents their major limitation (Jousten, 2016b, p. 476).

Ion getter pumps, also called *sputter-ion pumps* or simply *ion pumps*, are devices that exploit a gas discharge mechanism to create ions that are accelerated by a strong electric field against a cathode made of a getter material such as titanium, were they remain implanted under a few atomic layers. As a secondary effect of these collisions, titanium atoms in the cathode get sputtered into the surrounding surfaces, effectively creating a getter coating on them. At the same time, some of the ionized particles neutralize their charge upon colliding with the cathode and bounce back at high speed, implanting into the surrounding surfaces, where they can get buried by successively sputtered atoms coming from the cathode. H_2 molecules that have been implanted into some surface also diffuse into the bulk thanks to their high solubility in metals (Jousten, 2016b, p. 494).

Because of this gettering implanting and diffusive combined action, ion pumps are ideal to remove from a vacuum volume residual gases difficult to eliminate with other pumping techniques such as methane and noble gases (Jousten, 2016b, p. 493) and for this reason they are often used in combination with turbomolecular and NEG pumps on already baked systems, since they allow to attain extremely low pressures at the bottom limit of the UHV region (Chambers, 2005, p. 176, 181).

Sputter ion pumps are usually assembled as arrays of several small units called *Penning cells*, a particular kind of discharge cell that is used also in a type of vacuum gauges of the same name, which will be discussed in the following section.

2.4 Vacuum Measurements

Conducting measurements on a vacuum means identifying the properties of the rarefied gaseous particles that are confined inside the sealed volume of a vacuum chamber. Although the term “pressure” is usually employed to classify the magnitude of various types of vacuum, it must be noted that, below a certain threshold, the concept of pressure as force per unit area becomes nearly meaningless, especially when the gas becomes so rarefied that it stops behaving like a continuum medium. In the HV region and below, the forces that the particles exert on the walls of the vacuum chamber are so minuscule that not only they are negligible, but they are very difficult to detect (Jousten, 2016c, p. 565). So, while it is still possible to use the concept of force on a surface to *directly* measure the pressure in the rough vacuum region, most of the time in HV and UHV applications the pressure is measured *indirectly* by devices exploiting a series of physical phenomena that can be related to the number density of the gaseous species inside the volume they are monitoring (Figure 9).

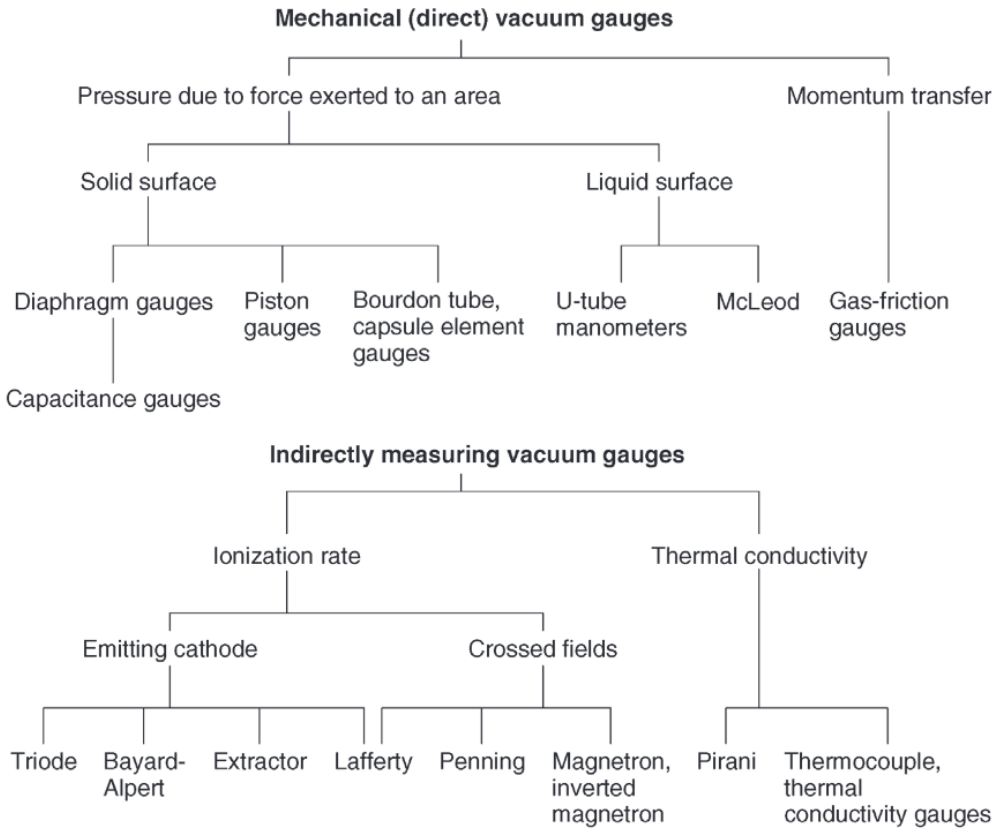

Figure 9. Direct and indirect methods to measure vacuum pressures (Jousten, 2016c, p. 566).

Therefore, in the field of vacuum technology, the measure of pressure is most often related to the *counting of particles* present in a certain region, i.e. their number density,

according to the definition of pressure $p = nkT$ given us by the kinetic theory of gases.

Beside the measurement of pressure, it is often very important to identify the composition of the gas mixture inside the evacuated volume, since it can provide information about the nature and origin of the outgassing processes, allow to assess the cleanness of the vacuum system and help discovering the presence of air leaks. Thus, specialized equipment is also required to perform mass spectrometric analysis of the residual gases.

2.4.1 Pressure Measurement and Vacuum Gauges

No single gauge can measure pressures which span 15 orders of magnitude, from the 1000 hPa of the atmosphere down to the 10^{-12} hPa created in some laboratories and particle accelerators. Therefore, several different types of gauges exist, each most suited to measurements within a specific pressure range (Figure 10).

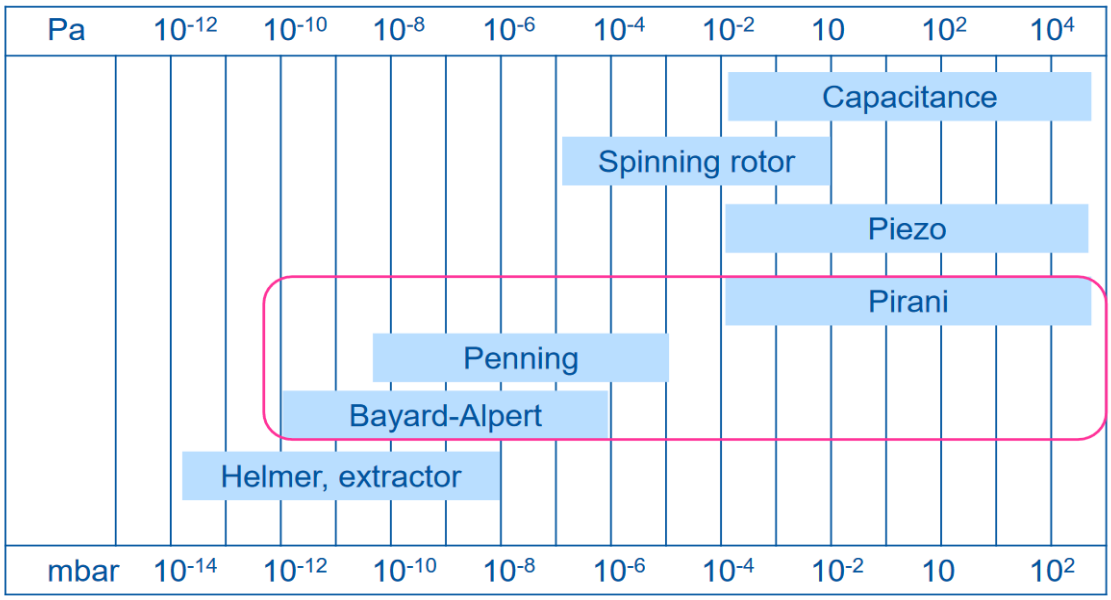

Figure 10. Operational range of the most common pressure gauges used in UHV (Baglin, 2019, p. 41).

The *Pirani gauge* is commonly used from atmospheric pressure down to ca. 10^{-4} hPa. Its operating principle is based on the dependence of the thermal conductivity of gases on the pressure, which is approximately linear in the region 10^{2} – 10^{-3} hPa. In its most accurate version, a resistor under vacuum is heated at a constant temperature, and the heating current required to keep the temperature stable gives an indirect reading of the pressure. Alternatively, the current can be kept constant and the variations in temperature can be measured instead (Jousten, 2016c, p. 594). Although useful to monitor pressure changes in the medium vacuum region and as a reference at the start of most pump-

down procedures, Pirani gauges are not accurate above ca. 10 hPa and below 10^{-3} hPa.

The *Bayard-Alpert gauge*, a type of hot cathode gauge, can be used to perform pressure measurement from about 10^{-6} hPa down to about 10^{-12} hPa. Electrons emitted by a hot filament (the cathode) are accelerated by the electrical field generated by a positively charged cylindrical grid (the anode); most of the electrons pass through the grid several times before being captured by the anode, tracing intricate paths and colliding on their way with some of the gas molecules inside the grid, ionizing them. The gas ions are then attracted by the central collector wire which is kept at a ground potential, creating a current i_{ions} which is proportional (by a factor K) to the electron current crossing the grid i_e and the gas density, i.e. the pressure (Chambers, 2005, p. 206-207):

$$i_{ions} = Kpi_e \qquad 2.54$$

Hence the pressure can be measured as:

$$p = \frac{i_{ions}}{Ki_e} \qquad 2.55$$

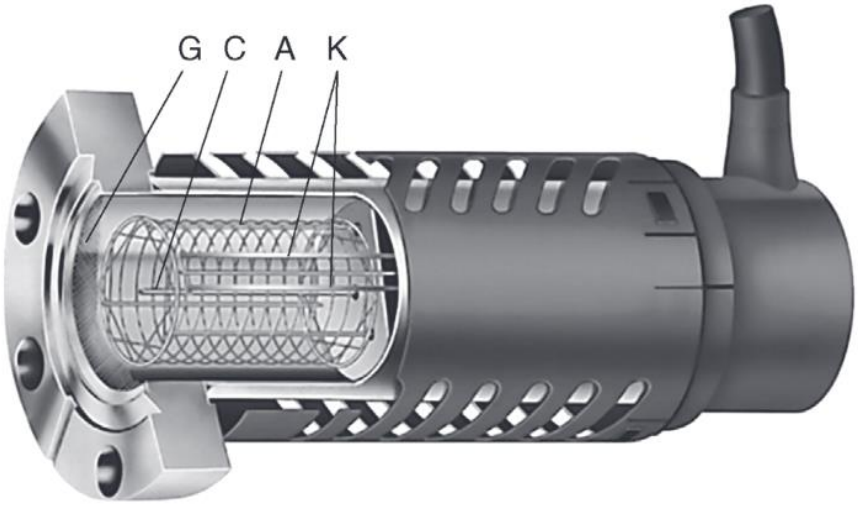

Figure 11. A Bayard-Alpert gauge. K: cathodes; A: anode; C: ion collector; G: grounding (Jousten, 2016c, p. 617).

The *Penning gauge* is commonly used in the range 10^{-5} – 10^{-10} hPa, although it can give (inaccurate) reading also slightly above and below this range. It is a so-called cold cathode gauge, since it does not use hot filaments to ionize gas molecules. This is instead achieved via gas discharge in a Penning cell: an anode is placed between two cathodes connected in parallel, and a strong voltage of a few kilovolts is maintained between the anode and the cathodes, stripping electrons from the surrounding molecules via field

emission (Baglin, 2019, p. 43).

A magnetic field caused by a permanent magnet external to the cell and whose field lines are parallel to the anode traps the electrons between the cathodes, forcing them to rotate in spirals around the anode. This in turn contributes to ionize more gas molecules in the surrounding volume, creating a current of positively charged ions that flows towards the cathodes where they are neutralized. The measured ion current depends on the gas density, i.e. the pressure, according to the following relationship:

$$p = K(i_{ions})^m \qquad 2.56$$

where K is a proportionality constant and $m = 1 – 1.4$ depending on the specific design of the gauge (Jousten, 2016c, p. 625).

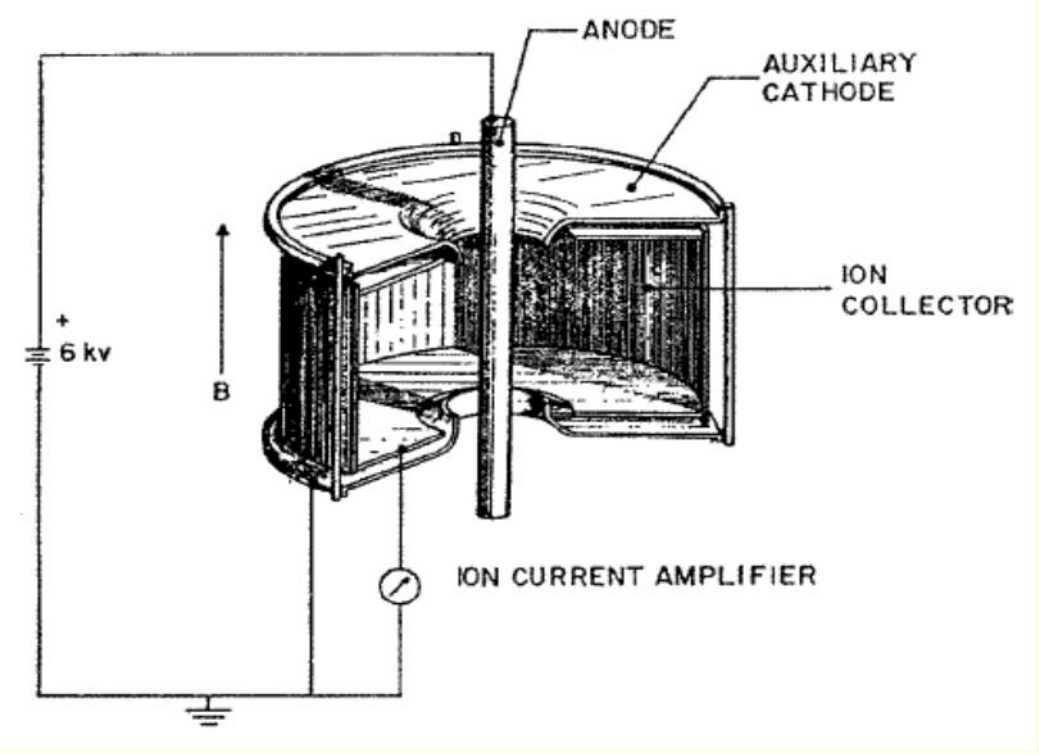

Figure 12. The structure of a Penning gauge (Baglin, 2019, p. 43).

In general, during a pump down that starts from atmospheric pressure and continues in the HV or UHV region, at least two or three different types of gauges are used to keep track of the pressure inside the monitored vacuum chamber. The pressure readings in the LHC vacuum system are provided by 170 Bayard-Alpert gauges, 442 Pirani gauges and 642 Penning gauges (Jimenez, 2008). For outgassing measurements in laboratory test benches, the pressure readings in the low and medium vacuum regions are not of great interest, hence Pirani gauges, despite their low accuracy, are sufficient to monitor

the systems and warn in case of unexpected problems. Special types of gauges that work efficiently within specific pressure windows might be installed to compensate the deficiencies of the most common types gauges, if required by the experiment.

2.4.2 Mass Spectrometry

In vacuum technology, mass spectrometry is performed by the means of devices called partial pressure analysers, more usually referred to as *residual gas analysers* (RGAs). An RGA ionizes and fragments gas molecules by impacting them with electrons, then filtering the various types of ions so produced by their mass to charge ratio, and finally neutralizing their charge in a detector (Figure 13). Selectively filtering different types of ions in succession, it is possible to obtain information about their relative amounts by comparing the relative intensity of the currents detected for each mass/charge value (Chambers, 2005, p. 221-222).

Figure 13. The operational principle of a residual gas analyser.

The ionization process is similar to the one employed in hot cathode gauges; a hot filament emits electrons that are attracted by an anode, impacting gas molecules during their path; the ions are then directed by the electrical field towards slotted plates that collect and focus the ion beam into the filtering device (Jousten, Ellefson, & Grosse Bley, 2016, p. 644). The latter consists of four parallel cylindrical metal rods arranged in a square array (quadrupole) and electrically connected so that opposite pairs are at the same potential, which is the sum of a DC component V_0 and an alternating component $V_1 \, cos \, \omega t$ with a frequency ω of a few MHz (Chambers, 2005, p. 224). The ions arriving from the focusing plate are injected alongside the axis in between the rods and are affected by the electrical field that forces them to move in an oscillatory path. Depending on the intensity of the currents, only certain ions with specific mass/charge values can pass through the quadrupole without being ejected or impacting one of the rods, hence, by adjusting the currents, the filtering action is obtained (Jousten, Ellefson, & Grosse Bley, 2016, p. 657). The ions are finally collected on the other hand of the quadrupole by a Faraday cup (the detector) which neutralizes the charge of the ions, thus producing an electrical signal that is proportional to the rate at which each particular ion

arrives. Most RGAs are also equipped with a multiplier exploiting secondary electron emission, to which the flow of ions can be deflected when the intensity of the currents is too low to be adequately detected by the Faraday cup, which happens when the pressure in the vacuum chamber is below a certain threshold (Chambers, 2005, p. 229).

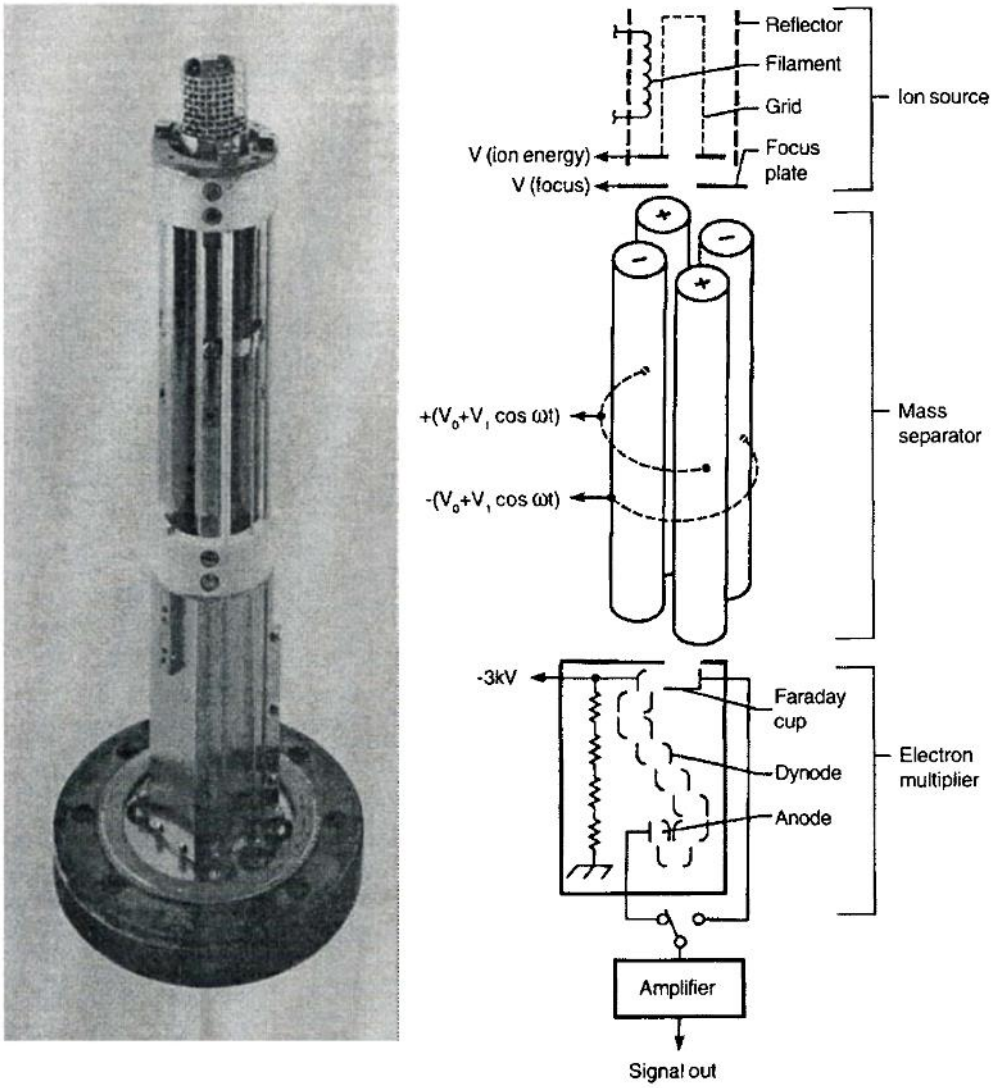

Figure 14. Structure and a schematic representation of a quadrupole mass spectrometer (Outlaw, 1998).

2.5 Overview of Polymers

2.5.1 General Aspects

Polymers are very large molecules composed by a long sequence of repeating units called monomers, from which they are usually named upon[12]. They are found abundant-

[12] The nomenclature of polymers is not uniform. Although the IUPAC has established some systematic

ly in nature, in the form of lignin, cellulose, starch; even molecules essential for life such as DNA and RNA are polymeric in nature. However, polymers can also be artificially synthetized in laboratories and production plants using a variety of chemical reactions and synthesis techniques collectively referred to as *polymerization processes*, which can be broadly classified in the two major categories of step-growth polymerization and chain polymerization (Saldıvar-Guerra & Vivaldo-Lima, 2013, p. 3, 9-10).

The average number of monomeric units repeating in a polymeric molecule is called *degree of polymerization*, which might be very large, often in the order of 10^4 – 10^5. These long molecules can have the structure of mainly *linear chains*, or they can have a *branched* structure in which secondary shorter chains of regular or irregular length can laterally protrude from the backbone of the main chain. Polymers can also have a *cross-linked* structure, in which branched structures of one molecule are linked together with the ones of other molecules, practically forming a unique, very large molecular network extending throughout the volume of the macroscopic object the polymer forms (Teraoka, 2002, p. 1-2).

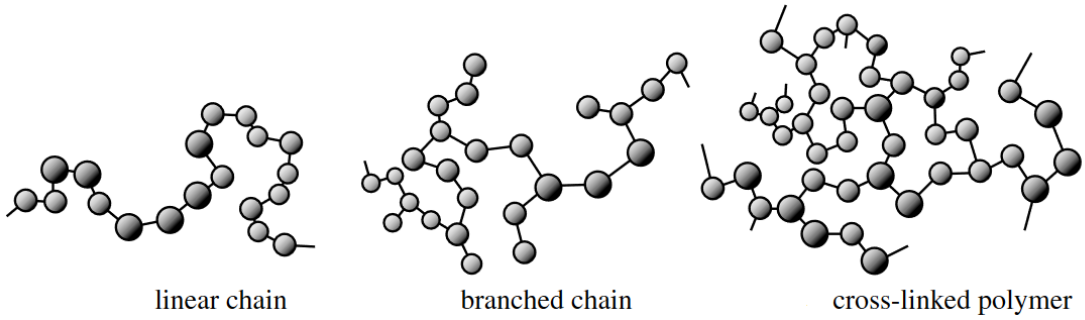

Figure 15. The three possible molecular structures of polymers (Teraoka, 2002, p. 2).

Depending on their structure, polymer molecules can pack together either in a disorganized way, forming amorphous regions, or in more organized arrays forming crystalline structures called crystallites: in both cases, little voids are left between the molecules (Teraoka, 2002, p. 1). The formation of crystallites is favoured by structural regularity and the existence of strong intermolecular forces, such as hydrogen bonds (Saldıvar-Guerra & Vivaldo-Lima, 2013, p. 5). However, since polymeric chains are very long, it is impossible for the molecules to completely fit into nearly perfect arrangements like in low-molecular-weight materials, hence both crystalline and amor-

rules for the naming of polymers, they are not universally adopted, and for some polymers common or commercial names are almost exclusively used instead (Saldıvar-Guerra & Vivaldo-Lima, 2013, p. 12).

phous regions are usually found in such polymers (Figure 16), which therefore should be more appropriately called semi-crystalline. Conversely, completely amorphous polymers are common, such as atactic[13] polystyrene and poly methyl methacrylate (ibid.). These polymers usually have highly branched chains whose randomly varying location of the branches prevent regular packing (Painter & Coleman, 1997, p. 6). The amount of crystalline regions found in the bulk of a polymeric material, expressed in percentage, is called *degree of crystallinity* (Fakirov, 2017, p. 103-105).

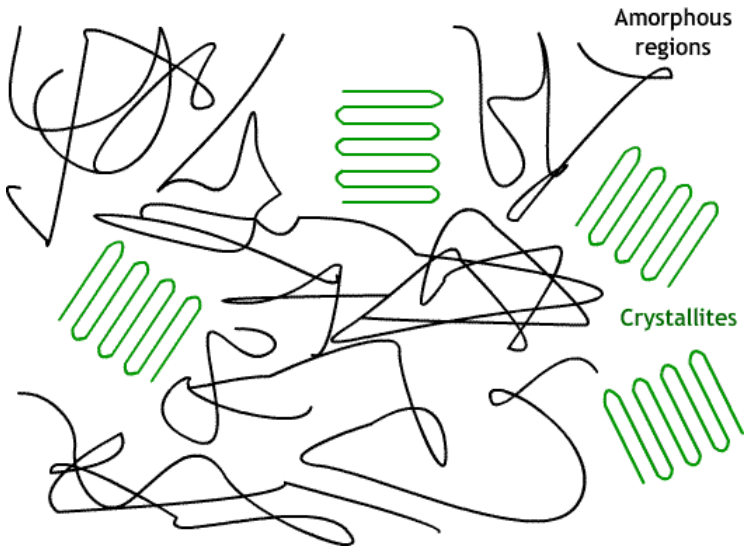

Figure 16. Crystallites embedded in an amorphous polymeric matrix (University of Cambridge, nd).

Structure and degree of crystallinity in polymers are responsible for several of their properties. In first place, they determine their phase transitions behaviour: below a certain temperature, called *glass transition temperature*, or T_g, the amorphous regions of a polymer are in a glassy state in which the molecules are frozen in place, despite not being in the thermodynamic equilibrium typical of crystalline arrangements; the bulky nature of the polymeric chains and their entanglement prevent them to move or rearrange. If heated above the T_g, however, these amorphous regions gain motility, exhibiting a second order phase transition that, at the macroscopic level, manifests as softening and becoming more elastic. On the other hand, crystalline regions do not display increased motility until reaching a true melting temperature T_m, when they undergo a first order phase transition. Thus, while polymers with low degree of crystallinity transit gradually

[13] As it will be explained at page 53, tacticity is the general arrangement of substituent groups on the sides of a polymeric chain. The term *atactic* is used for polymeric molecules whose side substituents are distributed without any regularity on either side of the chain (Painter & Coleman, 1997, p. 9-10).

from the solid to a viscous-liquid state as their temperature is raised above the T_g, highly crystallized polymers experience a more abrupt change in mechanical properties only nearby their melting point, and polymer with intermediate crystallinity display a behaviour somewhat in between (Painter & Coleman, 1997, p. 208-212).

Semi-crystalline polymers display both a T_g and a T_m, while completely amorphous polymers display only a T_g. Crosslinked polymers do not show any glass transition temperature, nor they do melt: their molecules chemically bonded in an extended network are essentially immobilized, thus flow is not possible in such a state (Painter & Coleman, 1997, p. 4). Relatively to the above-mentioned characteristics, polymers are usually classified in three categories (Saldıvar-Guerra & Vivaldo-Lima, 2013, p. 8):

- *Thermoplastics*, or simply *plastics*, are non-cross-linked amorphous and semi-crystalline polymers that are usually below their T_g at room temperature and therefore they appear as hard solids, but they can be melted upon heating and reshaped through thermoforming processing methods.
- *Thermosets* are polymeric materials which have undergone extensive cross-linking; these materials are usually harder and more resilient than thermoplastics, but they cannot be melted without degradation and therefore they cannot be reshaped by heating.
- *Elastomers*, or *rubbers*, are polymeric materials which are usually above their T_g at room temperature, and thus they are quite soft and elastic and display high toughness and impact resistance. They might be slightly cross-linked or not.

Crystallinity and molecular arrangements are usually depending on the type and distribution of the monomeric units that form the backbones and branches of polymeric molecules. These can be of a unique type, like in polyethylene, for which the term *homopolymer* is used, or they can be two or more different monomers, in which case the material is called *copolymer* (Painter & Coleman, 1997, p. 8). A typical example of copolymer is acrylonitrile butadiene styrene (ABS).

Many of the mechanical and chemical properties of polymeric materials depend on the particular type of monomeric units used to synthesize them and, for copolymers, on their distribution and arrangement along the molecular chains. The polymerization method also plays a major role in the determination of the final properties of a polymer, since it can determine the degree of polymerization, the residual presence of solvents,

unreacted monomers or catalysts inside the material, and the *tacticity*, i.e. the arrangement of the functional groups alongside the chain (Fakirov, 2017, p. 20-27), on which the crystallinity of the polymer might greatly depend.

The final properties of polymeric materials are also determined by their particular processing history, which sometimes have an influence even on the geometry, size and opticality of the final product. For example, extruded polymers are characterized by one or two-dimensional orientation of their molecular chains, which has an important influence on their tensile properties; injection molding imposes restrictions on the wall size of items and the rate of cooling from the melt state in general affects the degree of crystallinity of the polymer, which in turn might determine some of the optical properties of the material, such as its clarity (Ramos-de Valle, 2013, pp. 451-457; Aguilar-Vega, 2013, pp. 426-427; Fakirov, 2017, pp. 324-325; Painter & Coleman, 1997, p. 6).

2.5.2 Outgassing of Polymers

Due to their high outgassing rates, the use of polymers in vacuum systems of particle accelerators is limited to only few specific applications such as sealings, electrical insulators, supports, etc., and in general they are avoided in UHV (Chiggiato, 2016, p. 28).

Technical and economic reasons, however, demand for an increased use of this class of materials in the foreseeable future: design studies for more efficient, powerful, and perhaps much bigger accelerators (Gianotti, 2018) pose the challenge of building machines and components with significantly improved performance at a reasonable cost. This urges the R&D departments of particle accelerators laboratories such as CERN to develop new types of seals, feedthroughs and multilayer insulators which might include the use of polymeric materials, that therefore have to be properly selected and characterized (Savary, et al., 2019, p. 63).

Polymers such as PEEK (polyether ether ketone), Vespel® and Kapton® (polyimides) are already employed in vacuum equipment as they are among the polymers with the lowest known outgassing rates[14] also capable of resisting bakeout temperatures of 150 – 200 °C. Unfortunately, the available information about the outgassing behaviour of these materials is quite limited, and the data usually do not allow to fully predict or

[14] According to some trustworthy databases such as NASA's "Outgassing Data for Selecting Spacecraft Materials", see: https://outgassing.nasa.gov/

quantify the impact that a more extensive use of components made of these polymers could have on the quality of the vacuum in HV and UHV systems.

Indeed, only a few sparse studies have been conducted so far on this subject. In 1967, Hait (1967) investigated the outgassing behaviour of gaskets made of polyimide and discovered that the material releases significant amounts of water vapour after being exposed to air, due to its high hydrophilicity. A study conducted at CERN (Chiggiato & Kershaw, 2010) showed that also PEEK releases mainly water molecules under vacuum, even after several hours of bake-out at mild temperatures (100-150 °C). This behaviour was again observed in PEEK, Vespel® and Kapton® samples during subsequent studies by Battes et. al. (2018) and Riihimäki (2019).

In a study on the solubility and diffusion of water in PEEK, Grayson (1987) described the sorption and desorption processes in this polymer in terms of Fickian diffusion; likewise, Han et. al. (1998) found that the sorption and diffusion mechanisms in polyimide films were nearly Fickian. Although polymers might often deviate from this behaviour (see Section 2.2.2), especially when large amounts of permeant cause significant changes in the polymer structure (swelling), it seems at least reasonable to assume that, at low concentrations, the outgassing behaviour of the above-mentioned semi-crystalline polymers could be satisfactorily described by the Fickian diffusion model.

3 MATERIALS AND EXPERIMENTAL PROCEDURES

3.1 Samples Information

Three unfilled grades of the polymers selected for the study have been purchased from the supplier Goodfellow[15]: Kapton® HN, Vespel® SP-1, and PEEK 450G. Both the Kapton and the Vespel are produced by DuPont™, while the PEEK is produced by Victrex™. All three polymers are very good thermal and electrical insulators, have high tensile strength and stiffness, and display much higher thermal resistance than most other thermoplastics. The technical data sheets (TDSs) of the three materials are provided in Appendix A at the end of this document.

PEEK is a linear aromatic polymer belonging to the family of the polyaryletherketones,

[15] https://www.goodfellow.com

whose molecular structure is shown in Figure 17. It is a largely linear, semi-crystalline polymer, whose aryl and ketone groups provide stiffness to the material, while the ether groups provide toughness (Grasmeder, 2019).

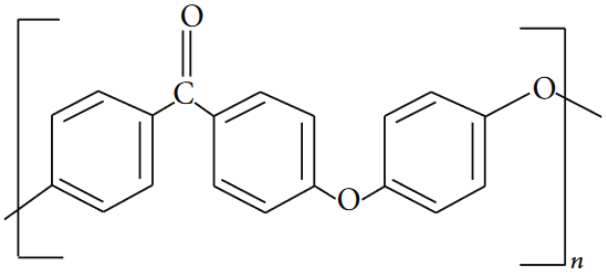

Figure 17. Molecular structure of PEEK Polymer (Najeeb, et al., 2015).

PEEK exhibits a T_g at 143 °C, but has a useful operating temperature up to 260°C and melts at 343°C. Despite its very high melting point, this polymer can be processed using conventional thermoplastic techniques such as injection molding, and extrusion. It is machinable, flame resistant and highly unreactive; furthermore, it resists gamma and electron beam radiation and it is transparent to X-rays (Grasmeder, 2019). According to its TDS and other available sources (de Rooij, n.d.), under normal conditions the water content of PEEK is expected to be in the range 0.31 – 0.45% (by mass).

Kapton® and Vespel® are two semi-crystalline polyimides sharing the same basic molecular structure shown in Figure 18 (Spurgeon, 2018, p. 6; Hrabovsky, et al., 2019).

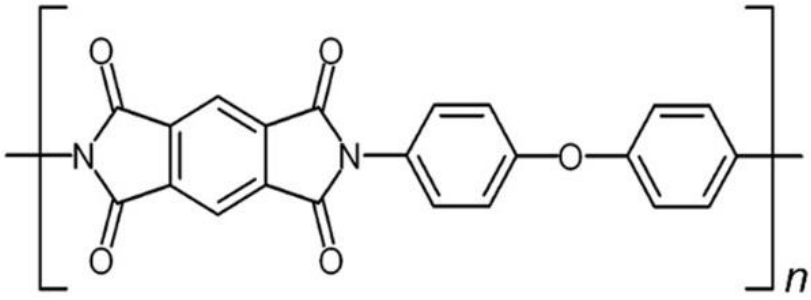

Figure 18. The repeating unit in the molecular chains of Kapton and Vespel (Hrabovsky, et al., 2019).

The imide groups confer to these polymers exceptional thermal stability, making them capable to withstand temperatures in excess of 400 °C (McKeen, 2008, p. 213-216), temperature above which they start undergoing thermal degradation (Tsukiji, Bitoh, & Enomoto, 1990). They do not melt, nor exhibit a clear T_g, feature that makes them mechanically stable even at temperatures above 260 °C (Kemmish, 1995, p. 21).

Due to the lack of a melting point, the polyimide must either be produced directly as a

film (Kapton®) at the synthesis stage (Perabo, 2018), or shaped into a semi-finished form (Vespel®) with sintering techniques (Kemmish, 1995, p. 22). According to the information retrieved from TDS and other sources, moisture content of these two polymers at equilibrium with the atmosphere is expected to be 1-1.3% for Vespel® and 1.3% for Kapton® (de Rooij, n.d.; NASA, 2018).

The PEEK and the Vespel® were received as rods with diameters of 51 mm and 50.8 mm, respectively. The Vespel® rod was cut into 5 disks with thicknesses from 0.25 mm to 1.80 mm, while 7 disks with thicknesses from 0.16 mm to 1.28 mm were obtained from the PEEK rod; the Kapton® was instead received as a set of square sheets with side length of 100 mm and thicknesses ranging from 0.0125 mm to 0.125 mm (Figure 19). Since the disks of PEEK and Vespel® had to be machined on a lathe, they were cleaned with water based anionic surfactant agent before the tests. The Kapton® sample sheets were instead tested as received from the provider. A summary of the final dimensions and shapes of the samples is provided in Table 3.

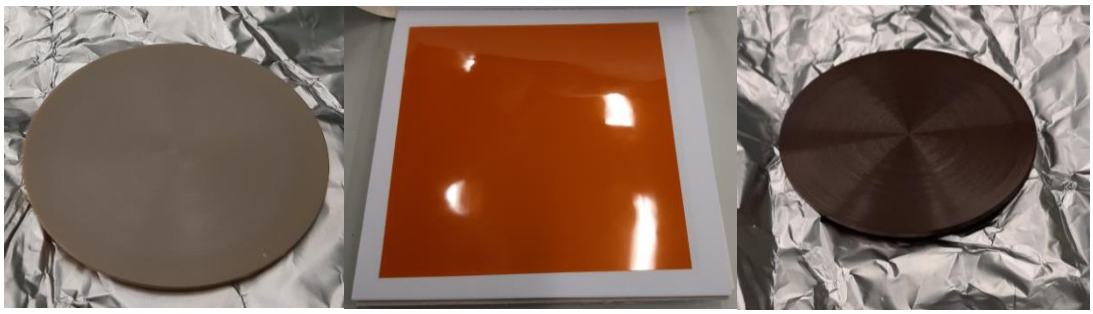

Figure 19: PEEK (left), Kapton® (centre), and Vespel® (right) samples

Table 3: Information on the polymer samples

Polymer	Manufacturer	Sample shape	Side / diameter (mm)	Surface of the two faces[16] (cm^2)	Thicknesses (mm)
PEEK 450G	Victrex™	Disk	51	40.9	0.16, 0.18, 0.47, 0.50, 0.72, 0.94, 1.28
Vespel® SP-1	DuPont™	Disk	50.8	40.5	0.25, 0.45, 0.92, 1.30, 1.80
Kapton® HN	DuPont™	Square sheet	100	200	0.0125, 0.025, 0.05, 0.075, 0.125

[16] The combined surface of the top and bottom faces. Since all the tested samples were very thin, the outgassing from the side walls was considered negligible, therefore only the surface of the two faces has been considered.

3.2 Equipment

The outgassing measurements were performed on a test bench whose schematic is shown in Figure 20. The main vacuum chamber (hereafter, sample dome) was a CF 4 ways cross DN 63/40 made of 304 alloy (stainless) steel, connected through a manually actuated angle valve to the pumping group. The latter was an Agilent TPS-mobile with integrated controller, featuring a TwisTorr 304 FS turbo molecular pump with a nominal pumping speed for N_2 of 250 L s^{-1}, backed by an Edwards RV12 rotary vane pump. A manually actuated valve was interposed between the two pumps, allowing to bypass the secondary pump when performing leak detection tests.

A Ø1 cm thin-walled orifice was installed between the sample dome and the inlet of the pumping group; its conductance was calculated as 9.2 L s^{-1} for N_2 and 11.5 L s^{-1} for H_2O using Equation 2.23.

The pressure on both sides of the restriction was monitored using Pirani TPR 017 DN 16 CF-F and Penning IKR 070 DN 40 CF-F gauges, both models produced by Pfeiffer. A Prisma QME 200 residual gas analyser using quadrupole technology (also produced by Pfeiffer) was mounted above the sample dome to conduct spectrometric analysis of the outgassing species. A digital controller Pfeiffer TPG 300 was employed to read the signals from the vacuum gauges and send the data to a desktop computer.

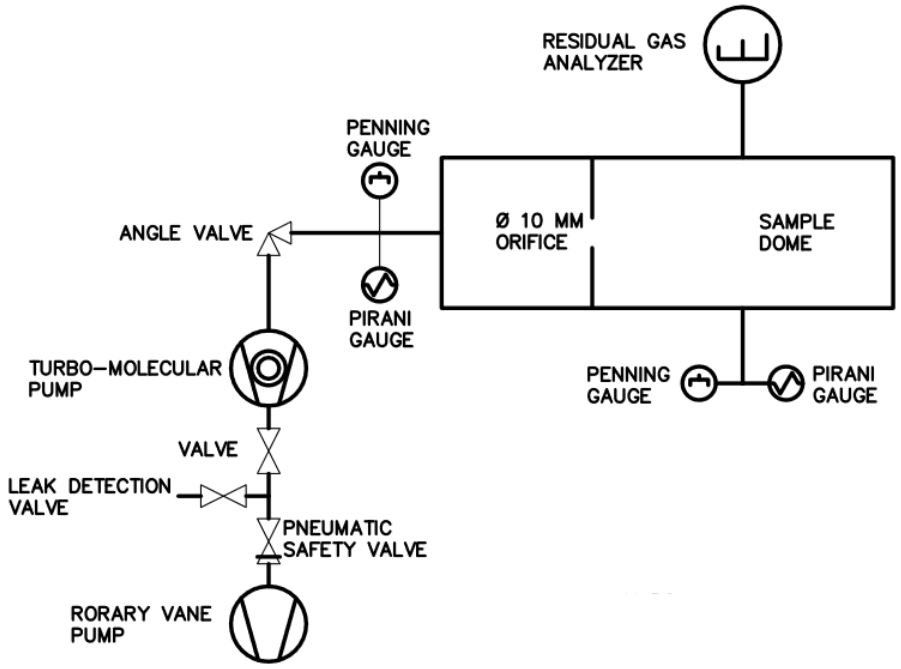

Figure 20. Schematic representation of the test bench used for the pump-down measurements.

3.3 Experimental Procedures

The configuration of the system allowed to calculate the outgassing rates inside the sample dome via the throughput method (Grinham & Chew, 2017): in the high vacuum regime and in absence of external leaks, the throughput Q from the sample dome was assumed to be entirely due to the outgassing from the internal surfaces of the vacuum chamber and the samples.

In virtue of Equation 2.18, the effective pumping speed at the outlet of the sample dome, S_{eff}, was approximated by the conductance of the orifice, since the latter was significantly smaller than the pumping speed of the pump. The value computed for water, 11.5 L s^{-1}, was chosen to calculate the throughputs, as H_2O molecules were expected to be the most abundant gaseous species in the sample dome (Schwarz, 1998, p. 514), fact that was eventually verified through spectrometric analysis. The gas flow from the sample dome was calculated using Equation 2.20, i.e. $Q = S_{eff}\, p_{chamber} \approx C\, p_{chamber}$, since the pressure near the inlet of the pump was always more than one order of magnitude lower than the pressure in the sample dome (often less than 5%).

To characterize the outgassing behaviour of the polymers under investigation, the net specific outgassing rates produced by each sample had to be computed. To do so, a pump-down of the empty system (a so-called background measurement) was initially performed to measure the total outgassing rates due to desorption from the walls of the sample dome; an equation to model these outgassing rates as a function of time, $Q_{bg}(t)$ was then extracted from the data. During the subsequent measurements with a sample inside the vacuum chamber, the specific outgassing rates of the sample q_{sample} were calculated as follows:

$$q_{sample} = \frac{Q_{measured} - Q_{bg}}{A_{sample}} \qquad 3.1$$

where $Q_{measured}$ was the total outgassing rate calculated upon the pressure reading at a certain pump-down time t, Q_{bg} was the corresponding outgassing rate value computed using the function $Q_{bg}(t)$ extracted from the background measurement, and A_{sample} was the combined surface of the top and bottom faces of the sample.

Before being tested, the samples were stored for at least 2 weeks in a clean environment protected from dust and other potential contaminants, exposed to normal levels of mois-

ture present in the air corresponding to a relative humidity (R.H.) oscillating between 30% and 65%. With the exception of the initial cleaning of the machined disks, no other operation was performed on the samples.

The pump-down procedure consisted in introducing a sample inside the sample dome, then sealing the latter with a flat flange and subsequently activating the pumping action by turning on the pumps and opening the various valves in a specific sequence.

A leak detection test was performed ca. 30 minutes after the beginning of each pump-down by connecting a special leak detection device to the system through a dedicated valve (see Figure 20) and then spraying He gas around all the sealed flanges in the test bench. In the presence of air leaks, the He gas penetrates into the low-pressure volume inside the vacuum system, being eventually detected by the leak detector, which would produce a warning signal. These types of tests were carried out to exclude the presence of undetected air leaks that would have caused an overestimate of the outgassing rates inside the sample dome during the pump-down measurements.

These were usually carried out at a temperature of about 22 °C (295 K), though variations of ca. ±3 °C have been observed, mainly due to the day-night cycles or abrupt changes in the external weather conditions. The overall pump-down time was not kept constant between different measurements, since the rate at which the pressure decreased inside the dome varied hugely from sample to sample. Each measurement during this phase was therefore interrupted when it was deemed that a sufficiently low pressure had been achieved, or that enough data had been collected, resulting in pump-down times that spanned from 24 hours for the thinnest samples, to over 600 hours for the thickest ones.

Before the end of each outgassing measurement, at least one mass spectrum of the residual gaseous molecules present in the sample dome was recorded with the RGA.

4 RESULTS

4.1 Pump-Down Curves and Specific Outgassing Rates

4.1.1 Background Measurement

The pump-down curve obtained during the preliminary background measurement is

shown in Figure 21. The graph presents two vertical axes, one for the pressure and the other for the outgassing rate; the values of the latter correspond to the values of the pressure axis multiplied by the pumping speed, such that the pressure and outgassing rate curves are made overlap. The horizontal axis displays the pumping time expressed in units of hours[17]. All axes show values in logarithmic scale. In such a graph, the pump-down curve of the empty system results in an almost perfect straight line, indication that the outgassing inside the vacuum chamber, up to the shown pressure level, was almost exclusively due to surface desorption processes, as explained in Section 2.2.1.

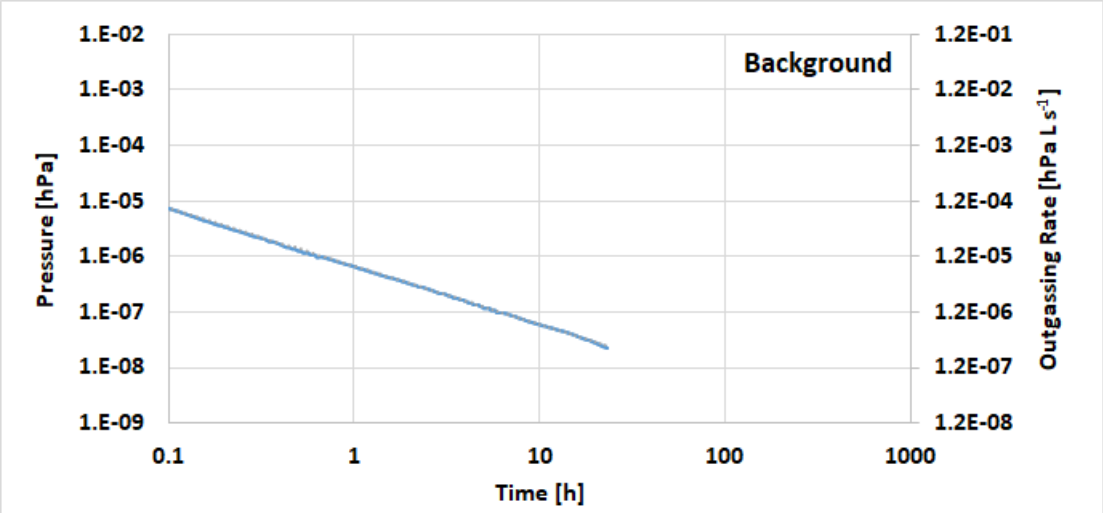

Figure 21. Pump-down curve recorded with the empty system.

From this pump-down curve, the following model for calculating the background outgassing rate as a function of pumping time, was obtained: $Q_{bg}(t) = 6.74 \cdot 10^{-7} t^{-1.04}$.

4.1.2 Pump-Down Curves Obtained with the Samples

The pump-down curves collected with the samples, divided by material type, are shown in Figure 22, Figure 23 and Figure 24 on log-log plots. The extrapolated[18] pump-down curve of the background (BG) is also plotted in every graph as a reference.

For each material, initial pressure and outgassing rates were very similar regardless of the specific thicknesses of the samples, as almost all the pump-down curves overlapped. The Kapton® sheets, which had a surface ca. 5 times larger than the other two materi-

[17] The hour (symbol h) is one of the non-SI units that are accepted for use with the SI (Bureau International des Poids et Mesures, 2019, p. 145).

[18] A sufficiently long empirical pump-down curve for the background was not available, therefore the model $Q_{bg}(t) = 6.74 \cdot 10^{-7} t^{-1.04}$ calculated after the initial background measurement was used instead.

als, produced the highest initial outgassing values, while Vespel® and PEEK, whose samples had similar surface, during the first few hours exhibited outgassing rates in the same range, although the rates of Vespel® were in general higher.

In all cases, the initial outgassing values decreased proportionally to $t^{-1/2}$, until a faster decay occurred, visible from a "bend" in the curves. These features were in line with the pump-down curves expected from diffusion-limited outgassing phenomena, as explained in Section 2.2.2.

From the figures it is also possible to notice that the faster, exponential-like decay of the outgassing rates began earlier with the thinnest samples and progressively later with the thickest ones, behaviour that was observed with all three materials.

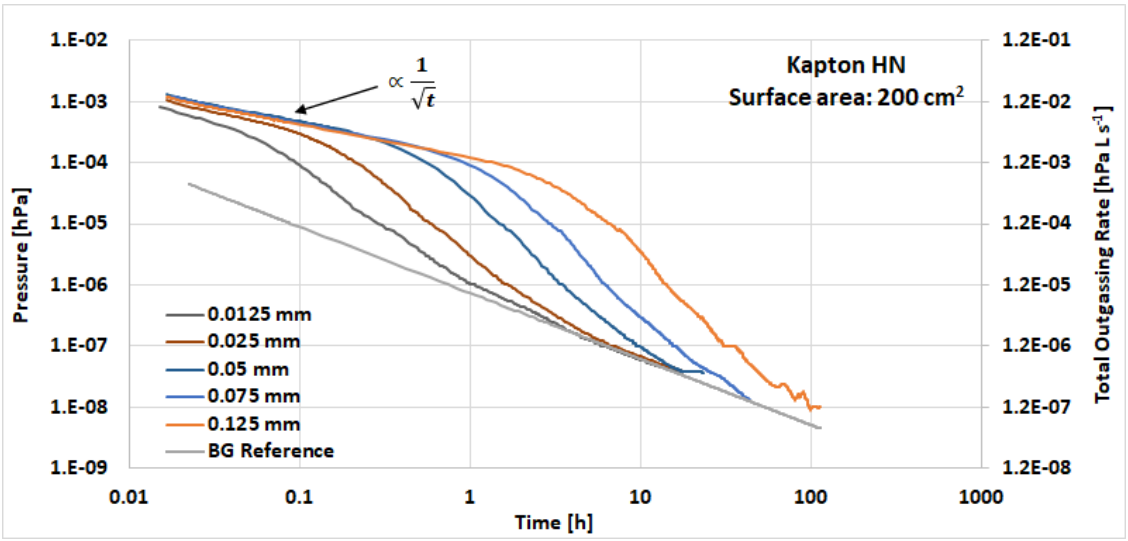

Figure 22. Pump-down curves obtained with the Kapton® samples.

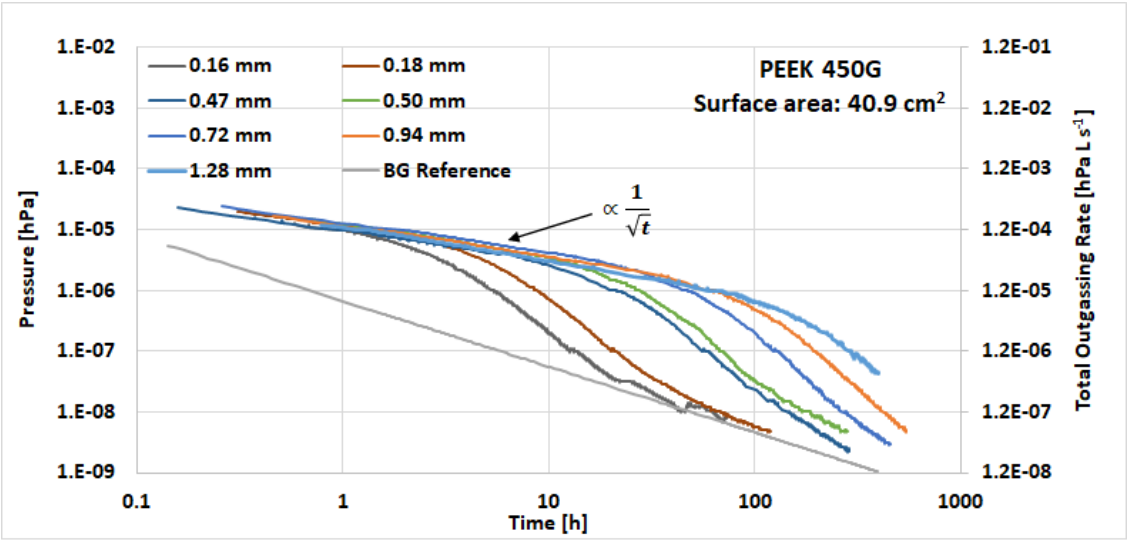

Figure 23. Pump-down curves obtained with the PEEK samples.

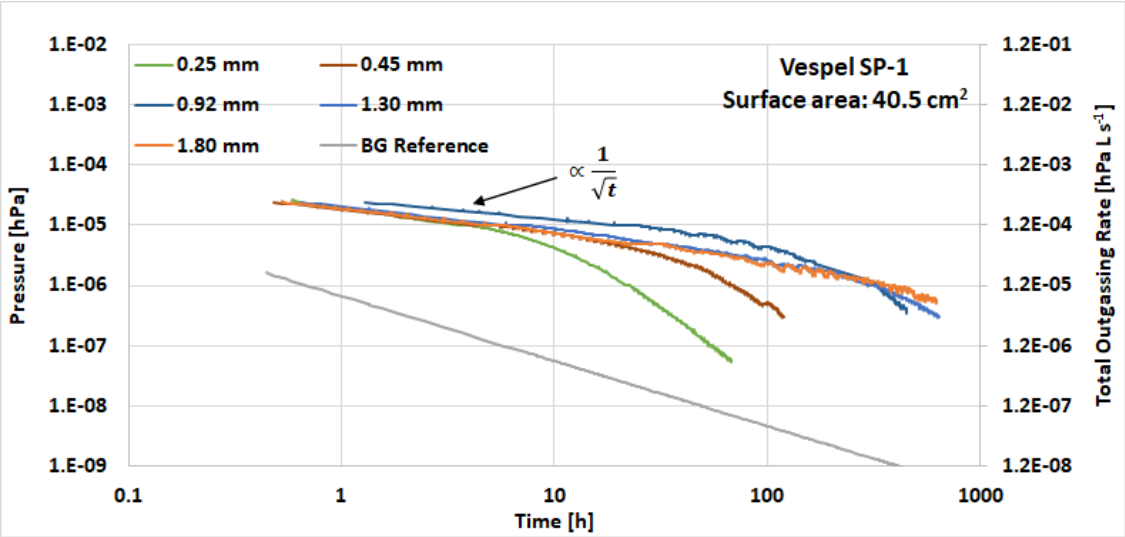

Figure 24. Pump-down curves obtained with the Vespel® samples.

Extending the measurements for enough time, the pump-down curves of the samples tended to approach asymptotically the one of the background, sign that their outgassing became eventually negligible compared to the outgassing produced by the system walls.

From the total outgassing rates of the samples and after removing the contribution of the background, the specific outgassing rates of the three materials were calculated, according to Equation 3.1. The results are plotted in Figure 25, Figure 26 and Figure 27.

Kapton®, whose samples were thinner than the other materials, showed very early exponential-like decays occurring in a matter of few minutes for the thinnest sheets, and after few hours for the thickest ones. The thicker PEEK and Vespel® samples exhibited the "bend" of the faster decay later, at pumping times sometimes above 100 hours.

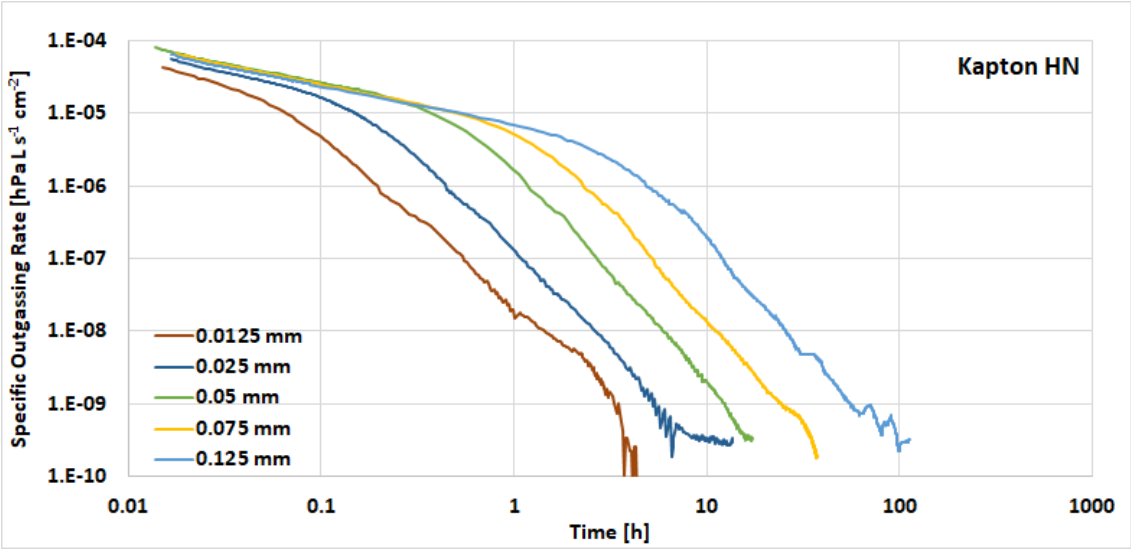

Figure 25. Specific outgassing rates of Kapton®.

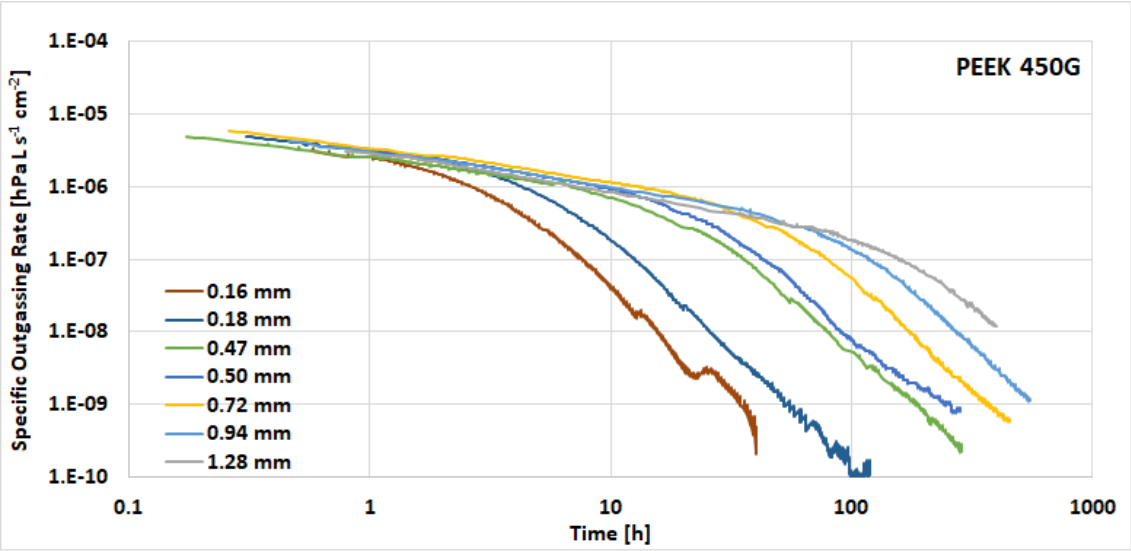

Figure 26. Specific outgassing rates of PEEK.

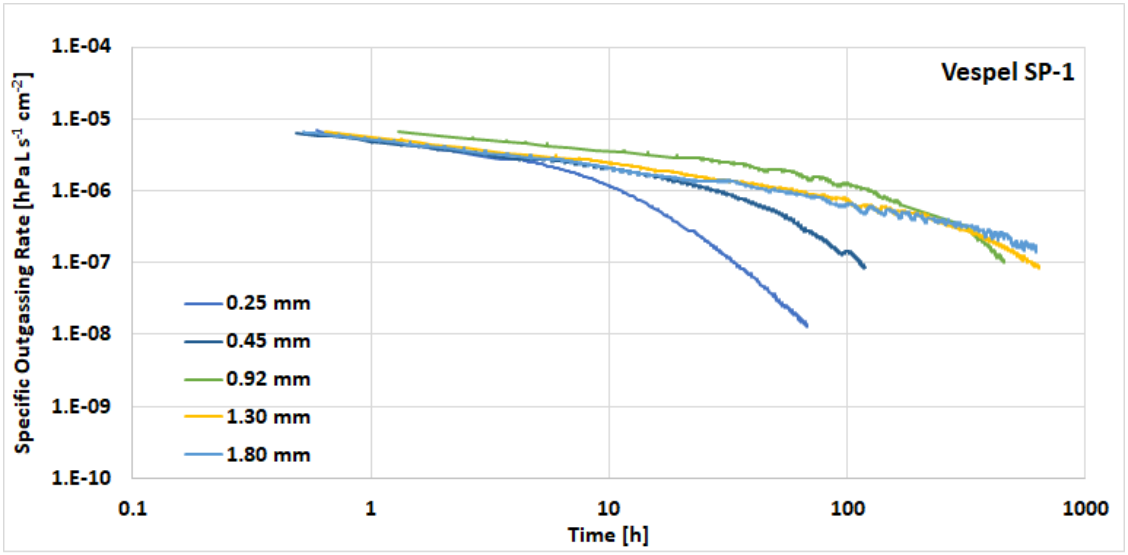

Figure 27. Specific outgassing rates of Vespel®.

From the log-log plots above, it can be also noticed that, when the curves extended significantly beyond the beginning of the exponential-like decay, they tended to assume again a straight line shape, hinting at a power rule rather than at an exponential one.

Since the tested samples of PEEK and Vespel® had very similar surface area, and having some of them also comparable thicknesses, it was possible to make a direct comparison between the outgassing rates of these two materials, as shown in Figure 28.

The graph shows that, given a certain thickness, PEEK exhibit lower initial outgassing rates and an earlier occurrence of the exponential decay, thus reaching much sooner low outgassing rate values than Vespel®.

As a general summary of these results, the specific outgassing rates of all the samples,

measured after 24 hours of pumping, are listed in the following Table 4.

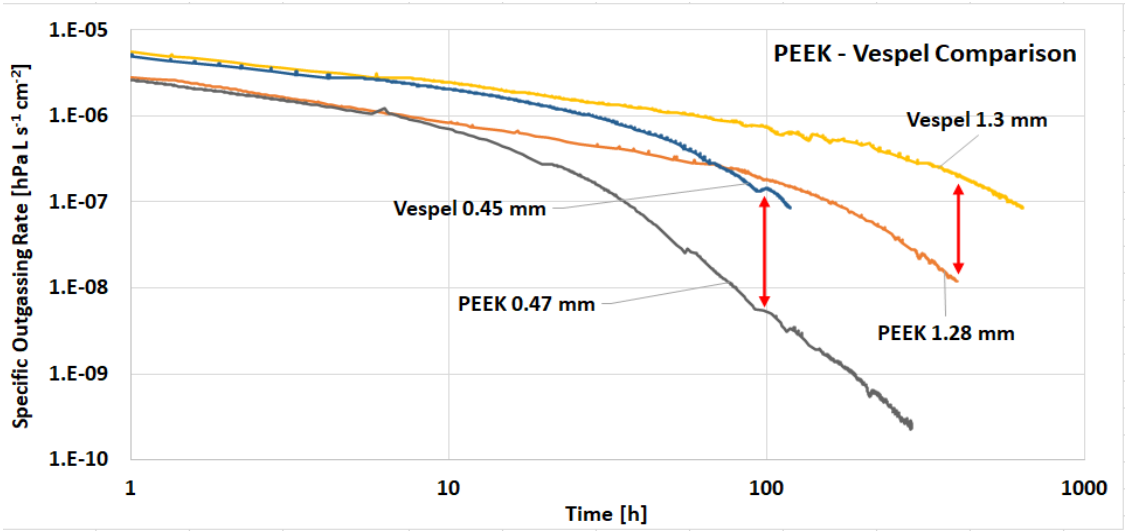

Figure 28. Outgassing rates of two pairs of similar sized Vespel® and PEEK samples.

Table 4: Specific outgassing rates of the tested polymers measured after 24 hours of pumping.

PEEK 450G		Vespel® SP-1		Kapton® HN	
Sample thickness [mm]	Specific outgassing rate [hPa L s^{-1} cm^{-2}]	Sample thickness [mm]	Specific outgassing rate [hPa L s^{-1} cm^{-2}]	Sample thickness [mm]	Specific outgassing rate [hPa L s^{-1} cm^{-2}]
0.16	$2.4\ 10^{-9}$	0.25	$3.1\ 10^{-7}$	0.0125	$<10^{-10}$
0.18	$1.4\ 10^{-8}$	0.45	$1.5\ 10^{-6}$	0.025	$<10^{-10}$
0.47	$2.4\ 10^{-7}$	0.92	$2.9\ 10^{-6}$	0.05	$6.9\ 10^{-10}$
0.5	$3.3\ 10^{-7}$	1.3	$1.6\ 10^{-6}$	0.075	$1.1\ 10^{-9}$
0.72	$6.4\ 10^{-7}$	1.8	$1.7\ 10^{-6}$	0.125	$1.3\ 10^{-8}$
0.94	$6.2\ 10^{-7}$				
1.28	$5.0\ 10^{-7}$				

4.2 Mass Spectra

4.2.1 Background Measurement

Figure 29 shows the results of the mass spectrometry performed at the end of the background measurement. The values in the plot are normalized to the value of the highest peak, which was found at the mass/charge value of 18, i.e. H_2O^+. The spectrum reveals that the outgassing from the chamber walls was dominated by water molecules, which constituted about 90% of all the residual species, since also the peak at 17, OH^+, can be attributed to the cracking of water molecules caused by the RGA (see Section 2.4.2).

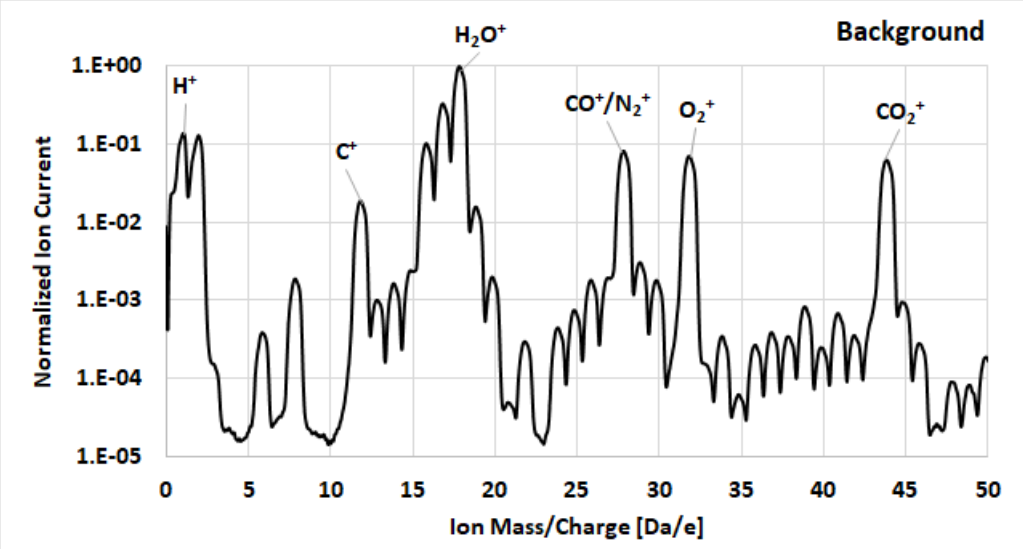

Figure 29: Normalized mass spectrum of the empty background, taken at a pressure of $3 \cdot 10^{-8}$ hPa.

4.2.2 Mass Spectra of the Samples

Figure 30, Figure 31 and Figure 32 show the spectra of a Kapton®, a PEEK and a Vespel® sample collected at the end of their pump-down measurements at similar pressures. In all three graphs, the highest peak is found at 18, with 17 being the second highest, hence H_2O was the most abundant species accounting for at least 75% of the total outgassing from the polymers.

The spectrum of the Kapton® sample shows very few differences with the spectrum of the background, the most relevant of which are the slightly higher peaks at 14 and 32, i.e. N^+ and O_2^+ and the peak at 30, the latter possibly indicating the presence of NO ions in the sample dome (Jenninger & Chiggiato, 2017, p. 26, 70).

The spectrum of the PEEK sample is very similar to the one of the Kapton®, featuring a slightly higher peak at 14 and a peak at mass 40, i.e. Ar^+, which has a relative intensity of about 1% compared to the peak at 28 (N_2^+), approaching the ratio that these two gases have in the atmosphere (1,2%). This fact, together with the slightly higher peaks caused by nitrogen and oxygen, indicate the presence of trapped air in this polymer.

The spectrum of the Vespel® sample shows even an higher Ar^+ peak, as well as the highest peaks at 28 (N_2^+, CO^+), 14 (N^+) and 7 (N^{++}), all clear signatures of high outgassing of air species, probably trapped inside the bulk of the material. This polymer also exhibited a peak at the value 64 (not shown in Figure 32), which might indicate the outgassing of sulphuric compounds such as S_2 and SO_2. The latter could be explained by the use of aprotic polar solvents such as dimethyl sulfoxide (DMSO) during the synthe-

sis of the polyimide (USA Patent No. US9617386B2, 2013).

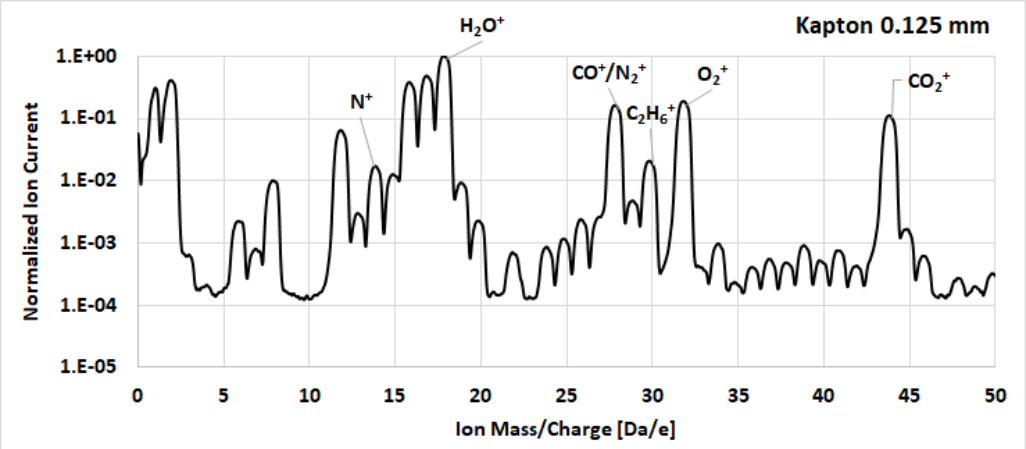

Figure 30. Normalized mass spectrum of Kapton, taken at a pressure of $2.5 \cdot 10^{-8}$ hPa.

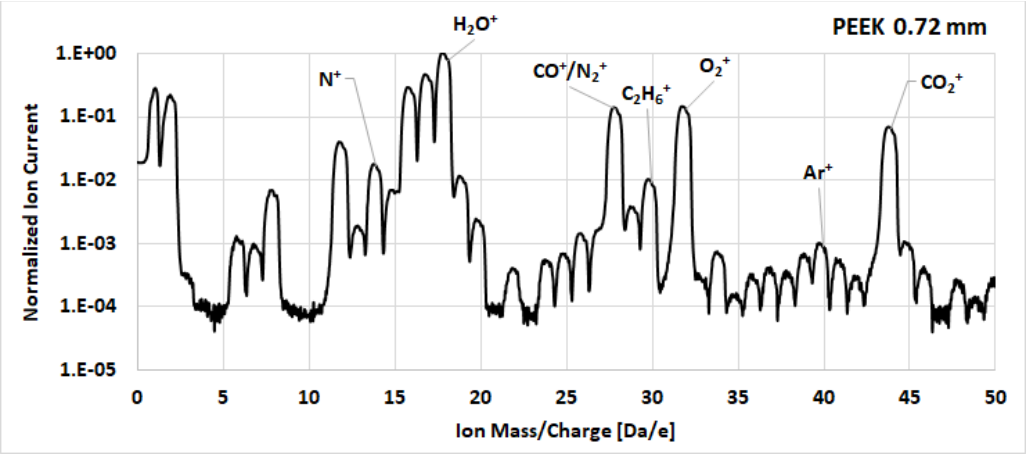

Figure 31. Normalized mass spectrum of PEEK, taken at a pressure of $2.4 \cdot 10^{-8}$ hPa.

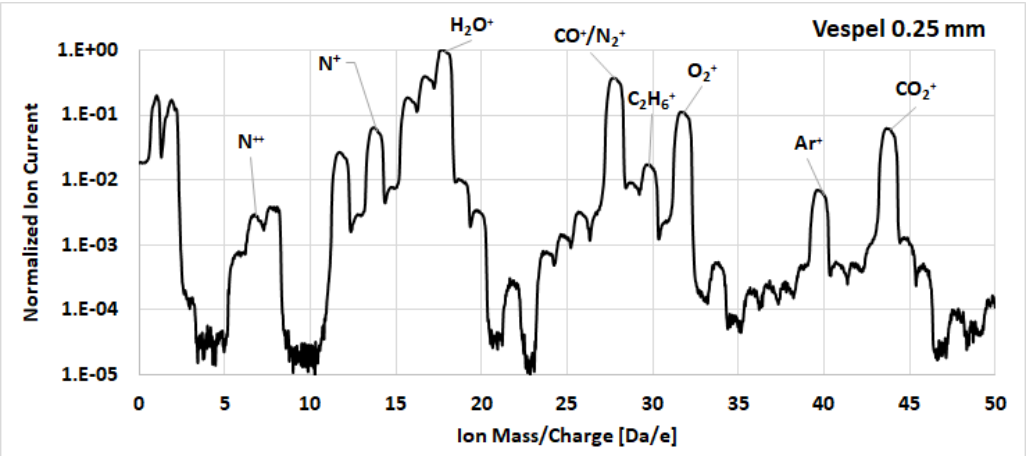

Figure 32. Normalized mass spectrum of Vespel, taken at a pressure of $4 \cdot 10^{-8}$ hPa.

The features underlined for each of these selected spectra were similarly found also in most of the other spectra. Thus, the Kapton® polymer in general exhibited very little outgassing of atmospheric species (besides water), the PEEK showed a slightly higher

outgassing of nitrogen and argon, and the Vespel® displayed the most significant release of atmospheric gases among the three polymers.

5 ANALYSIS OF THE RESULTS

As seen in Section 4.1.2, the outgassing rates of the polymeric samples recorded during the pump-down measurements showed typical features of diffusion process: the initial slope of the curves (in log-log plots) were consistent with the $q \propto t^{-1/2}$ rule expected when diffusion limited desorption is the dominant outgassing phenomenon, and an exponential-like behaviour, whose occurrence was clearly dependent on the thickness of the samples, was also observed. Spectrometric analysis suggests that the outgassing was mainly due to H2O molecules diffusing from the bulk. However, the plot of the specific outgassing rates showed that after long pump-down times the curves seemed to assume again a straight line shape, hinting at a divergence from the Fickian model.

The suitability of the latter for describing the outgassing rates of PEEK, Vespel® and Kapton® was therefore tested by trying to fit the empirical data with curves computed using the 2-step Equation 2.45. To do so, plausible values for the initial moisture content c_0 (see Section 3.1) and diffusion coefficients D were selected according to the available sources (Rabilloud, 2000, pp. 156-157; Chiggiato, 2017, p. 17; Chiggiato & Kershaw, 2010; NASA, 2018; de Rooij, n.d.), and used as initial guesses for the fitting procedure. A time constant τ based on thickness and diffusion coefficient was then calculated for every sample.

The values of c_0, which were available as mass percentages, were converted into grams per cm^3 by multiplying them by the density of the polymer ρ_{polim} in the following way:

$$c_0\left[\frac{g}{cm^3}\right] = \frac{c_0[wt.\%]}{100} \cdot \rho_{polim}\ \left[\frac{g}{cm^3}\right] \qquad 5.1$$

These values were then expressed in terms of molar concentration by exploiting the fact that 1 mol (H_2O) = 18 g (H_2O) and that 1 L = 10^3 cm^3:

$$c_0\left[\frac{mol}{L}\right] = c_0\left[\frac{g}{cm^3}\right] \cdot \frac{1}{18}\left[\frac{mol}{g}\right] \cdot 10^3\left[\frac{cm^3}{L}\right] \qquad 5.2$$

Finally, the molar concentration could be written as the partial pressure of the H_2O molecules dissolved inside the polymer by applying the ideal gas law as formulated in

Equation 2.4 (Section 2.1.2), which, at 22 °C = 295 K results in:

$$c_0[hPa] = p_{H_2O} = \frac{\nu}{V} \cdot RT = c_0 \left[\frac{mol}{L}\right] \cdot 83.14 \, \frac{hPa \, L}{mol \, K} \cdot 295 \, K \qquad 5.3$$

Thus, the moisture concentration inside the polymer samples could be expressed in hPa, for an easier and more direct calculation of the outgassing rates with Equation 2.45.

The fitting curves calculated using the 2-step equation model worked well for the data collected with most Vespel® samples, whose tests, however, were not extended for periods of time much longer than the τ calculated for each specific sample. This was later rectified by increasing pump-down times when testing most of the PEEK and Kapton® samples, in order to collect information on the outgassing behaviour of the polymers for values of $t > 3\tau$. A strong divergence was then observed above this threshold between the empirical data and the model, divergence that regularly occurred with all the samples, whenever the measurements were extended for long enough times. The 0.25 mm thick Vespel® sample was also retested for a longer time, revealing that the same divergence occurred with all three polymers, as shown in Figure 33.

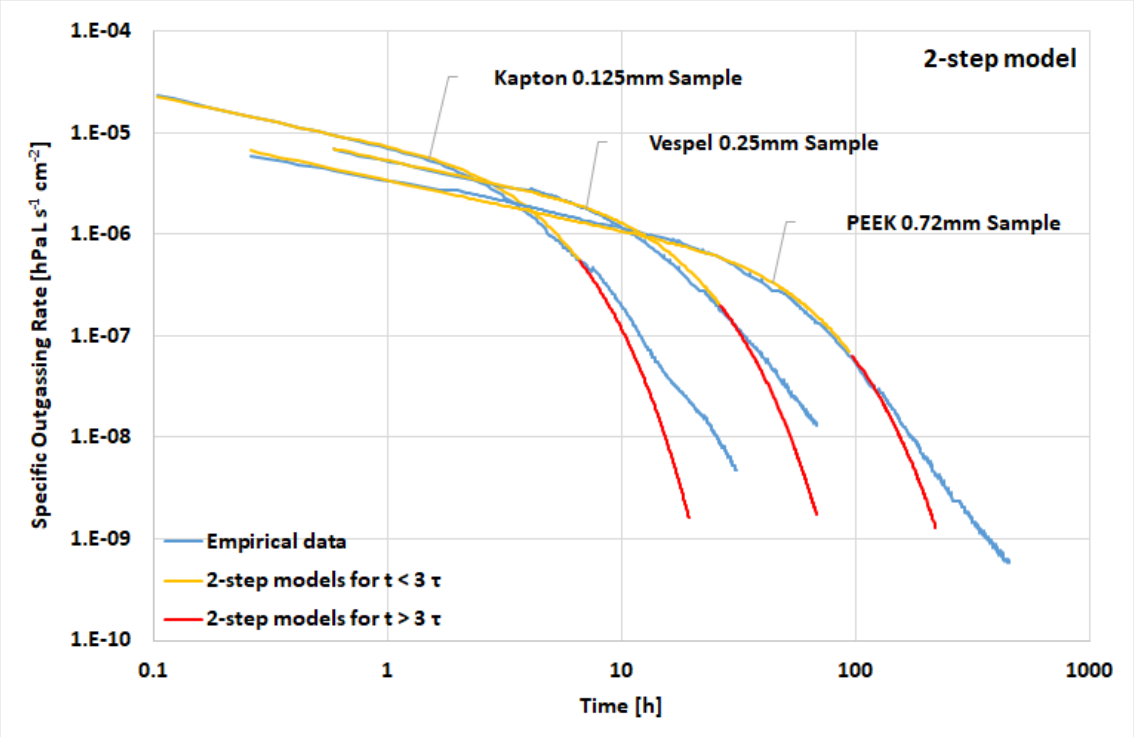

Figure 33: The divergence between the 2-step model and the empirical data for $t > 3\tau$

Regression analysis focused on the final part of the outgassing curves allowed to establish that the relationship $q \propto t^{-3}$ was found to fit very well the data for values of $t > 3\tau$.

After writing this relationship in terms of c_0 and τ and rearranging for convenience some terms in Equation 2.45, the following 3 equations were assembled and eventually adopted during the continuation of the study to model the specific outgassing rates of the polymeric samples:

$$q_{face}(t) = \begin{cases} j_0 c_0 \sqrt{\frac{\pi\tau}{t}} & for\ t \leq 0.5\tau \\ 4 j_0 c_0 e^{-\frac{t}{\tau}} & for\ 0.5\tau < t \leq 3\tau \\ \frac{1}{6} j_0 c_0 \left(\frac{\pi\tau}{t}\right)^3 & for\ t > 3\tau \end{cases} \quad , \quad \tau = \frac{l^2}{\pi^2 D} \qquad 5.4$$

where the parameter $j_0 = \frac{D}{l}$ has been here introduced for ease of calculation.

This 3-step equation eventually allowed to obtain very good fits for all the collected empirical curves, as it can be seen in Figure 34, showing the specific outgassing rates of the same three samples plotted in Figure 33, this time fitted with the new model.

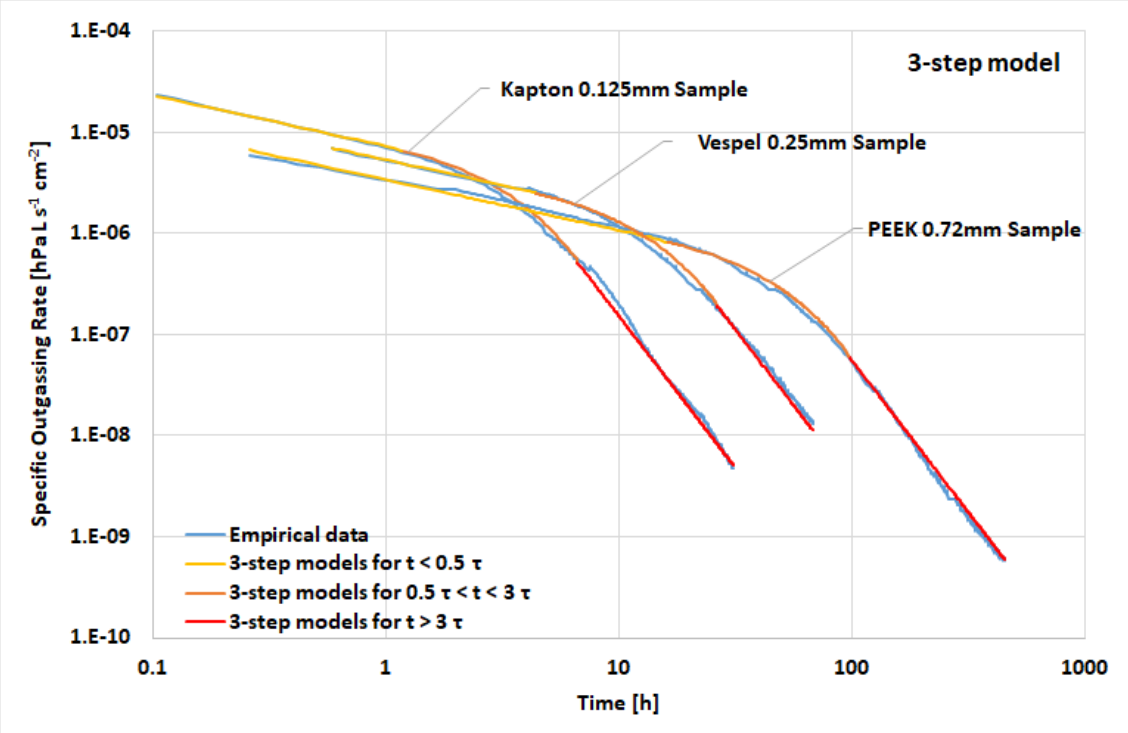

Figure 34: The 3-step model allowed to fit very well the empirical data also for $t > 3\tau$

By optimizing the τ and j_0 parameters during the fitting procedure, the actual diffusion coefficients D and the initial moisture contents c_0 of each sample were obtained, upon which average values were computed for each material. The results of these calculations, which are in good agreement with the data found in the available sources, are

listed in the Appendix B and graphically summarized in Figure 35.

PEEK on average exhibited a higher diffusion coefficient ($4.2 \cdot 10^{-9}$ cm^2 s^{-1}) and a lower moisture content (0.3%) than Vespel® and Kapton®. The average values obtained for the two polyimides were remarkably similar (diffusion coefficients of $1.7 - 1.8 \cdot 10^{-9}$ cm^2 s^{-1} and initial moisture content of 0.94 – 0.97%), which might be explained by their common chemical structure (see Section 3.1).

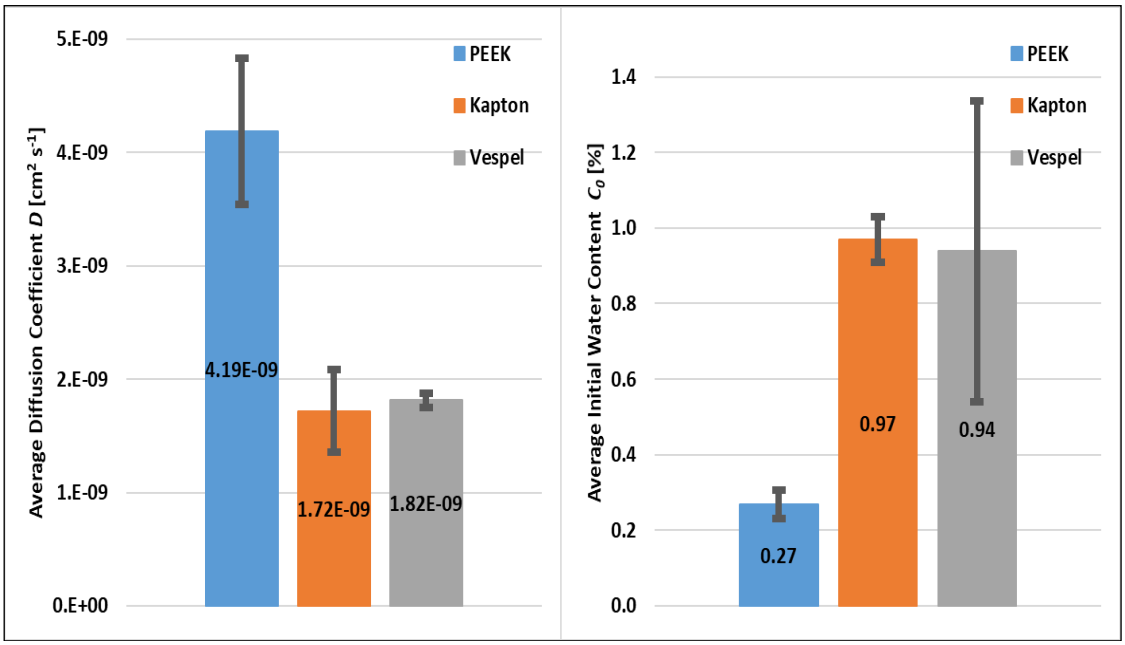

Figure 35: Average values of D and C_0 computed through the fitting procedure. The error bars represent the standard deviations of the data

The big standard deviations associated with some of the extrapolated values can largely be attributed to the small size of the sample population available for each material; moreover, non-perfectly constant conditions before and during the tests might have contributed to increase the variability of the collected data, since changes in the relative humidity of the air (see Section 3.3) can have influenced the amount of water vapour absorbed by the polymers, and even small variations in the environmental temperature (ibid.) could have had a sizable effect on the diffusion coefficients of the samples (Jousten, 2016a, p. 247). Despite the uncertainties in the data, the application of Equation 5.4 for fitting the empirical curves proved to be a viable way to estimate the specific outgassing rates of all three polymers.

The different time constants τ associated with each sample, upon which the initiation of the faster exponential decay depends, were also optimized during the fitting procedure,

and found to be with good approximation proportional to the square of the thickness, as shown in Figure 36. This has an important consequence: increasing the thickness by only a fraction of a millimetre can potentially extend the necessary pump-down times by tens, even hundreds of hours. Consequently, it might be concluded that the thickness is the most important factor affecting the outgassing behaviour of the tested polymers.

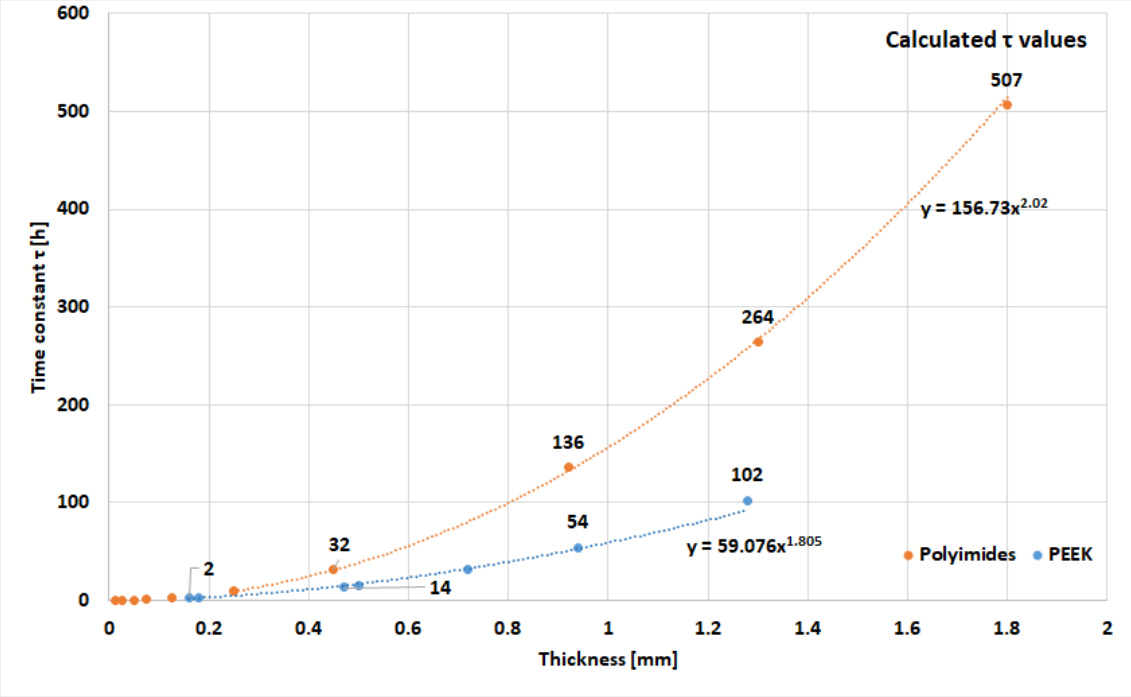

Figure 36: Variation of the time constant τ with the thickness of the tested materials. The Kapton® and Vespel® are plotted together as "Polyimides", having essentially the same diffusion coefficient.

6 DISCUSSION

The calculation of diffusion coefficients and initial moisture contents through the optimization of the parameters in the model allowed to draw some important conclusions about the general outgassing behaviour of these polymeric materials: a higher moisture content causes higher outgassing rates during all stages of the pump-down, while a greater diffusion coefficient, although increasing the initial outgassing rates, causes the latter to decay sooner, making possible to reduce pump-down times. Thus, the difference in these parameters can well explain the difference in specific outgassing rates observed between PEEK and Vespel® samples of equal thicknesses, which has been highlighted in Figure 28 of Section 4.1.2.

On the other hand, the differences in outgassing rates between Vespel® and Kapton®,

which share the same chemical formula and exhibited almost identical diffusion coefficients and moisture content, can mainly be attributed to their different thicknesses. The latter are determined by their respective synthesis/processing techniques: Kapton® is directly produced as a film with thicknesses in the range 0.0125 – 0.125 mm, while Vespel® is sintered in much thicker semi-finished shapes. The sintering route used during the manufacture of Vespel® parts might as well explain why this material, unlike the Kapton®, showed so evident signs of atmospheric species in its mass spectra: polymer sintering techniques usually lead to the production of highly porous materials (Ulbricht, 2011, p. 284) which can trap air inside their bulk both during production and probably also subsequently, provided adequately long exposure: the 0.25 mm thick Vespel® sample that was tested a second time after few months since the first test showed again the same peaks in its spectrum, indicating outgassing of N_2, CO and Ar from its bulk despite having already undergone pump-down once. The signature of atmospheric species found also in the spectra of PEEK samples, although to a less extent than in Vespel®, might also be due to a certain degree of porosity in this material, too.

It is important to remark how the outgassing of atmospheric species such as N_2 and Ar by PEEK and especially Vespel® polymers, shown by spectrometric analysis, could be cause of major concerns if detected inside the vacuum chambers of particle accelerators, since it might easily be mistaken for the presence of external air leaks. Engineers and technicians working on the vacuum systems of such machines therefore need to be aware of the problem, if parts containing any of these polymers had to be installed inside the vacuum equipment under their supervision.

Explanations to the deviation from the standard Fickian diffusion model observed for extended pump-down times might be sought within the framework of the dual-mode sorption theories that have been mentioned in Section 2.2.2. Since the outgassing of the polymers exhibited Fickian characteristics for a good part of the pump-down time, it seems unlikely that completely different diffusive mechanisms, such as those described by non-Fickian diffusion models (Crank, 1975, p. 256) could take place in the bulk of these materials when simply exposed to vacuum. Models accounting for concentration dependent diffusion coefficients do not seem to apply in this case either, since a good empirical fit was eventually found for all the curves without the need to modify this parameter into some sort of function. On the other hand, it is not unreasonable to assume that a fraction of the H_2O molecules absorbed by the polymers from the air could end up

filling some of the microvoids typically found between the molecular chains of all amorphous and semi-crystalline polymers (i.e. their *free volume*). These microscopic pockets of water could eventually diffuse again into the denser regions of the polymer if the concentration in the latter would drop under a certain threshold, situation that of course happens during the late stages of a pump-down. By leaving the voids, these once stored water molecules would effectively act as a secondary reservoir of moisture in the bulk, slowing down the rate of decay of the outgassing process at the surface, which would result in higher outgassing rate values than those predicted by the standard Fickian diffusion model when the polymer starts getting depleted of the majority of its moisture content, as observed during the outgassing measurements of PEEK, Kapton® and Vespel® presented in the previous sections of this document. The verification of such hypothesis, however, would require a rigorous mathematical analysis of the model and computer simulations which are beyond the scope of the present work, and will be left for future studies.

7 CONCLUSIONS

The outgassing behaviour of several samples of PEEK, Kapton® and Vespel® polymers have been investigated through a series of pump-down tests. The collected data suggest that the outgassing of these materials is mainly due to diffusion of H_2O molecules through the bulk, which then desorb from their surface into the volume of the vacuum chamber.

The measured outgassing rates of the polymers have been compared with the outgassing rates predicted by the Fickian diffusion model; agreement between empirical and modelled values was found only for relatively short pumping times, and a modification to the model based on empirical observations was introduced to more correctly describe the outgassing rates of these materials for extended pumping times. The discrepancy appears to be likely due to dual-mode sorption processes, though further investigation will be necessary to validate this hypothesis.

The analysis allowed to estimate average diffusion coefficients and initial moisture contents of the three polymers, and the obtained values were in agreement with the ones found in the available literature. The diffusion coefficients of Vespel® and Kapton® were in the range $1.7 - 1.8 \cdot 10^{-9}$ cm^2 s^{-1} and their initial moisture content was found

to be around 1%; a diffusion coefficient of ca. $4.2 \cdot 10^{-9}$ cm^2 s^{-1} and an initial moisture content of less than 0.3% were calculated for PEEK.

The higher moisture content in the polyimides causes higher outgassing rates at the beginning of the pump-down, compared to PEEK; the latter polymer also displays a quicker reduction of outgassing activity, owed to its higher diffusion coefficient that accelerates the depletion of outgassing species from the bulk, making possible to overall reduce pump-down times.

The relatively high standard deviations of the collected data suggest that the outgassing behaviour of PEEK, Kapton® and Vespel® could be, to some extent, influenced by environmental conditions, especially the amount of relative humidity in the air. It is therefore recommended to store components for HV and UHV systems containing these polymers in dry locations/containers several days before installation.

Alongside diffusion coefficient and initial moisture content, thickness was found to have a major impact on the decay of the specific outgassing rates of PEEK, Kapton® and Vespel®, and therefore it should represent the primary concern when selecting polymeric components to be installed into HV or UHV systems. Preference should always be given to the thinnest components available; if choosing between different polymers is possible, those with higher diffusion coefficients and lower expected moisture content should be then selected.

REFERENCES

Afework, B., Hanania, J., Stenhouse, K., & Donev, J. (2018, June 25). *Isothermal*. Retrieved 04 27, 2020, from Energy Education: https://energyeducation.ca/encyclopedia/Isothermal

Aguilar-Vega, M. (2013). Structure and Mechanical Properties of Polymers. In E. Saldıvar-Guerra, & E. Vivaldo-Lima (Eds.), *Handbook of polymer synthesis, characterization, and processing* (pp. 425-434). Hoboken, New Jersey, USA: John Wiley & Sons, Inc.

Baglin, V. (2019). Vacuum Systems Lecture 1. Archamps: CERN. Retrieved 04 26, 2020, from https://indico.cern.ch/event/779575/contributions/3244628/attachments/1793476

/2925134/Lecture_1_Vacuum_Systems_-_V_Baglin_-_JUAS_2019_-_12_feb_2019_with_complementary_info.pdf

Battes, K., Day, C., & Hauer, V. (2018). Outgassing behavior of different high-temperature resistant polymers. *Journal of Vacuum Science and Technology A, 36*(2).

Bregliozzi, G. (2017). *Vacuum Acceptance Tests for Particle Accelerator Equipment.* Retrieved 02 28, 2020, from https://indico.cern.ch/event/565314/contributions/2285863/attachments/1474356/2294232/No_Video.pdf

Bureau International des Poids et Mesures. (2019). *The International System of Units (SI).* Retrieved 03 14, 2020, from https://www.bipm.org/utils/common/pdf/si-brochure/SI-Brochure-9-EN.pdf

CERN. (2019). *Technology Department - Vacuum, Surfaces and Coatings*. Retrieved 03 22, 2020, from http://te-dep.web.cern.ch/content/vacuum-surfaces-and-coatings

CERN. (2020a). *CERN's accelerator complex*. Retrieved 02 17, 2020, from home.cern: https://home.cern/science/accelerators/accelerator-complex

CERN. (2020b). *A vacuum as empty as interstellar space*. Retrieved 02 17, 2020, from home.cern: https://home.cern/science/engineering/vacuum-empty-interstellar-space

CERN. (2020c). *Our History*. Retrieved 03 27, 2020, from home.cern: https://home.cern/about/who-we-are/our-history

CERN. (2020d). *Our Mission*. Retrieved 03 22, 2020, from https://home.cern/about/who-we-are/our-mission

CERN. (2020e). *The CERN accelerator complex - 2019*. Retrieved 03 22, 2020, from https://cds.cern.ch/record/2684277

CERN. (2020f). *Our Research*. Retrieved 03 22, 2020, from https://home.cern/about/what-we-do/our-research

CERN. (2020g). *The Standard Model*. Retrieved 03 22, 2020, from https://home.cern/science/physics/standard-model

CERN. (n.d.). *Thin Film Coatings For Improved Vacuum Performance.* Retrieved from

CERN - Accelerating Science: https://kt.cern/sites/knowledgetransfer.web.cern.ch/files/documents/technologies/neg-thin-film-coatingspdf.pdf

Chambers, A. (2005). *Modern Vacuum Physics.* Boca Raton, Florida , USA: CRC Press LLC .

Chiggiato, P. (2016). Vacuum technology for particle accelerators. *JUAS - Joint Universities Accelerators School* (p. 72). CERN. Retrieved 03 11, 2020, from https://indico.cern.ch/event/471931/contributions/1149644/attachments/1226014/1794769/JUAS-Notes_Vacuum_Tech-Chiggiato.pdf

Chiggiato, P. (2017). Materials and Properties IV - Outgassing. *CERN Accelerator School (CAS) on Vacuum for Particle Accelerators.* CERN. Retrieved 02 22, 2020, from https://indico.cern.ch/event/565314/contributions/2285743/attachments/1466415/2277367/Outgassing-CAS-Lund-final.pdf

Chiggiato, P. (2018). CERN's prowess in nothingness. (M. Chalmers, Ed.) *CERN Courier - International Journal of High-Energy Physics, 58*(5), pp. 26-30. Retrieved 04 02, 2020, from http://cds.cern.ch/record/2320186/files/CERN%20Courier%20June%202018%20(Volume%2053%20Issue%205).pdf

Chiggiato, P., & Kershaw, R. (2010). *Outgassing measurement of PEEK disks.* Retrieved 03 11, 2020, from https://edms.cern.ch/ui/file/1102539/1/Report_Agilent-Varian_PEEK_disks_docx_cpdf.pdf

Clapeyron, E. (1834). *Memoir on the Motive Power of Heat.* École Royale Polytechnique. Paris: École Royale Polytechnique. Retrieved 04 12, 2020, from https://gallica.bnf.fr/ark:/12148/bpt6k4336791/f157.image

Costa Pinto, P. (2013). History and Potential of Non Evaporable Getter (NEG) Technolog. *Workshop on Advanced Materials and Surfaces.* CERN. Retrieved 04 11, 2020, from https://indico.cern.ch/event/229108/contributions/1539894/attachments/379090/527262/Presentation_COSTA_PINTO.pdf

Crank, J. (1975). *The Mathematics of Diffusion* (Second ed.). Oxford: Oxford University Press. Retrieved 02 25, 2020, from http://www-eng.lbl.gov/~shuman/NEXT/MATERIALS%26COMPONENTS/Xe_damage/Crank-The-Mathematics-of-Diffusion.pdf

de Rooij, A. (n.d.). *SPACEMATDB - Space Materials DataBase*. Retrieved 02 17, 2020, from https://www.spacematdb.com/spacemat/

Duda, J., & Zielinski, J. (1996). Free-Volume Theory. In P. Neogi (Ed.), *Diffusion in polymers* (pp. 143-172). New York, USA: Marcel Dekker, Inc.

Elsen, E., & Bordry, F. (2018). *A successful conclusion to Run 2*. (CERN) Retrieved 03 19, 2020, from CERN - Accelerating Science: https://home.cern/news/opinion/accelerators/successful-conclusion-run-2

Fakirov, S. (2017). *Fundamentals of Polymer Science for Engineers.* Weinheim, Germany: Wiley-VCHVerlagGmbH&Co.KGaA.

Gianotti, F. (2018). The European Strategy and the future of HEP. *HL-LHC Collaboration meeting.* Geneva: CERN. Retrieved 04 22, 2020, from https://indico.cern.ch/event/742082/contributions/3072114/attachments/1734070/2803878/HL-LHC-FG.pdf#search=fcc

Gould, R., Kasap, S., & Ray, A. (2017). Thin Films. In R. Gould, S. Kasap, & A. Ray (Eds.), *Springer Handbook of Electronic and Photonic Materials* (Second ed.). Cham, Switzerland: Springer . Retrieved 05 18, 2020, from https://link.springer.com/book/10.1007/978-3-319-48933-9

Grasmeder, J. (2019, 09 24). *A Closer Peek at PEEK – HPP Explained (Part2)*. (Victrex plc) Retrieved 02 13, 2020, from victrex.com: https://www.victrex.com/en/blog/2017/a-closer-peek-at-peek

Grayson, M. (1987). The solubility and diffusion of water in poly(aryl-ether-ether-ketone) (PEEK). *Journal of Polymer Science, 25*(1).

Greenwood, J. (2002). The correct and incorrect generation of a cosine distribution ofscattered particles for Monte-Carlo modelling of vacuumsystems. *Vacuum, 67*, 217-222. Retrieved 05 02, 2020, from https://molflow.web.cern.ch/sites/molflow.web.cern.ch/files/1-s2.0-S0042207X02001732-main.pdf

Grinham, R., & Chew, A. (2017). A Review of Outgassing and Methods for its Reduction. *Applied Science and Convergence Technology, 26*(5), 95-109. Retrieved 03 12, 2020, from http://www.e-asct.org/journal/view.html?doi=10.5757/ASCT.2017.26.5.95

Guo, J., & Barbari, T. (2009). Unified Dual Mode Description of Small Molecule Sorption and Desorption Kinetics in a Glassy Polymer. *Macromolecules*(42), 5700-5708. Retrieved 02 28, 2020, from https://guolab.engr.ucr.edu/sites/g/files/rcwecm1696/files/2018-08/5._unified_dual_mode.pdf

Hablanian, M. (1998). Technology of Vacuum Pumps — An Overview. In D. Hoffman, B. Singh, & J. Thomas (Eds.), *Handbook of Vacuum Science and Technology* (pp. 57-254). San Diego, CA, USA: Academic Press .

Hait, P. (1967). The application of polyimide to ultrahigh vacuum seals. *Vacuum, 17*(10), pp. 547-550. Retrieved 03 11, 2020

Halliday, D., Resnick, R., & Walker, J. (2008). *Fundamentals of physics, extended edition.* Wiley.

Han, H., Seo, J., Ree, M., Pyo, S., & Gryte, C. (1998). Water sorption and diffusion behaviours in thin films of photosensitive polyimides. *Polymer, 39*(13), 2963-2972.

Henning, H. (1998). Turbomolecular Pumps. In D. Hoffman, B. Singh, & J. Thomas (Eds.), *Handbook of Vacuum Science and Technology* (pp. 183-213). San Diego, CA, USA: Academic Press.

Hrabovsky, J., Liberatore, C., Mirza, I., Sladek, J., Beranek, J., Bulgakov, A. V., & Bulgakova, N. M. (2019). Surface Structuring of Kapton Polyimide with Femtosecond and Picosecodn IR Laser Pulses. *Interfacial Phenomena and Heat Transfer, 7*(2), 113–121 . Retrieved 04 18, 2020, from https://www.researchgate.net/publication/335783913_Surface_structuring_of_Kapton_polyimide_with_femtosecond_and_picosecond_IR_laser_pulses

Hudson, J. (1998). Gas-Surface Interactions and Diffusion. In J. M. Lafferty (Ed.), *Foundations of Vacuum Science and Technology* (pp. 547-622). US: John Wiley & Sons, Inc.

Jenninger, B., & Chiggiato, P. (2017). CAS tutorial on RGA Interpretation of RGA spectra. *CAS - CERN Accelerators School.* CERN. Retrieved 04 02, 2020, from https://indico.cern.ch/event/565314/contributions/2285748/attachments/1467497/2273709/RGA_tutorial-interpretation.pdf#search=RGA%20tutorial

Jimenez, J. (2008). LHC: The World's Largest Vacuum Systems Being Commissioned at CERN. *EPAC - European Particle Accelerator Conference.* Genoa: CERN. Retrieved 04 29, 2020, from https://accelconf.web.cern.ch/e08/papers/weobm04.pdf

Jitschin, W. (2016a). Gas Flow. In K. Jousten (Ed.), *Handbook of Vacuum Technology* (Second ed., pp. 83-166). Weinheim, Germany: Wiley-VCH Verlag GmbH & Co. KGaA.

Jitschin, W. (2016b). Gas Laws and Kinetic Theory of Gases. In K. Jousten (Ed.), *Handbook of Vacuum Technology* (Second ed., pp. 29-82). Weinheim, Germany: Wiley-VCH Verlag GmbH & Co. KGaA.

Jousten, K. (2016a). Sorption and Diffusion. In K. Jousten (Ed.), *Handbook of Vacuum Technology* (Second ed., pp. 229-257). iley-VCH Verlag GmbH & Co. KGaA.

Jousten, K. (2016b). Sorption Pumps. In K. Jousten (Ed.), *Handbook of Vacuum Technology* (pp. 463-510). Weinheim, Germany: Wiley-VCH Verlag GmbH & Co. KGaA.

Jousten, K. (2016c). Total Pressure Vacuum Gauges. In K. Jousten (Ed.), *Handbook of Vacuum Technology* (Second ed., pp. 565-642). Weinheim, Germany: Wiley-VCH Verlag GmbH & Co. KGaA.

Jousten, K., Dirscherl, J., Lachenmann, R., Jünemann, A., Friedrichsen, Lippelt, E., & Kossek, B. (2016). Positive Displacement Pumps. In K. Jousten (Ed.), *Handbook of Vacuum Technology* (Second ed., pp. 259-360). Weinheim, Baden-Württemberg, Germany: Wiley-VCH Verlag GmbH & Co. KGaA.

Jousten, K., Ellefson, R., & Grosse Bley, W. (2016). Partial Pressure Vacuum Gauges and Leak Detectors. In K. Jousten (Ed.), *Handbook of Vacuum Technology* (pp. 643-696). Weinheim, Germany: Wiley-VCH Verlag GmbH & Co. KGaA.

Kemmish, D. (1995). *High Performance Engineering Plastics.* Shawbury: Rapra Technology LTD.

Kurt J. Lesker Company®. (n.d.). *Frequently Asked Questions*. Retrieved 03 19, 2020, from Kurt J. Lesker Company: https://www.lesker.com/newweb/faqs/question.cfm?id=477

Lee, G. (1989). *Materials for Ultra-High Vacuum.* Retrieved from Fermilab: https://lss.fnal.gov/archive/tm/TM-1615.pdf

LIGO. (2011). *LIGO Vacuum Compatible Materials List.* Retrieved from LIGO - Laser Interferometer Gravitational Wave Observatory: https://dcc-llo.ligo.org/public/0003/E960050/011/E960050-v11%20Vacuum%20Compatible%20Materials%20List.pdf

Livesey, R. (1998). Flow of Gases through Tubes and Orifices. In J. Lafferty (Ed.), *Foundations of Vacuum Science and Technology* (pp. 81-140). USA: John Wiley & Sons, Inc.

McKeen, L. (2008). *The effect of temperature and other factors on plastics and elastomers* (Second ed.). Norwich, NY, USA: William Andrew Inc. .

Mosher, M. (2016, November 28). Teaching IUPAC recommendations. *c&n - Chemical & Engineering News, 94*(47), p. 35. Retrieved 03 22, 2020, from https://cen.acs.org/content/cen/articles/94/i47/Teaching-IUPAC-recommendations.html

Najeeb, S., Khurshid, Z., Matinlinna, J., Siddiqui, F., Nassani, M., & Baroudi, K. (2015). Nanomodified Peek Dental Implants: Bioactive Compositesand Surface Modification — A Review. *International Journal of Dentistry*. Retrieved 05 02, 2020, from https://www.researchgate.net/publication/279842270_Nanomodified_Peek_Dental_Implants_Bioactive_Composites_and_Surface_Modification-A_Review

NASA. (2018). *Outgassing Data for Selecting Spacecraft Materials Online*. Retrieved 02 28, 2019, from https://outgassing.nasa.gov/

Outlaw, R. (1998). Practical Aspects of Vacuum System Mass Spectrometers. In D. Hoffman, B. Singh, & J. Thomas (Eds.), *Handbook of Vacuum Science and Technology* (pp. 335-375). San Diego, , CA, USA: Academic Press.

Painter, P., & Coleman, M. (1997). *Fundamentals of Polymer Science.* Boca Raton: CRC Press LLC.

Perabo, C. (2018). *How is Polyimide Pressure Sensitive Tape Made?* (CAPLINQ Corporation) Retrieved 03 02, 2020, from https://www.caplinq.com/blog/how-is-polyimide-film-made_7/

Rabilloud, G. (2000). *High-Performance Polymers* (Vol. 3). Paris, France: Editions Technip.

Ramos-de Valle, L. (2013). Principles of Polymer Processing. In E. Saldivar-Guerra, & E. Vivaldo-Lima (Eds.), *Handbook of Polymer Synthesis, Characterization and Processing* (pp. 451-461). Hoboken: John Wiley & Sons, Inc.

Reinerth, W., Malik, S., & De Binod, B. (2013). *USA Patent No. US9617386B2.* Retrieved 03 11, 2020, from https://patents.google.com/patent/US9617386

Riihimäki, A. (2019). *Outgassing Studies of Some Accelerator Materials.* Retrieved 03 11, 2020, from http://cds.cern.ch/record/2679153?ln=en

Saldıvar-Guerra, E., & Vivaldo-Lima, E. (2013). Introduction to Polymers and Polymers Types. In E. Saldıvar-Guerra, & E. Vivaldo-Lima (Eds.), *Handbook of Polymer Synthesis, Characterization and Processing* (pp. 3-14). Hoboken, New Jersey, USA: John Wiley & Sons, Inc.

Savary, F., Bajko, M., Bordini, B., Bottura, L., Devred, A., Fiscarelli, L., . . . Willering, G. (2019). Status of the 11 T Dipole and CERN Magnet Program Beyond HiLumi. CERN. Retrieved 04 29, 2020, from https://indico.cern.ch/event/806637/contributions/3487461/attachments/1925924/3187901/191014_Arnaud_11_T_and_beyond_HL-LHC_Meeting.pdf#search=FCC%20collimators%20polymers%20cables

Schwarz, W. (1998). High-Vacuum System Design. In J. Lafferty (Ed.), *Foundations of Vacuum Science and Technology* (pp. 513-516). John Wiley & Sons, Inc.

Singh, B., & Thomas, J. (1998). Fundamentals of Vacuum Technology and Surface Physics. In D. Hoffman, B. Singh, & J. Thomas (Eds.), *Handbook of Vacuum Science and Technology* (pp. 1-55). San Diego, California, USA: Academic Press.

Singleton, J. (1998). Pumps for Utra-High Vacuum Applications. In D. Hoffman, B. Sigh, & J. Thomas (Eds.), *Handbook of Vacuum Science and Technology* (pp. 214-254). San Diego, CA, USA: Academic Press.

Spurgeon, W. (2018). *Thermal Conductivities of Some Polymers and Composites.* US Army Research Laboratory. Adelphi: US Army Research Laboratory. Retrieved 04 20, 2020, from https://pdfs.semanticscholar.org/35b9/0a64cbfb188a72af5dd859c24902f1c44b5d.pdf?_ga=2.136354997.403697148.1588945036-759902428.1585936060

Tant, M., & Hill, A. (1999). The Structure and Properties of Glassy Polymers - An Overview. In M. Tant, & A. Hill (Eds.), *Structure and Properties of Glassy Polymers* (pp. 1-20). Washington, DC, USA: American Chemical Society. Retrieved 03 21, 2020, from https://pubs.acs.org/isbn/9780841235885

Teraoka, I. (2002). *Polymer Solutions - An Introduction to Physical Properties.* New York, USA: John Wiley & Sons, Inc.

Tsukiji, M., Bitoh, W., & Enomoto, J. (1990). *Thermal degradation and endurance of polyimide films.* doi:10.1109/ELINSL.1990.109715

Ulbricht, M. (2011). Separation Membranes. In M. Silverstein, N. Cameron, & M. Hillmyer (Eds.), *Porous Polymers.* Hoboken, New Jersey, USA: John Wiley & Sons, Inc.

University of Cambridge. (nd). *Crystallinity*. Retrieved 05 03, 2020, from Dissemination of IT for the Promotion of Materials Science (DoITPoMS): https://www.doitpoms.ac.uk/tlplib/polymerbasics/crystallinity.php

Appendix A:

Materials Technical Data Sheets

victrex®
HIGH PERFORMANCE POLYMERS

VICTREX® PEEK 450G

Product Description:
High performance thermoplastic material, unreinforced **P**oly**E**ther**E**ther**K**etone (PEEK), semi crystalline, granules for injection moulding and extrusion, standard flow, FDA food contact compliant, colour natural/beige.

Typical Application Areas:
Applications for higher strength and stiffness as well as high ductility. Chemically resistant to aggressive environments, suitable for sterilisation for medical and food contact applications.

Material Properties

	CONDITIONS	TEST METHOD	UNITS	TYPICAL VALUE
Mechanical Data				
Tensile Strength	Yield, 23°C	ISO 527	MPa	100
Tensile Elongation	Break, 23°C	ISO 527	%	45
Tensile Modulus	23°C	ISO 527	GPa	3.7
Flexural Strength	At 3.5% strain, 23°C	ISO 178	MPa	125
	At yield, 23°C			165
	125°C			85
	175°C			18
	275°C			13
Flexural Modulus	23°C	ISO 178	GPa	4.1
Compressive Strength	23°C	ISO 604	MPa	125
	120°C			70
Charpy Impact Strength	Notched, 23°C	ISO 179/1eA	kJ m^{-2}	7.0
	Unnotched, 23°C	ISO 179/U		n/b
Izod Impact Strength	Notched, 23°C	ISO 180/A	kJ m^{-2}	7.5
	Unnotched, 23°C	ISO 180/U		n/b
Thermal Data				
Melting Point		ISO 11357	°C	343
Glass Transition (Tg)	Onset	ISO 11357	°C	143
Specific Heat Capacity	23°C	DSC	kJ kg^{-1} $°C^{-1}$	2.2
Coefficient of Thermal Expansion	Along flow below Tg	ISO 11359	ppm K^{-1}	45
	Average below Tg			55
	Along flow above Tg			120
	Average above Tg			140
Heat Deflection Temperature	1.8 MPa	ISO 75-f	°C	152
Thermal Conductivity	23°C	ISO 22007-4	W m^{-1} K^{-1}	0.29
Relative Thermal Index	Electrical	UL 746B	°C	260
	Mechanical w/o impact			240
	Mechanical w/impact			180
Flow				
Melt Viscosity	400°C	ISO 11443	Pa.s	350
Miscellaneous				
Density	Crystalline	ISO 1183	g cm^{-3}	1.30
	Amorphous			1.26
Shore D hardness	23°C	ISO 868		84.5
Water Absorption (3.2mm thick Tensile bar)	24h, 23°C	ISO 62-1	%	0.07
(by immersion)	Equilibrium, 23°C			0.4

Electrical Properties				
Dielectric Strength	2mm thickness	IEC 60243-1	kV mm^{-1}	23
	50µm thickness			190
Comparative Tracking Index		IEC 60112	V	150
Loss Tangent	23°C, 1MHz	IEC 60250	n/a	0.004
Dielectric Constant	23°C, 1kHz	IEC 60250	n/a	3.1
	23°C, 50Hz			3.0
	200°C, 50Hz			4.5
Volume Resistivity	23°C	IEC 60093	Ω cm	10^{16}
	125°C			10^{15}
	275°C			10^{9}

Fire Smoke Toxicity				
Glow Wire Test	2mm thickness	IEC 60695-2-12	°C	960
Limiting Oxygen Index	0.4mm thickness	ISO 4589	% O_2	24
	3.2mm thickness			35
Toxicity Index	CO content	NES 713	n/a	0.074
	CO_2 content			0.15
	Total gases			0.22

Recommended Processing Conditions	
Drying Temperature / Time	150°C / 3h or 120°C / 5h
Temperature settings	355 / 360 / 365 / 370 / 375°C (Nozzle)
Hopper Temperature	Not greater than 100°C
Mould Temperature	170°C - 200°C (max 250°C)
Runner	Die / nozzle >3mm, manifold >3.5mm
Gate	>1mm or 0.5 x part thickness

Mould Shrinkage and Spiral Flow					
Spiral Flow	375°C nozzle, 180°C tool	1mm thick section	Victrex	mm	110
Mould Shrinkage	375°C nozzle, 180°C tool	Along flow	ISO 294-4	%	1.0
		Across flow			1.3

Important note:

Data are generated in accordance with prevailing national, international and internal standards, and should be used for material comparison. Actual property values are highly dependent on part geometry, mould configuration and processing conditions. Properties may also differ for along flow and across flow directions

Detailed data available on our website www.victrex.com or upon request

World Headquarters
Victrex plc, Hillhouse International, Thornton Cleveleys, Lancashire FY5 4QD United Kingdom
Tel: + (44) 1253 897700 Fax: + (44) 1253 897701 Email: victrexplc@victrex.com

DUPONT™ KAPTON® HN

POLYIMIDE FILM

DESCRIPTION

DuPont™ Kapton® HN general-purpose film has been used successfully in applications at temperatures as low as -269°C (-452°F) and as high as 400°C (752°F). HN film can be laminated, metallized, punched, formed or adhesive coated. Kapton® HN is the recommended choice for applications that require an all-polyimide film with an excellent balance of properties over a wide range of temperatures.

APPLICATIONS

- Mechanical parts
- Electronic parts
- Electrical Insulation
- Pressure sensitive tape
- Fiber optics cable
- Insulation blankets
- Insulation tubing
- Automotive diaphragms sensors and manifolds
- Etching
- Shims

PRODUCT SPECIFICATIONS

Kapton® HN is manufactured, slit and packaged according to the product specifications listed in H-38479, Bulletin GS-96-7.

CERTIFICATION

Kapton® HN meets ASTM D-5213 (type 1, item A) requirements.

DUPONT™ KAPTON® HN

Table 1 – Physical Properties of DuPont™ Kapton® HN at 23°C (73°F)

Property	Unit	1 mil 25µm	2 mil 50µm	3 mil 75µm	5 mil 125µm	Test Method
Ultimate Tensile Strength at 23°C, (73°F) at 200°C (392°F)	psi (MPa)	33,500 (231) 20,000 (138)	33,500 (231) 20,000 (138)	33,500 (231) 20,000 (138)	33,500 (231) 20,000 (138)	ASTM D-882-91, Method A*
Ultimate Elongation at 23°C, (73°F) at 200°C (392°F)	%	72 83	72 83	78 83	82 83	ASTM D-882-91, Method A
Tensile Modulus at 23°C, (73°F) at 200°C (392°F)	psi (GPa)	400,000 (2.76) 290,000 (2.0)	400,000 (2.76) 290,000 (2.0)	400,000 (2.76) 290,000 (2.0)	400,000 (2.76) 290,000 (2.0)	ASTM D-882-91, Method A
Density	g/cc	1.42	1.42	1.42	1.42	ASTM D-1505-90
MIT Folding Endurance	cycles	285,000	55,000	6,000	5,000	ASTM D-2176-89
Tear Strength-propagating (Elmendorf), N (lbf)		0.07 (0.02)	0.21 (0.02)	0.38 (0.02)	0.58 (0.02)	ASTM D-1922-89
Tear Strength, Initial (Graves), N (lbf)		7.2 (1.6)	16.3 (1.6)	26.3 (1.6)	46.9 (1.6)	ASTM D-1004-90
Yield Point at 3% at 23°C, (73°F) at 200°C (392°F)	MPa (psi)	69 (10,000) 41 (6,000)	69 (10,000) 41 (6,000)	69 (10,000) 41 (6,000)	69 (10,000) 41 (6,000)	ASTM D-882-91
Stress to produce 5% elong. at 23°C, (73°F) at 200°C (392°F)	MPa (psi)	90 (13,000) 62 (9,000)	90 (13,000) 62 (9,000)	90 (13,000) 62 (9,000)	90 (13,000) 62 (9,000)	ASTM D-882-92
Impact Strength at 23°C, (73°F)	N-cm-(ft lb)	78 (0.58)	78 (0.58)	78 (0.58)	78 (0.58)	DuPont Pneumatic Impact Test
Coefficient of Friction, kinetic (film-to-film)		0.48	0.48	0.48	0.48	ASTM D-1894-90
Coefficient of Friction, static (film-to-film)		0.63	0.63	0.63	0.63	ASTM D-1894-90
Refractive Index (sodium D line)		1.70	1.70	1.70	1.70	ASTM D-542-90
Poisson's Ratio		0.34	0.34	0.34	0.34	Avg. three samples, elongated at 5, 7, 10%
Low temperature flex life		pass	pass	pass	pass	IPC-TM-650, Method 2.6.18

*Specimen size 25 x 150 mm (1.6 in); jaw separation 100 mm (4 in), jaw speed, 50mm/min (2 in/min). Ultimate refers to the tensile strength and elongation measured at break.

Table 2 – Thermal Properties of DuPont™ Kapton® HN Film

Thermal Property	Typical Value	Test Condition	Test Method
Melting Point	None	None	ASTM E-794-85 (1989)
Thermal Coefficient of Linear Expansion	20 ppm/°C (11 ppm/°F)	-14 to 38°C (7 to 100°F)	ASTM D-696-91
Coefficient of Thermal Conductivity, W/m-K $\frac{\text{cal}}{\text{cm-sec-°C}}$	0.12 2.87×10^{4}	296K 23°C	ASTM F-433-77 (1987)
Specific Heat, J/g•K (cal/g-°C)	1.09 (0.261)		Differential calorimetry
Heat Sealability	not heat sealable		
Solder Float	pass		IPC-TM-650 Method 2.4.13A
Smoke Generation	D_m=<1	NBS smoke chamber	NFPA-258
Shrinkage, % 30 min at 150°C 120 min at 400°C	 0.17 1.25		IPC-TM-650 Method 2.2.4A; ASTM D-5214-91
Limiting Oxygen Index, %	37–45		ASTM D-2863-87
Glass Transition Temperature (T_g)	A second order transition occurs in Kapton® between 360°C (680°F) and 410°C (770°F) and is assumed to be the glass transition temperature. Different measurement techniques produce different results within the above temperature range.		

DUPONT™ KAPTON® HN

Table 3 – Typical Electrical Properties of DuPont™ Kapton® HN Film at 23°C (73°F), 50% RH

Property Film Gage	Typical Value		Test Condition	Test Method
Dielectric Strength	**V/m kV/mm**	**(V/mil)**		
25 µm (1 mil)	303	(7700)	60 Hz	
50 µm (2 mil)	240	(6100)	1/4 in electrodes	ASTM D-149-91
75 µm (3 mil)	201	(5100)	500 V/sec rise	
125 µm (5 mil)	154	(3900)		
Dielectric Constant				
25 µm (1 mil)	3.4		1 kHz	ASTM D-150-92
50 µm (2 mil)	3.4			
75 µm (3 mil)	3.5			
125 µm (5 mil)	3.5			
Dissipation Factor				
25 µm (1 mil)	0.0018		1 kHz	ASTM D-150-92
50 µm (2 mil)	0.0020			
75 µm (3 mil)	0.0020			
125 µm (5 mil)	0.0026			
Volume Resistivity	·cm			
25 µm (1 mil)	1.5 x 1017			ASTM D-257-91
50 µm (2 mil)	1.5 x 1017			
75 µm (3 mil)	1.4 x 1017			
125 µm (5 mil)	1.0 x 1017			

DIMENSIONAL STABILITY

The dimensional stability of DuPont™ Kapton® polyimide film depends on two factors–the normal coefficient of thermal expansion and the residual stresses placed in the film during manufacture. The latter causes Kapton® to shrink on its first exposure to elevated temperatures as indicated in the bar graph in **Figure 1.** Once the film has been exposed, the normal values of the thermal coefficient of linear expansion as shown in **Table 4** can be expected.

Figure 1. Residual Shrinkage vs. Exposure Temperature and Thickness, DuPont™ Kapton® HN

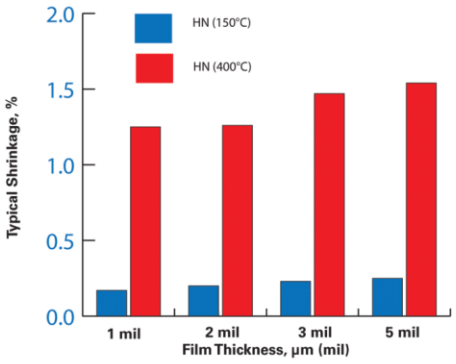

Table 4 – Thermal Coefficient of Expansion, DuPont™ Kapton® HN Film, 25 µm (1 mil), Thermally Exposed

Temperature Range, °C, (°F)	ppm/°C
30–100 (86–212)	17
100–200 (212–392)	32
200–300 (392–572)	40
300–400 (572–752)	44
30–400 (86–752)	34

DUPONT™ KAPTON® HN

FOR MORE INFORMATION ON DUPONT™ KAPTON® POLYIMIDE FILMS, PLEASE CONTACT YOUR LOCAL REPRESENTATIVE, OR VISIT OUR SALES & SUPPORT WEBPAGE FOR ADDITIONAL REGIONAL CONTACT INFORMATION.

kapton.com

K-15345-3 (8/18)

DuPont™ Vespel® SP-1

POLYIMIDE ISOSTATIC SHAPES

CLICK, SHOP ONLINE »

Typical ISO Properties

DuPont™ Vespel® SP-1 parts and shapes are specified for their excellent physical properties, including electrical and thermal insulation at high temperatures. SP-1 is an unfilled polymer.

Some data presented below are based on limited production runs and are subject to revision as new knowledge and experience become available.

Mechanical Property	Temperature	ASTM	Units	Typical Values
Tensile Strength	23 °C (73 °F) 260 °C (500 °F)	D-1708 or E8†	MPa (kpsi)	86.2 (12.5) 41.4 (6.0)
Strain at Break	23 °C (73 °F) 260 °C (500 °F)	D-1708 or E8†	%	7.5 6.0
Flexural Strength	23 °C (73 °F) 260 °C (500 °F)	D-790	MPa (kpsi)	110.3 (16.0) 62.1 (9.0)
Flexural Modulus	23 °C (73 °F) 260 °C (500 °F)	D-790	MPa (kpsi)	3102 (450) 1724 (250)
Compressive Stress at 1% strain at 10% strain at 0.1% offset	 23 °C (73 °F) 23 °C (73 °F) 23 °C (73 °F)	D-695	MPa (kpsi)	 24.8 (3.6) 133.1 (19.3) 51.0 (7.4)
Compressive Modulus	23 °C (73 °F)	D-695	MPa (kpsi)	2413 (350)
Axial Fatigue, Endurance Limit at 10^3 cycles at 10^7 cycles	 23 °C (73 °F) 260 °C (500 °F) 23 °C (73 °F) 260 °C (500 °F)	—	MPa (kpsi)	 55.8 (8.10) 26.2 (3.8) 42.1 (6.1) 16.5 (2.4)
Flexural Fatigue, Endurance Limit at 10^3 cycles at 10^7 cycles	 23 °C (73 °F) 23 °C (73 °F)	—	MPa (kpsi)	 65.5 (9.5) 44.8 (6.5)
Shear Strength	23 °C (73 °F)	D-732	MPa (kpsi)	89.6 (13.0)
Izod Notched Impact Strength	23 °C (73 °F)	D-256	J/m	42.7
Izod Unotched Impact Strength	23 °C (73 °F)	D-256	J/m	747
Poisson's Ratio	23 °C (73 °F)	—	—	0.41
Wear and Friction				
Wear Rate††	—	—	m/s x 10^{-10}	17– 85
Friction Coefficient** PV = 0.875 MPa·m/s PV = 3.5 MPa·m/s	—	—	—	0.29
In Vacuum	—	—	—	—
Static in Air	—	—	—	0.35

DUPONT
The miracles of science™

DuPont™ Vespel® SP-1 Typical ISO Properties *(continued)*

Thermal Property	Temperature	ASTM	Units	Typical Values
Coefficient of Linear Expansion	23 °C (73 °F) to 260 °C (500 °F) –62 to +23 (–80 to 73° F)	D-696	µm/m/°C (in/in/°F)	54 (30) 45 (25)
Thermal Conductivity	40 °C (104 °F)	—	W/m·°C	0.35
Specific Heat	—	—	J/kg/°C	1130
Deformation Under 14 MPa Load	50 °C (122 °F)	D-621	%	0.14
Deflection Temperature at 2 MPa	—	D-648	°C	~360
Electrical Property				
Dielectric Constant at 10^2 Hz at 10^4 Hz at 10^6 Hz	23 °C (73 °F)	D150	—	 3.62 3.64 3.55
Dissipation Factor at 10^2 Hz at 10^4 Hz at 10^6 Hz	23 °C (73 °F)	D150	—	 0.0018 0.0036 0.0034
Dielectric Strength, Short Time 2 mm Thick	23 °C (73 °F)	D149	MV/m	22 (3.20)
Volume Resistivity	23 °C (73 °F)	D257	Ω·m	10^{14}–10^{15}
Surface Resistivity	23 °C (73 °F)	D257	Ω	10^{15}–10^{16}
Other Properties				
Water Absorption 24 h 48 h Equilibrium, 50% RH	 23 °C (73 °F) 50 °C (122 °F)	D570	%	 0.24 0.72 1.0–1.3
Specific Gravity	—	D792	—	1.43
Oxygen Index	—	D2863	%	53

† Machined isoststic tensile specimens made per D1708
†† Unlubricated in air (PV 0.875 MPa·m/s).
** Steady state, unlubricated in air.

Visit us at kalrez.dupont.com or vespel.dupont.com

Contact DuPont at the following regional locations:

North America
800-222-8377

Latin America
+0800 17 17 15

Greater China
+86-400-8851-888

ASEAN
+65-6586-3688

(09/10) Reference No. VPE-A10861-00-B0614

DUPONT
The miracles of science™

Appendix B:
Calculated Diffusion Coefficients and Initial Moisture Contents of the Samples

Table 5. Diffusion coefficients of the samples calculated through the fitting procedure.

Kapton HN		Vespel SP-1		PEEK 450 G	
Thickness (mm)	D ($cm^2\ s^{-1}$)	Thickness (mm)	D ($cm^2\ s^{-1}$)	Thickness (mm)	D ($cm^2\ s^{-1}$)
0.0125	$1.10 \cdot 10^{-09}$	0.25	$1.80 \cdot 10^{-09}$	0.16	$3.50 \cdot 10^{-09}$
0.025	$1.50 \cdot 10^{-09}$	0.25*	$1.95 \cdot 10^{-09}$	0.18	$2.90 \cdot 10^{-09}$
0.05	$2.00 \cdot 10^{-09}$	0.45	$1.80 \cdot 10^{-09}$	0.47	$4.60 \cdot 10^{-09}$
0.075	$2.00 \cdot 10^{-09}$	0.92	$1.75 \cdot 10^{-09}$	0.5	$4.60 \cdot 10^{-09}$
0.125	$2.00 \cdot 10^{-09}$	1.30	$1.80 \cdot 10^{-09}$	0.72	$4.60 \cdot 10^{-09}$
		1.80	$1.80 \cdot 10^{-09}$	0.94	$4.60 \cdot 10^{-09}$
				1.28	$4.50 \cdot 10^{-09}$
Average	$1.72 \cdot 10^{-09}$	Average	$1.82 \cdot 10^{-09}$	Average	$4.19 \cdot 10^{-09}$
St. deviation	$3.66 \cdot 10^{-10}$	St. deviation	$6.24 \cdot 10^{-11}$	St. deviation	$6.45 \cdot 10^{-10}$

Table 6. Initial moisture content of the samples calculated through the fitting procedure.

Kapton HN		Vespel SP-1		PEEK 450 G	
Thickness (mm)	C_0 (wt.%)	Thickness (mm)	C_0 (wt.%)	Thickness (mm)	C_0 (wt.%)
0.0125	0.90	0.25	0.68	0.16	0.25
0.025	1.00	0.25*	0.65	0.18	0.33
0.05	1.05	0.45	0.75	0.47	0.22
0.075	1.00	0.92	1.80	0.5	0.28
0.125	0.90	1.30	0.95	0.72	0.30
		1.80	0.80	0.94	0.28
				1.28	0.22
Average	0.97	Average	0.94	Average	0.27
St. deviation	0.06	St. deviation	0.40	St. deviation	0.04

*The same 0.25 mm thick Vespel SP-1 sample was tested twice